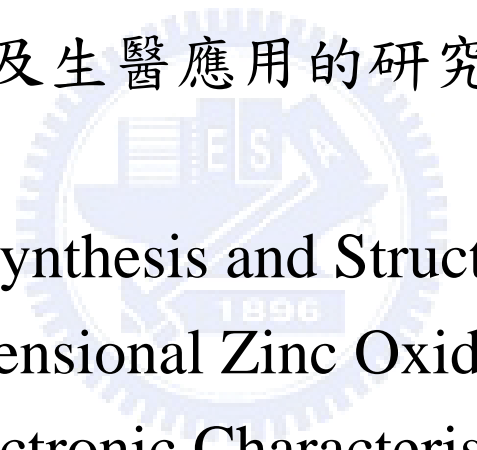


國立交通大學
材料科學與工程學系
博士論文

一維氧化鋅的合成與結構對於光電特性
及生醫應用的研究



Study on Synthesis and Structure of One
Dimensional Zinc Oxide for
Optoelectronic Characteristics and
Bio-Medical Applications

研究生：蕭繼聖
指導教授：陳三元 博士

九十七年 十月

Contents

Contents	I
摘要	IV
Abstract	V
誌謝	VII
Chapter 1	1
Chapter 2 Literature Review	4
2.1 ZnO nanorods	4
2.1.1 Introduction	4
2.1.2 Crystal and surface structure of ZnO	5
2.1.3 Growth ZnO nanorods	5
2.1.4 ZnO defect chemistry	6
2.1.5 Applications of the ZnO nanorods	8
2.2 ZnO nanotubes	9
2.3 Nano-Alumina material	11
2.3.1 Structure and phase of alumina material	11
2.3.2 Synthesis and optical of nano-alumina material	12
2.4 ZnO Core/shell materials	13
2.5 ZnO nanostructure in the bio-medical application	14
Chapter 3 Experimental materials and methods	26
3.1 Flow chart of experimental procedure	26
3.2 ZnO thin films formation	27
3.3 Wet-chemical growth of ZnO nanorods and nanotubes	27
3.4 Wet-chemical synthesis of alumina nanoparticles and nanofilms	27
3.5 Synthesis and thermal treatment of alumina/ZnO core/shell structure	28

3.6 Characterization of ZnO and alumina materials	29
Chapter 4 Tunable growth of ZnO nanorods synthesized in aqueous solutions at low	
temperatures.....	30
4.1 Introduction	30
4.2 ZnO nanorods with different growth parameters	31
4.3 Patterned growth of the ZnO nanorods.....	32
4.4 The relation between ZnO film and ZnO nanorods.....	33
4.5 Summary	34
Chapter 5 Growth behavior and microstructure evolution of ZnO nanorods grown on Si	
in aqueous solution.....	44
5.1 Introduction	44
5.2 Phase and morphology of ZnO nanorods grown on different substrates	45
5.3 Microstructural analysis of ZnO nanorods.....	46
5.4 Growth behavior of ZnO nanorods	48
5.5 Summary	50
Chapter 6 Synthesis and Luminescent Properties of Strong Blue Light-Emitting	
Al₂O₃/ZnO Nanocables	59
6.1 Introduction	59
6.2 The structure of the Al ₂ O ₃ /ZnO nanocables	60
6.3 Annealing effect on the Al ₂ O ₃ /ZnO nanocables.....	62
6.4 The investigation of photoluminescence centers in the Al ₂ O ₃ /ZnO nanocables .	63
6.5 Summary	67
Chapter 7 Synthesis and Optical Properties of White-light Emitting Alumina/ZnO	
Nanotubes	76
7.1 Introduction	76
7.2 Synthesis and physical properties of ZnO nanotubes	77

7.3 The structure of the ZnO nanotubes after thermal annealing	79
7.4 The structure of the alumina/ZnO nanotubes	81
7.5 The optical properties of the alumina/ZnO nanotubes	82
7.6 Summary	84
Chapter 8 Smart ZnO nanotube for Controlled Drug Release	96
Chapter 9 Conclusions	109
References.....	111
Curriculum Vitae	116
Publication list	117



摘要

氧化鋅被視為明星的奈米材料之一，由於其寬廣的能隙(3.37 eV)，並且具有卓越的化學和熱穩定性，使得在眾多產業上有著很好地應用。隨著一維奈米材料的發展，如何合成一維氧化鋅奈米結構，就變成了一項重要的研究。在過去幾年，發展出利用低溫溶液法成長氧化鋅奈米結構，並且，可以控制成長好幾種的形態。然而，氧化鋅本身的複雜缺陷結構，卻大大地影響了其應用。因此，如何改善和操控缺陷，就變成了一項非常值得深入的研究主題，另外，一個聰明的氧化鋅元件，在生物醫學方面的研究，也是令人期待。所以，本論文研究會深入地探討，一維氧化鋅的合成即其光學特性、氧化鋁-氧化鋅殼核結構的光學性質，最後會利用染料模擬藥物釋放，來研究藥物載體(氧化鋅)在電場下的釋放行為。

在第一章，我們會一般地介紹氧化鋅材料。在第二章，將會討論氧化鋅的基本特性、缺陷、製程、應用和生醫藥物。第三章將會介紹實驗製程，包含氧化鋅和氧化鋁-氧化鋅殼核結構的製程，並且，量測方法和設備皆會在這章做介紹。

第四章主要會說明氧化鋅奈米柱如何經由水溶液法成長在，鍍有氧化鋅薄膜的矽基版上，而其成長的形態跟薄膜上的晶粒大小有絕對的關係。第五章將會討論在兩種基版上氧化鋅奈米柱的成長行為。

第六章將會展示陣列式氧化鋁-氧化鋅殼核奈米結構，經由溶凝膠法在室溫所製成，並且經由光譜分析得知，此結構在 400°C、600°C 的氧氣、氮氣熱處理後，能發出在 450 nm 強烈藍光。第七章將會先介紹如何經由化學溶液法，合成氧化鋅奈米管，更進一步展示氧化鋁-氧化鋅奈米管的成長。在經過不同溫度和氣氛熱處理下，此奈米管將會發出各種不同顏色的光，經由高斯分析可知，這些光有藍、藍-綠，綠和黃光，這些光和奈米管的缺陷有強烈的相關性。

最後，在第八章將會展示如何用高頻電場控制 FITC-ZnO 奈米管的釋放行為。另外，也可以證明此氧化鋅結構，具有低能量損耗、良好的生物相容性、生物標示和低成本的特性。

Abstract

ZnO has been recognized as one of the promising nanomaterials in a broad range of high-technology applications because ZnO has a large direct band gap (3.37 eV), excellent chemical and thermal stability, and the electrical properties of a large exciton binding energy (60 meV). Furthermore, with one-dimensional materials developing, the synthesis of one-dimensional ZnO nanostructure becomes an important research. In the past several years, a low-temperature solution-based method to prepare complex ZnO nanostructures has been developed. In addition, ZnO morphology can be controlled via simple solution route. However, a fatal problem for ZnO material is complex defects. Therefore, it is worth to be studied on how to improve and manipulate defects. In addition, ZnO nanostructures are believed to be nontoxic and possibly biocompatible. A smart ZnO device for bio-medical is expected to develop. Therefore, this thesis outlines the process and optical of one-dimensional ZnO nanostructures and the study of photoluminescent properties and light-emitting characteristics of ZnO/alumina core/shell nanostructure. Finally, Drug release behavior from dye-ZnO nanostructure by applying high frequency electric field is also given in this thesis.

In chapter 1, we will present an introductory overview to ZnO materials. Chapter 2 will discuss fundamental, defects, synthesis process, application and bio-medical. Chapter 3 will introduce the experimental process, including ZnO and alumina-coated ZnO nanostructure. The measurement setup for optoelectronic characteristics is also shown in this chapter.

Chapter 4 will demonstrate that highly arrayed ZnO nanorods were fabricated on the Si substrate buffered with patterned ZnO film (ZnO_f/Si) via wet-chemical process. It was found that the growth morphology of ZnO nanorods is strongly dominated by the grain size of the ZnO film on the Si substrate. Chapter 5 will discuss growth behavior of the ZnO nanorods. Two substrates, Si and ZnO film-coated Si (ZnO_f/Si), were used to investigate growth

behavior and microstructure evolution of single-crystal ZnO nanorods (ZNs) in aqueous solutions at low temperatures.

Chapter 6 will show that hetrostructured AlO_x-ZnO core-shell nanocables arrays have been successfully synthesized by soaking the ZnO nanorods in the sol-gel solution of Al(NO₃)₃ and NH₄OH at room temperature. Photoluminescence measurement indicates that a strong blue emission peak at ~450 nm appears at 400°C and 600°C in O₂ and N₂ atmospheres, respectively. Chapter 7 will induce to synthesize the ZnO nanotubes by chemical solution method. Moreover, a simple chemical solution process for alumina/ZnO nanotubes will be studied. After thermal treatment at different temperatures under various atmospheres, photoluminescence (PL) measurements showed that the alumina nanoparticles coated on ZnO nanotubes (ANZTs) emitted a variety of colors, including blue, green and white light. Gaussian curve fitting of the PL spectra revealed that the competition between the blue, blue-green, green and yellow band emissions and their relative emission intensities were strongly associated with various defects.

Finally, Chapter 8 will demonstrate the controlled release behavior of the FITC-ZnO nanotubes by high frequency electric-field. This ZnO-based nanostructure possesses low power consumption, biocompatible, bio-imaging and low-cost characteristic.

誌謝

在這漫長的求學路途上，我首先想感謝我的父母，沒有他們的幫助，我不可能可以完成我的學業，他們的默默支持，是我可以全力專心研究的最大助力。接下來，我想感謝我的指導教授-陳三元，把我從一位不會做學術研究的學生，在他的不放棄的指導下，學生終於對於如何做研究，有了些許的心得。另外，我也很感謝另一位教授-劉典謨，對我研究路途上的幫助，他教會我如何深入做研究。再來，我想感謝可愛的琬琳學妹，在她的幫助下，我完成了很多複雜的實驗，沒有她，我想我不可能可以完成這論文的深度。接下來，我想感謝晉慶學長，有他的幫助，幫我解答了很多深入的問題，以及他對我的細心的照顧。另外，我想感謝尚秀和維琳，在他們兩位的幫助下，我才能完成我論文的最後一部份，以及帶我認識不熟悉的領域。除此之外，我要感謝實驗室的每一位同學和學弟妹，因為，有他們才能使我有愉快的博士生活，抱持快樂的心態。

Chapter 1

Introduction

Low-dimensional nanostructural materials have been extensively studied for their application in photonic and electronic devices, for example, GaN, ZnO and ZnS. They have attracted considerable interest in application to ultraviolet (UV) laser devices due to their direct wide band gaps. Among them, ZnO ($\Delta E_g = 3.37$) is thought to be the most suitable material for UV laser devices due to its large excitation binding energy of 60 meV compared to the thermal energy (26 meV) of room temperature.[1-4] ZnO is belonging to wurtzite structure which are the noncentral symmetry and polar surfaces. The structure of ZnO can be assigned to a number of alternating planes composed of tetrahedrally coordinated O^{2-} and Zn^{+2} ions, stacked along the c-axis. Therefore, the ZnO is a good candidate for applications in optoelectronics, lasing, and piezoelectricity. Recently, arrays of ZnO nanorods are expected to speed charge migration for solar cell application, due to their lower trap density and more direct path to the current collecting electrode. In order to increase surface volume ratio for raising sensitivity, ZnO nanotubes are good candidate material.[5] Furthermore, ZnO is also a bio-safe and biocompatible, which can be used for biomedical application without coating.[6]

Nowadays, various synthetic approaches have been developed to fabricate ZnO nanostructures, which can be classified into two categories, vapor-phase and solution-phase synthesis. Vapor-phase processes such as vapor-liquid-solid growth (VLS),[7] chemical vapor deposition (CVD),[8] thermal decomposition,[9] and thermal evaporation[10] are favored for their simplicity and high-quality products. Solution-phase routes are appealing due to their low growth temperature, low cost, high efficiency, and potential for scale up. On the other

side, many morphology of ZnO nanostructure have been discovered by various synthesized processes, such as nanobelts, nanosprings, nanorings, nanorods, nanotubes.[12-15]

Although one dimension ZnO nanorods and nanotubes show very attractive properties, such as electric, optical and bio-safe properties, it is an important issue how to tune the ZnO nanorods growth by wet-chemical method. Therefore, in the PhD thesis, several main topics will be investigated. (i) In Chapter 4, we will first study the synthesis and growth control of highly arrayed ZnO nanorods on the Si substrate buffered with patterned ZnO film (ZnO_f/Si) via wet-chemical process. The growth behavior and morphology of single-crystal ZnO nanorods (ZNs) were investigated in terms of the annealing temperatures of the sputtered ZnO film.(ii) In Chapter 5, the growth behavior of ZnO nanorods will be focused. Two substrates, Si and ZnO film-coated Si (ZnO_f/Si), were used to investigate growth behavior and microstructure evolution of single-crystal ZnO nanorods (ZNs) in aqueous solutions at low temperatures. (iii) ZnO nanorods have been used for LED application for many years and ZnO nanorods can be used are good template due to good conduct electricity. Therefore, in Chapter 6, the photoluminescence and HRTEM interface microstructure of the $\text{AlO}_x\text{-ZnO}$ core-shell nanocables will be investigated and discussed. (iv) Recently, ZnO nanotubes have attracted more attention due to excellent properties, such as high surface/volume ratio. Therefore, in Chapter 7, we will first investigate the synthesis of the ZnO nanotubes by chemical solution method. Next, in order to develop white light LED, a simple chemical solution process developed for alumina/ZnO nanotubes will be studied. The photoluminescence (PL) measurements of the alumina/ZnO nanotubes after thermal treatment at different temperatures under various atmospheres will be further analyzed. (v) Since ZnO materials have been believed to be nontoxic, biosafe, and possibly biocompatible, it could be developed for biomedical applications in our daily life, such as drug carriers and cosmetics. Therefore, in Chapter 8, we will introduce the ZnO nanotubes in the application of drug carriers. It was demonstrated that drug released from the ZnO nanotubes can be controlled by

the ZnO-based electric device. Furthermore, a test with the cell will be performed on the bio-imaged ZnO nanostructures. Finally, conclusions and future researches will be summarized.



Chapter 2

Literature Review

2.1 ZnO nanorods

2.1.1 Introduction

Nanostructured ZnO materials have attracted much attention due to their exceptional performance in electronics, optics and photonics. From the 1960s, synthesis of ZnO thin films has been an active field because of their applications as sensors, transducers and catalysts. In the last few decades, especially since the nanotechnology initiative led by the US, study of one-dimensional (1D) materials has become a leading edge in nanoscience and nanotechnology. With decreasing volume size, novel electrical, mechanical, chemical and optical properties are introduced, which are believed to be the result of surface and quantum confinement effects. Nanowire-like structures are the ideal system for studying the transport process in one-dimensionally (1D) confined objects, which are of benefit not only for understanding the fundamental phenomena in low dimensional systems, but also for developing new generation nano-devices. ZnO is a key technological material. The lack of a centre of symmetry in wurtzite, combined with large electromechanical coupling, results in strong piezoelectric and pyroelectric properties and the consequent use of ZnO in mechanical actuators and piezoelectric sensors. In addition, ZnO is a wide band-gap (3.37 eV) compound semiconductor that is suitable for short wavelength optoelectronic applications. The high exciton binding energy (60meV) in ZnO crystal can ensure efficient excitonic emission at room temperature and room temperature ultraviolet (UV) luminescence has been reported in disordered nanoparticles and thin films. ZnO is transparent to visible light and can be made

highly conductive by doping. ZnO is a versatile functional material that has a diverse group of growth morphologies, such as nanocombs, nanorings, nanosprings, nanobelts, nanowires and nanocages. The basic materials parameters of ZnO are shown in Figure 2.1.

2.1.2 Crystal and surface structure of ZnO

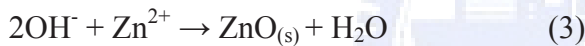
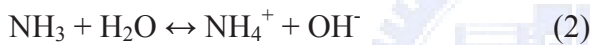
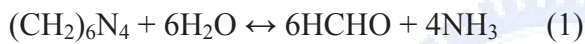
Wurtzite zinc oxide has a hexagonal structure (space group $C6mc$) with lattice parameters $a = 0.3296$ and $c = 0.52065$ nm. The structure of ZnO can be simply described as a number of alternating planes composed of tetrahedrally coordinated O^{2-} and Zn^{2+} ions, stacked alternately along the c -axis (Figure 2.2[16]). The tetrahedral coordination in ZnO results in non central symmetric structure and consequently piezoelectricity and pyroelectricity. Another important characteristic of ZnO is polar surfaces. The most common polar surface is the basal plane. The oppositely charged ions produce positively charged Zn-(0001) and negatively charged O-(000 $\bar{1}$) surfaces, resulting in a normal dipole moment and spontaneous polarization along the c -axis. To maintain a stable structure, the polar surfaces generally have facets or exhibit massive surface reconstructions, but ZnO \pm (0001) are exceptions: they are atomically flat, stable and without reconstruction.[17,18] The other two most commonly observed facets for ZnO are $\{2\bar{1}\bar{1}0\}$ and $\{01\bar{1}0\}$, which are non-polar surfaces and have lower energy than the $\{0001\}$ facets.

2.1.3 Growth ZnO nanorods

The different surface structures of ZnO could induce anisotropic growth. Under thermodynamic equilibrium conditions, the facet with higher surface energy is usually small in area, while the lower energy facets are larger. Specifically, in the ZnO growth, the highest growth rate is along the c -axis and the large facets are usually $\{01\bar{1}0\}$ and $\{2\bar{1}\bar{1}0\}$. Therefore, the ZnO nanorods can be synthesized by many process, including chemical bath deposition(CBD)[19,20], aqueous chemical solution[21], and vapour-liquid-solid (VLS)[22].

The growth mechanism from VLS method was proposed in the 1960s-1970s for large whisker growth. This method is promotion of anisotropic crystal growth using metal nanoparticles as catalysts. Yang et al. [22] reported the use of the vapor-phase transport process to grow ZnO nanowires via the VLS mechanism. The Zn vapor was generated using carbothermal or hydrogen reduction of ZnO. Size control of the nanowire diameters was achieved by varying the thickness of the thin film Au catalyst.

Another important growth method is aqueous chemical method. Vayssieres *et al.* [21] used this method to grow nanorods on conducting glass and Si substrates. For this type of growth, a ZnO seed layer is needed to initialize the uniform growth of oriented nanorods. Often, a solution of Zn(NO₃)₂ and hexamethyltetramine (HMT) is used:



Hydroxide ions are formed by the decomposition of HMT and they react with the Zn²⁺ to form ZnO.

Idealized growth habit of a ZnO crystal was first to describe by Laudise [23,24] by the hydrothermal method. It has been observed that the maximal crystal growth velocity is fixed in the <0001> direction and the following relationship between the velocities of crystal growth to different directions is found to be: $V_{\langle 0001 \rangle} > V_{\langle 01\bar{1}0 \rangle} > V_{\langle 000\bar{1} \rangle}$. Because the fastest growth plane (0002) will be disappeared, the shape of ZnO nanostructure would become wires or rods.

2.1.4 ZnO defect chemistry

There are a number of intrinsic defects with different ionization energies in ZnO structure. The Kroger Vink notation uses: i = interstitial site, Zn = zinc, O = oxygen, and V = vacancy. The terms indicate the atomic sites, and superscripted terms indicate charges, where a dot

indicates positive charge, a prime indicates negative charge, and a cross indicates zero charge, with the charges in proportion to the number of symbols. Figure 2.3 shows that there are a number of defect states within the bandgap of ZnO. The donor defects are: Zn_i^{**} , Zn_i^{\bullet} , Zn_i^{\times} , V_o^{**} , V_o^{\bullet} , V_o and the acceptor defects are: V_{Zn}'' , V_{Zn}' . The defect ionization energies vary from ~ 0.05 - 2.8 eV. Zn interstitials and oxygen vacancies are known to be the predominant ionic defect types.[25]

Figure 2.4 [26] shows the corrected formation energies for the relevant native point defects in ZnO as a function of Fermi-level position. The kinks in the curves for a given defect indicate transitions between different charge states. The differences are related to the correction of absolute formation energies, where we now take into account the occupancy of the defect-induced states in the case of defects with partially occupied states in the band gap. Oxygen vacancies have the lowest formation energy (see Fig. 2.4). Oxygen vacancies have frequently been invoked as the source of unintentional *n*-type conductivity in ZnO. Prof. Vanheusden found that the green emission intensity is strongly influenced by free-carrier depletion at the particle surface, particularly for small particles and/or low doping. Their data suggested that the singly ionized oxygen vacancy is responsible for the green emission in ZnO; this emission results from the recombination of a photogenerated hole with the singly ionized charge state of this defect. [26]

Because of the different ionization energies, the relative concentrations of the various defects depend strongly on temperature. However, the partial pressure of oxygen and zinc, pO_2 and pZn , respectively, are also very important. Hence, under very reducing conditions and at high temperatures, oxygen vacancies may predominate, depending on the relative pO_2/pZn ratio. During annealing, the variety of these defects with the oxygen pressure (P_{O_2}) could be expressed as follows:

$$\frac{1}{2}O_2 + V_O^X = O_O^X \quad [V_O^X] \propto P_{O_2}^{-1/2}, \quad (4)$$

$$\frac{1}{2}O_2 = O_O^X + V_{Zn}^X \quad [V_{Zn}^X] \propto P_{O_2}^{1/2}, \quad (5)$$

$$Zn_i + \frac{1}{2}O_2 = Zn_{Zn} + O_O \quad [Zn_i] \propto P_{O_2}^{-1/2}, \quad (6)$$

$$\frac{1}{2}O_2 = O_i \quad [O_i] \propto P_{O_2}^{1/2}, \quad (7)$$

$$\frac{1}{2}O_{2(g)} + V_{Zn} = O_{Zn} \quad [O_{Zn}] \propto P_{O_2}^{1/2}[V_{Zn}]. \quad (8)$$

Equations (4) and (6) indicate that concentrations of the oxygen vacancy and the interstitial zinc decreased with the increase of oxygen pressure P_{O_2} : While Eqs. (5), (7) and (8) indicated that concentrations of the zinc vacancy, the interstitial zinc and antisite oxygen increased with the increase of the oxygen pressure P_{O_2} . [27]

2.1.5 Applications of the ZnO nanorods

So far, there are many applications of the ZnO nanorods, such as sensor, light-emitting diodes, lasing, cantilevers and solar cells. Especially, solar cells and lasing are the two famous applications. Prof. Yang reported nanowire dye-sensitized solar cells in 2005. They introduced a version of the dye-sensitized cell in which the traditional nanoparticle film was replaced by a dense array of oriented, crystalline ZnO nanowires. The nanowire anode was synthesized by mild aqueous chemistry and features a surface area up to one-fifth as large as a nanoparticle cell. The direct electrical pathways provided by the nanowires ensured the rapid collection of carriers generated throughout the device, and a full Sun efficiency of 1.5% was demonstrated. The device structure is presented in Figure 2.5. [28]

Laser application of the ZnO nanorods is also quite attracted much attention up to now. Prof. Choy show the room-temperature ZnO ultraviolet laser in 2003. They presented that a high-quality ZnO nanorods was grown on a Si wafer by a wet-chemical process at 95°C, where the Si wafer was dip-coated with 4 nm sized ZnO nanoparticles s buffer and seed layer prior

th the crystal growth. The product ZnO nanrods showed threshold power density was $\sim 70 \text{ kW cm}^{-2}$. The result can be seen in the Figure. 2.6. [29] Moreover, Prof. Wang developed a direct-current nanogenerator driven by ultrasonic waves in 2007. The nanogenerator was fabricated with vertically aligned zinc oxide nanowire arrays that were placed beneath a zigzag metal electrode with a small gap. The wave drives the electrode up and down to bend and/or vibrate the nanowires. A piezoelectric semiconducting coupling process converts mechanical energy into electricity. The zigzag electrode acts as an array of parallel integrated metal tips that simultaneously and continuously create, collect, and output electricity from all of the nanowires. The approach presents an adaptable, mobile, and cost-effective technology for harvesting energy from the environment, and it offers a potential solution for powering nanodevices and nanosystems. The nanogenerator structure was shown in the Figure 2.7. [30]

2.2 ZnO nanotubes

It is well-known that the hollow structure provides 1D ZnO with more prominent advantages than other 1D ZnO materials. For example, the formation of tubes facilitates enhancing the confinement effect in 1D structures and tuning the electronic properties of materials in a wider range. Moreover, a larger surface area-volume ratio in tubular structure provides an effective way to optimize the performances of various devices including dye-sensitized photovoltaic cells, catalysts, gas sensors, and hydrogen storage. But, few publications on the preparation of ZnO nanotubes (NTs) have been reported because the tubular form is generally limited in layered materials such as carbon nanotube so that it seems hard to obtain the tubular structure for the nonlayered ZnO material. This situation was improved from chemical solution process produced. L. Vayssieres et al. reported a famous paper, three-dimensional array of highly oriented crystalline ZnO microtubes. They presented a simple chemical solution method. A equimolar (0.1 M) aqueous solution of zinc nitrate, $\text{Zn}(\text{NO}_3)_2 \cdot 4\text{H}_2\text{O}$, and methenamine was prepared in a bottle with an autoclavable screw cap. Silicon wafers or

ITO-coated polyester substrate washed and cleaned with MilliQ water. The bottle is then heated at a constant temperature of 90°C for 2 days in a regular laboratory oven. Subsequently, the homogeneous thin films are thoroughly washed with water to remove any contamination from residual salts or amino complex. This concept was schemed in the figure 2.8. [31] However, the growth mechanism of the ZnO NTs was not clear. After five years ago, Sun and co-workers supplied growth theory. They proposed that the different surface terminations influence (through electrostatic interactions) the cation (Zn^{2+}) to anion (OH^-) concentration ratio in the double layer at the growing polar surface. Zn-atom termination causes a reduction in the local Zn^{2+}/OH^- ratios (i.e. the extent of solution supersaturation) relative to those in the bulk solution, thereby encouraging tapered NR growth and, as the zinc concentration falls further, the emergence of volcano-like structures on the polar surface which seed the subsequent growth of ZnO NTs, as shown in Figure 9. [32]

However, Han et al. thought this chemical solution process remained complex and difficult/irreproducible. They reported the low-temperature synthesis of hexagonal ZnO nanotube arrays, which can be formed on zinc foils. This process could further reduce the growth temperature to 65°C.

Optical properties of the ZnO NTs are expected to study. Zhang reported strong green emission of ZnO NTs. It is well-known that ZnO has green light emission, which has been attributed to the singly ionized oxygen vacancy in ZnO and is located at ~2.2 and ~2.5 eV, as shown in Figure 2.10. [33] They pointed out that NTs have enhanced green emission due to a much improved surface area, which is predominant over the near-band edge emission. In other words, a higher surface area to volume ratio should favor a higher level of surface and subsurface oxygen vacancies.

ZnO nanowires solar cell did not demonstrate good enough efficiency, limited primarily by the surface area of the nanowire array. ZnO NTs can just overcome this problem. Hupp et al. introduced high surface area ZnO NT photoanodes templated by anodic aluminum oxide for

use in dye-sensitized solar cells. While the new nanotube cells compare favorably with other ZnO-based DSSCs, increased surface area will clearly be needed because of energy conversion efficiencies approaching that of the best ZnO cells (4%). [34]

2.3 Nano-Alumina material

2.3.1 Structure and phase of alumina material

Alumina is a low cost material used in many domains like catalysis, ceramics and mechanical ceramics, refractory, electrotechnology, electronics, bio-medical, . . . The wide variety of these applications comes from the fact that alumina occurs in two forms, corundum or α -alumina with a hexagonal close-packing of oxygen ions and transition aluminas with a cubic close packing of oxygen. Transition aluminas include a series of metastable forms that exist on an extended temperature range, but all of them lead to α -alumina by calcining at high temperatures. Corundum has excellent mechanical, electrical, thermal, and optical properties. Transition aluminas are widely used as adsorbents, catalysts, catalyst supports, and membranes because of their high surface area, mesoporosity, and surface acidity.

Transition aluminas are prepared by calcining aluminum hydroxides. As different hydroxides were used, it usually leads to different forms having different thermal stability, surface acidity and textural properties. Among aluminum hydroxides, boehmite, aluminum oxyhydroxide (AlOOH) is an important precursor because the heat treatment of boehmite produces a series of transition aluminas from γ - Al_2O_3 and η - Al_2O_3 to δ - Al_2O_3 , and θ - Al_2O_3 , which exhibit high surface areas (200–500 m^2/g) and thermal stability up to 1000°C. [35] The structures of the transition aluminas all are based on a face-centered cubic (fcc) array of oxygen anions. The structural differences between these forms only involve the arrangement of aluminum cations in the interstices of the fcc array of oxygen anions. γ - Al_2O_3 and η - Al_2O_3 have defect spinel structures. δ - Al_2O_3 has a tetragonal superstructure of the spinel lattice with

one unit-cell parameter tripled and θ - Al_2O_3 has a monoclinic structure. η - Al_2O_3 is produced by dehydration of bayerite $\text{Al}(\text{OH})_3$, whereas γ - Al_2O_3 is formed by dehydration of boehmite. Upon heating, γ - Al_2O_3 and η - Al_2O_3 are gradually converted in θ - Al_2O_3 .

Boehmite was thought to exist under two distinct forms, well-crystallized boehmite and pseudoboehmite (also called gelatinous boehmite), with significantly different morphologies, porosity, and surface areas. [36] Pseudo-boehmite is a low crystalline aluminum oxide hydroxide. The crystal structure is consisted of a distorted AlO_6 octahedron, which is joined by sharing edges to form zigzagged layers parallel to the (010) plane. These layers are linked together by hydrogen bonds between hydroxyls in neighboring layers. Although pseudo-boehmite contains water molecules between layers, the intercalation of guest molecules is very difficult because of strong hydrogen bonding between the layers. γ -alumina is reported to occur at temperatures between 350 and 1000 °C. It is typically formed from an amorphous or boehmite precursor and has remained present at temperatures as high as 1200 °C when derived from amorphous aluminas. The bulk structure of γ alumina is closely related to that of magnesium spinel ($\text{MgO}, \text{Al}_2\text{O}_3$). [37]

2.3.2 Synthesis and optical of nano-alumina material

Alumina powders have been synthesized by Bayer process since 1888. Up to now, there are many methods to fabricate alumina powders, such as solid state deposition, precipitation, sol-gel and chemical vapor deposition. The main fabricated process in industry is Bayer process. On the other hand, sol-gel methods are a cheap and conventional process. Yoldas et al. [38] reported that transparent monolithic alumina could be obtained by the sol-gel method using an alumina sol derived from the alkoxide. Furthermore, Suga and co-workers [39] prepared transparent alumina gels from two sources, $\text{AlCl}_3 \cdot 6\text{H}_2\text{O}$ and aluminium iso-propoxide. The boehmite phase is synthesized first and usually the phase is amorphous.

Then, the thermal process can be used to promote the boehmite to transform α -alumina phase through γ -alumina.

Blue photoluminescent emission was observed in pure nanometer-sized γ -alumina powders prepared by the sol-gel process. The photoluminescent emission spectra were made up of a broad band and the emission band of 422 nm had obvious intensity. Du et al. used the alumina membranes with nano pore arrays to point out that the blue emission band is related to the singly ionized oxygen vacancies (F^+ centers). However, the formation mechanism of F^+ centers is not clear. Ishizaka and co-workers presented that the F^+ centers may be related to pentahedrally (Al^V) coordinated aluminum by NMR result. Boehmite phase is belong to octahedrally (Al^{VI}) coordinated alumina. However, the γ -alumina has tetrahedrally and octahedrally coordinated alumina. They supposed that the pentahedrally coordinated aluminum would be produced during the phase transformation. [40,41]

2.4 ZnO Core/shell materials

The nanostructures of optical materials are particularly important as the properties of these materials are greatly influenced by various surface states arising out of the higher surface-to-volume ratio. This can be further tuned by deliberately modifying the surface of nanostructured materials by other materials such as core-shell nanostructures. ZnO core/shell structure was wild application in the fields of luminescence, electronics, and sensors. Chaudhuri et al. have successfully fabricated vertically aligned ZnO-ZnS core-shell and ZnS nanorods arrays in a thin film form by sulfidation of aligned ZnO nanorod arrays. [42] The PL study at room temperature indicated that the high band gap ZnS shell confines the photogenerated carriers inside the ZnO core, and so enhanced UV emission was observed for the ZnO-ZnS core-shell nanorods, when the shell thickness is a few nanometers. Yang et al. [43] described the construction and performance of dye-sensitized solar cells (DSCs) based on arrays of ZnO nanowires coated with thin shells of amorphous Al_2O_3 by ALD. The TEM

images of alumina-coated ZnO nanorods were shown in Figure 2.11. They find that alumina shells of all thicknesses act as insulating barriers that improve cell open-circuit voltage (V_{OC}) only at the expense of a larger decrease in short-circuit current density (J_{SC}).

On the other hand, using ZnO nanowires to be a template is a well-known ideal. ZnO nanowires as a template have many advantages, such as growth process, removal and stable. Yang reported ZnO nanowires arrays were placed inside a reaction tube for single-crystal gallium nitride (GaN) nanotubes chemical vapor deposition.[44] After GaN deposition, the samples were treated at 600°C with 10% H₂ in argon to remove the ZnO nanowire templates. The GaN nanotubes could be obtained, as shown in the Figure 2.12. The same process was also used to make alumina nanotubes. Hwang et al. reported Al₂O₃ nanotubes fabricated by wet etching of ZnO/Al₂O₃ core/shell nanofibers. [45] The Al₂O₃ film was deposited on the ZnO nanowires by atom layer deposition. All ZnO would be etched out only Al₂O₃ nanotubes remain during the immersion in H₃PO₄ solution for 6 min at 25°C. Furthermore, Hong et al.(reference xxx) shows the ZnAl₂O₄ nanotubes synthesized through reaction of core/shell ZnO/Al₂O₃ nanowires involving the Kirkendall effect. When the ZnO/Al₂O₃ nanowires were thermal annealing over 800°C, the ZnO would diffuse into alumina material so that ZnAl₂O₄ nanotubes were formed, as shown in Fig. 2.13. [46]

2.5 ZnO nanostructure in the bio-medical application

Si NWs and carbon NTs are the most studied materials as biosensors. Functionalized Si NWs and carbon NTs have been demonstrated for detecting proteins, DNA and DNA sequence variations, and cancer markers. However, the biocompatibility and biodegradability of these nanostructures remain to be studied. For example, carbon NTs injected into human blood vessels might accumulate and occlude capillaries in the human brain, which could cause serious damage or be fatal. Therefore, ZnO becomes an interesting new material. As

very body knows, the morphology and the dopant concentration of ZnO nanostructures can be well controlled by tuning the growth conditions. ZnO nanoparticles are believed to be nontoxic, biosafe, and possibly biocompatible, and have been used in many applications in our daily life, such as drug carriers and cosmetics. In order to study toxicological impact of ZnO nanoparticles, Brayner et al. first added macromolecules on the ZnO nanoparticles. Then, they studied of biocidal effects and cellular internalization of ZnO nanoparticles on *Escherichia coli* bacteria. These results showed that lower concentrations of ZnO nanoparticles did not induce any damage. Cellular internalization of these nanoparticles was observed in the Figure 2.14. [47]

Roselli et al. and Huang et al. get the similar result to prove that ZnO is a biosafe material.[48] Furthermore, Wang proved that ZnO wires are belong to biodegradability. [49] They have conducted a systematic study on the etching and dissolving behavior of ZnO NWs in various solutions with moderate pH values, including deionized water, ammonia, NaOH solution, and horse blood serum. The result shows that ZnO can be dissolved by deionized water (pH = 4.5–5.0), ammonia (pH = 7.0–7.1, 8.7–9.0) and NaOH solution (pH = 7.0–7.1, 8.7–9.0). The study of the interaction of ZnO wires with horse blood serum shows that the ZnO wires can survive in the fluid for a few hours before they eventually degrade into mineral ions. The results of this study are of great significance. The SEM results are shown in the Figure 2.15. First, biosensors made of ZnO nonmaterial have a certain time to perform a device function. Secondly, once completing the corresponding service, the ZnO wires can eventually dissolve into ions that can be completely absorbed by the body and become part of the nutrition. The biodegradability and biocompatibility of ZnO NWs would allow their use for in vivo biosensing and biodetection.

Generally, ZnO is one luminescent material due to its defects. ZnO quantum dots can enhance the intensity of luminescent emission for bio-image. Wu and co-workers reported that ZnO quantum dots can be used to bio-image by surface modifications. [50] They used Si

gel and TiO_2 to combine with the ZnO. After surface modifications, the samples could be obtain strong visible emission with different thickness, as shown in Figure 2.16. This result showed ZnO quantum dots were suitable in the bio-image applications.

Bio-sensor based ZnO on is a challenging issue. Zhang et al. developed a reagentless uric acid (UA) biosensor based on uricase immobilized on ZnO nanorods. [51] The ZnO nanorods derived electrode retained the enzyme bioactivity and could enhance the electron transfer between the enzyme and the electrode. This sensor showed a high thermal stability up to 85 °C and an electrocatalytic activity to the oxidation of uric acid without the presence of an electron mediator.



Property	Value
Lattice parameters at 300 K:	
a_0	0.32495 nm
c_0	0.52069 nm
a_0/c_0	1.602 (1.633 for ideal hexagonal structure)
u	0.345
Density	5.606 g/cm ³
Stable phase at 300 K	wurtzite
Melting point	1975°C
Thermal conductivity	0.6, 1-1.2
Linear expansion coefficient (/°C)	a_0 : 6.5×10^{-6} , c_0 : 3.0×10^{-6}
Static dielectric constant	8.656
Refractive index	2.008, 2.029
Energy gap	3.4 eV (direct)
Intrinsic carrier concentration	$< 10^6$ /cm ³
Exciton binding energy	60 meV
Electron effective mass	0.24
Electron Hall mobility at 300 K for low n -type conductivity	200 cm ² /V·s
Hole effective mass	0.59
Hole Hall mobility at 300 K for low p -type conductivity	5-50 cm ² /V·s

Figure 2.1 Properties of wurtzite ZnO [16]

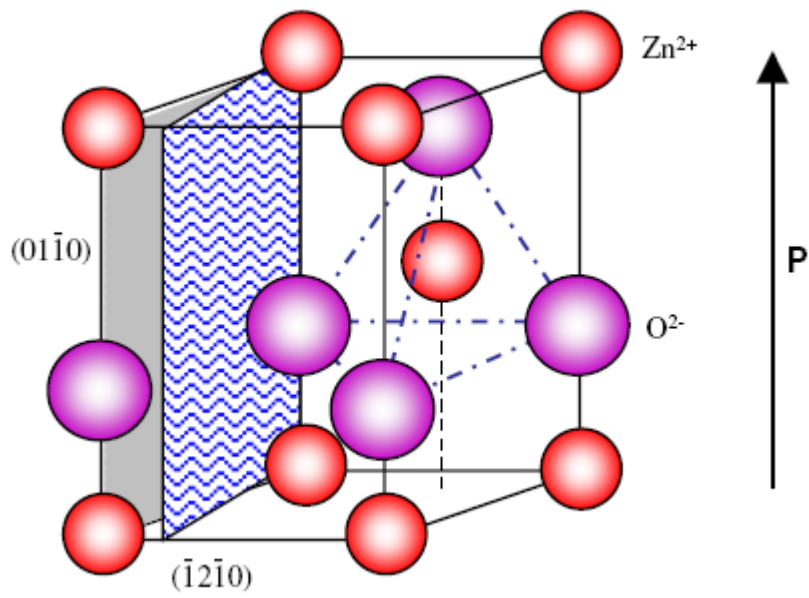


Figure 2.2 wurtzite structure model of ZnO.[17]

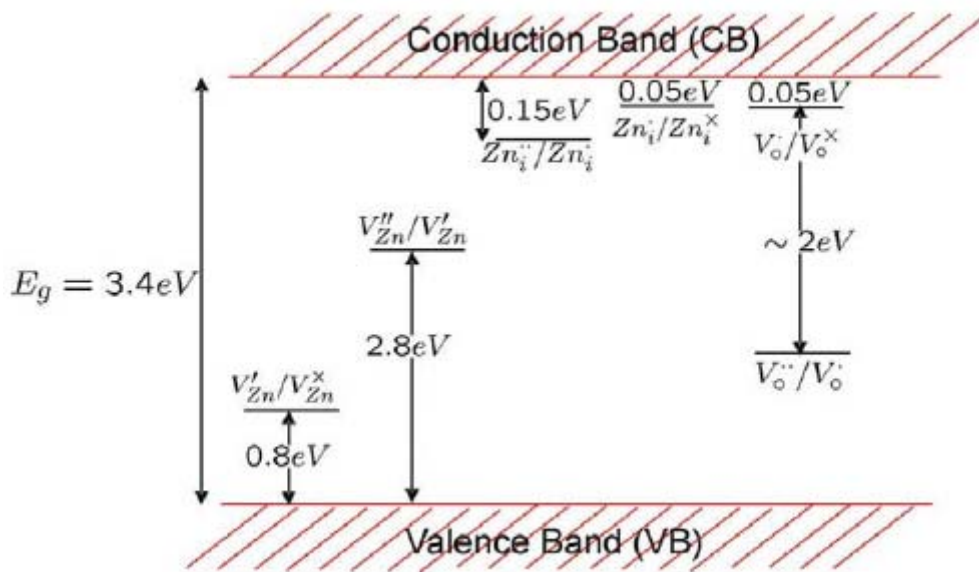


Figure 2.3 Energy levels of native defects in ZnO. [25]

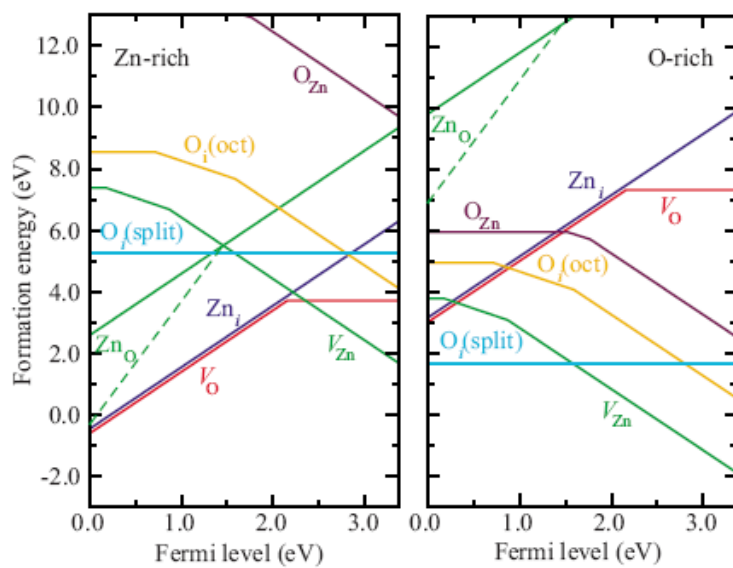


Figure 2.4 Formation energies as a function of Fermi-level position for native point defects in ZnO.[26]

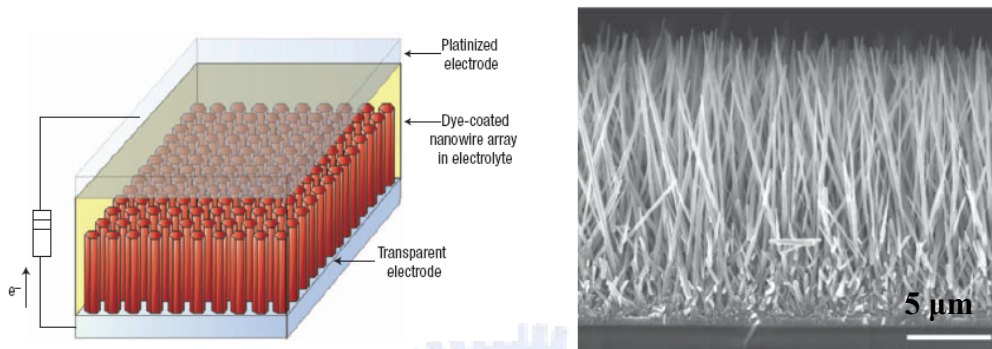


Figure 2.5 A ZnO nanowire dye-sensitized solar cell [28]

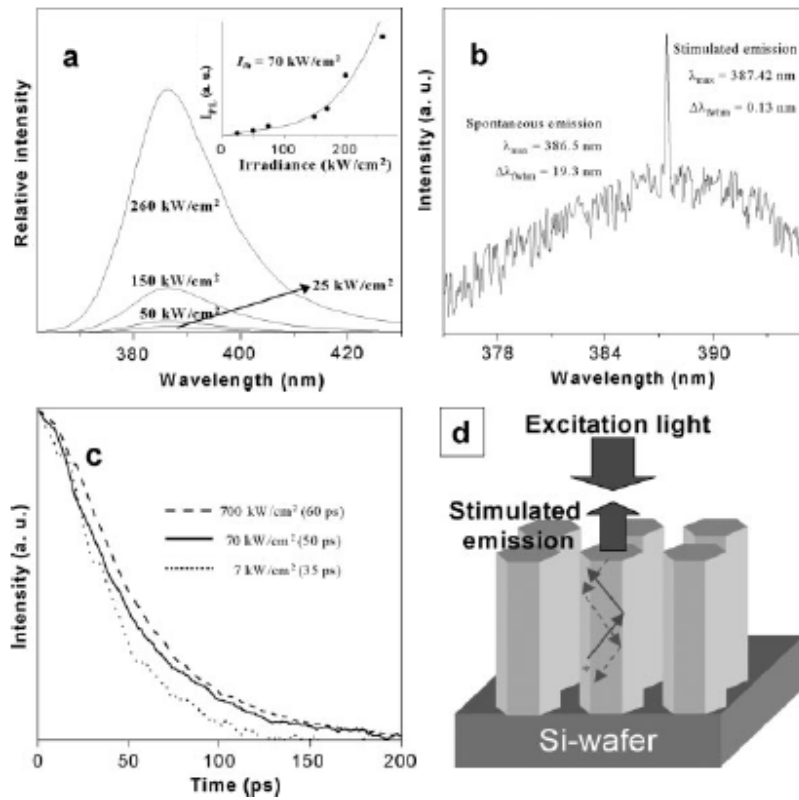


Figure 2.6 ZnO nanorods laser [29]

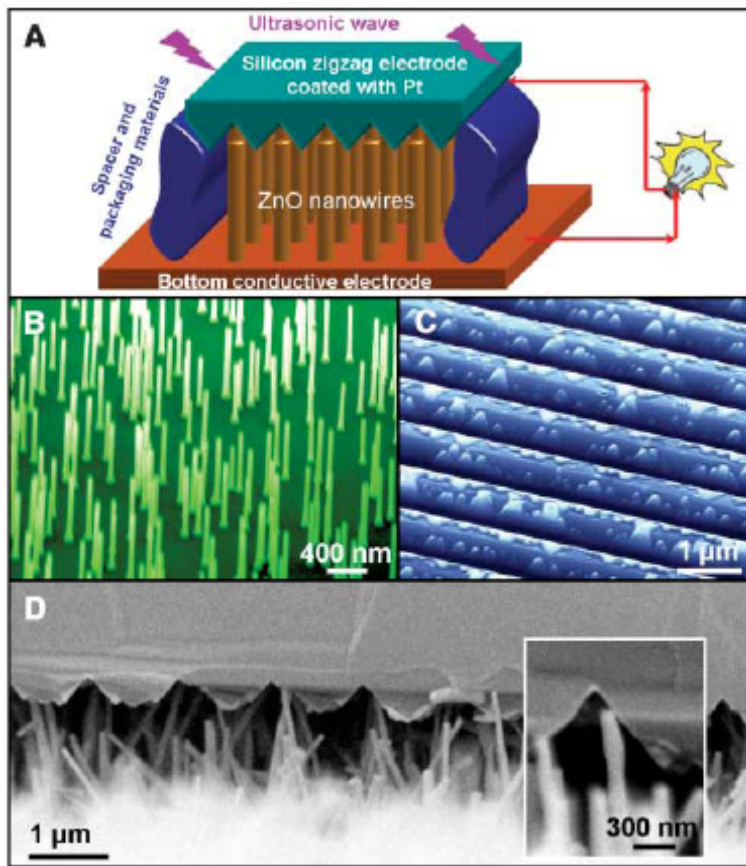


Figure 2.7 Schematic diagram showing the design and structure of the nanogenerator. [30]

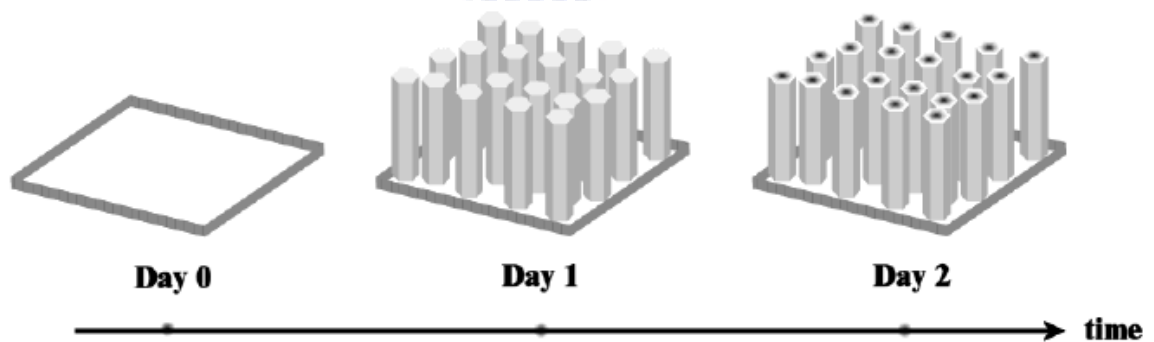


Figure 2.8 Scheme of solution growth of highly oriented microtubular array of ZnO onto substrates [31]

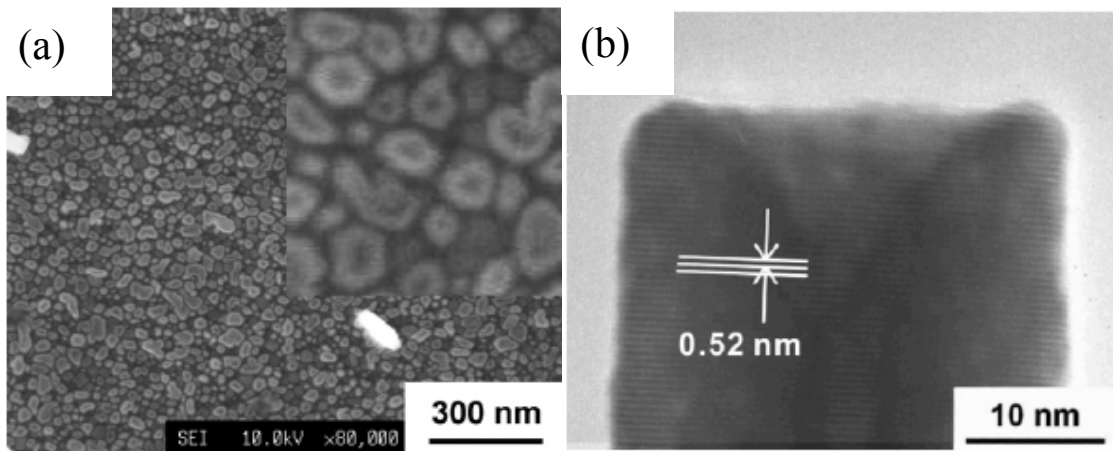


Figure 2.9 (a) Top view SEM image and (b) HRTEM images of the sample grown for 1 h.

[32]

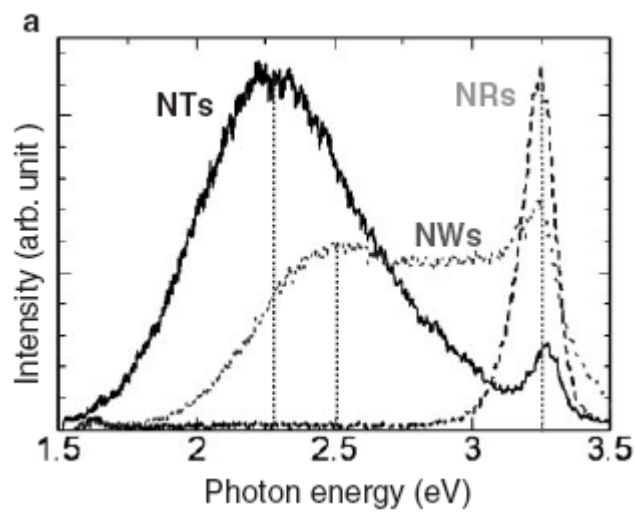


Figure 2.10 PL spectra of ZnO nanotubes nanorods and nanowires [33]

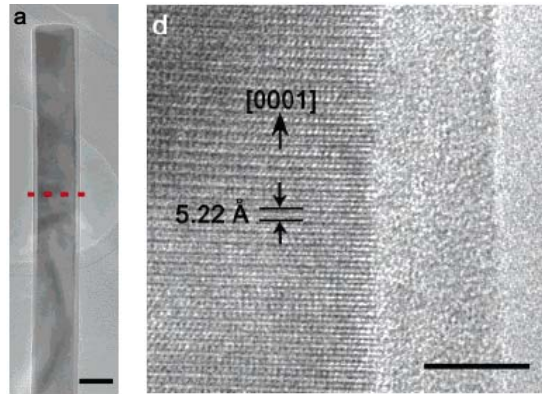


Figure 2.11 TEM characterization of ZnO-Al₂O₃ core-shell nanowires. Scale bar (a) 50 nm (d) 5nm [44]

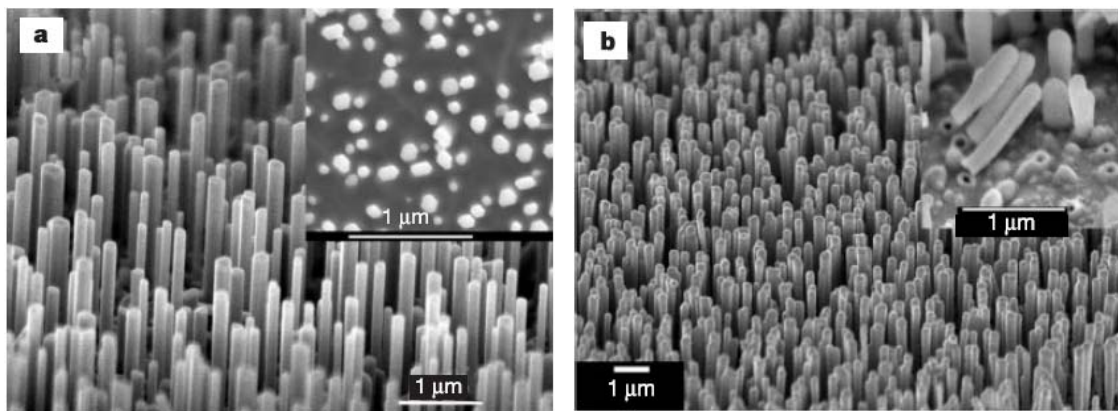


Figure 2.12 Arrays of ZnO nanowires and GaN nanotubes. Shown are SEM images of the ZnO nanowire template arrays (a), and the resulting GaN nanotube array (b). Inset in a shows cross-sections of the ZnO nanowires. [44]

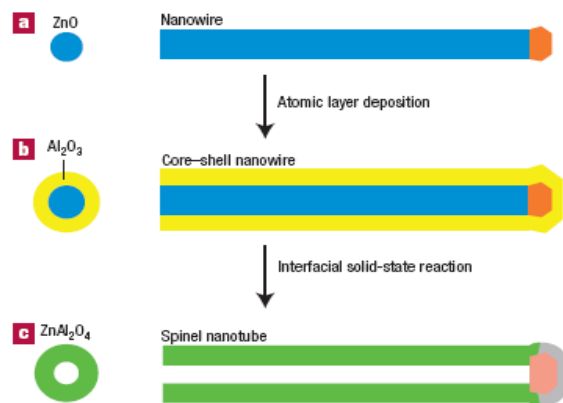


Figure 2.13 Schematic diagram of the formation process of ZnAl₂O₄ spinel nanotubes. [46]

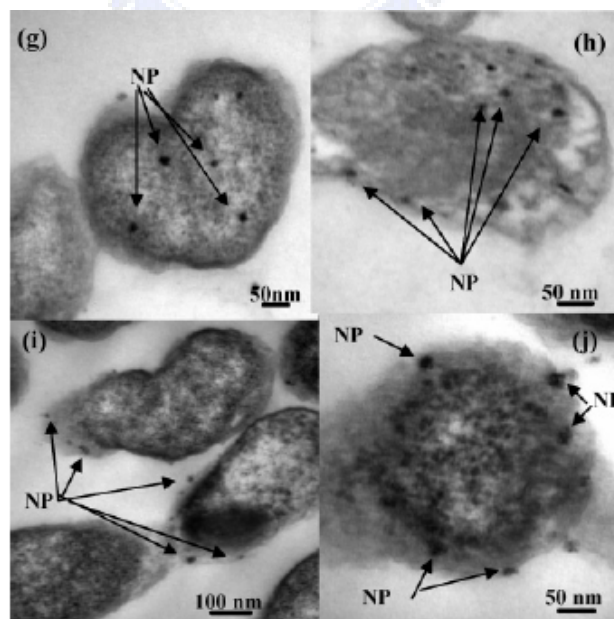


Figure 2.14 TEM micrographs of *E. coli* thin sections (NP = ZnO nanoparticles) (g-j) ZnO nanoparticles (10⁻³ M) internalization.[47]

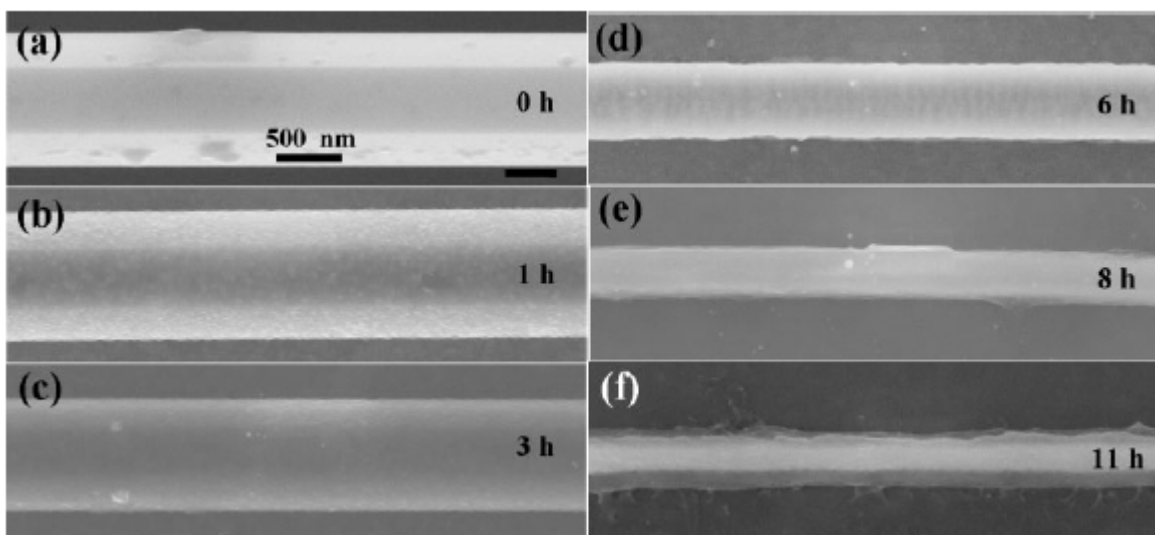


Figure 2.15 SEM images of a ZnO wire that has interacted with horse blood serum diluted in 10% aqueous NaOH solution (pH = 7.9–8.2) for different lengths of time. [49]

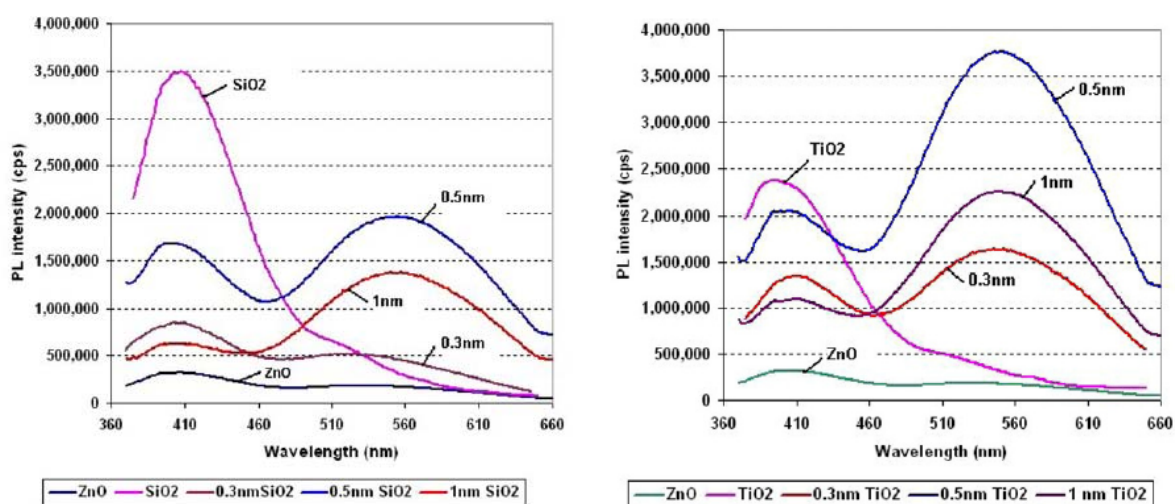
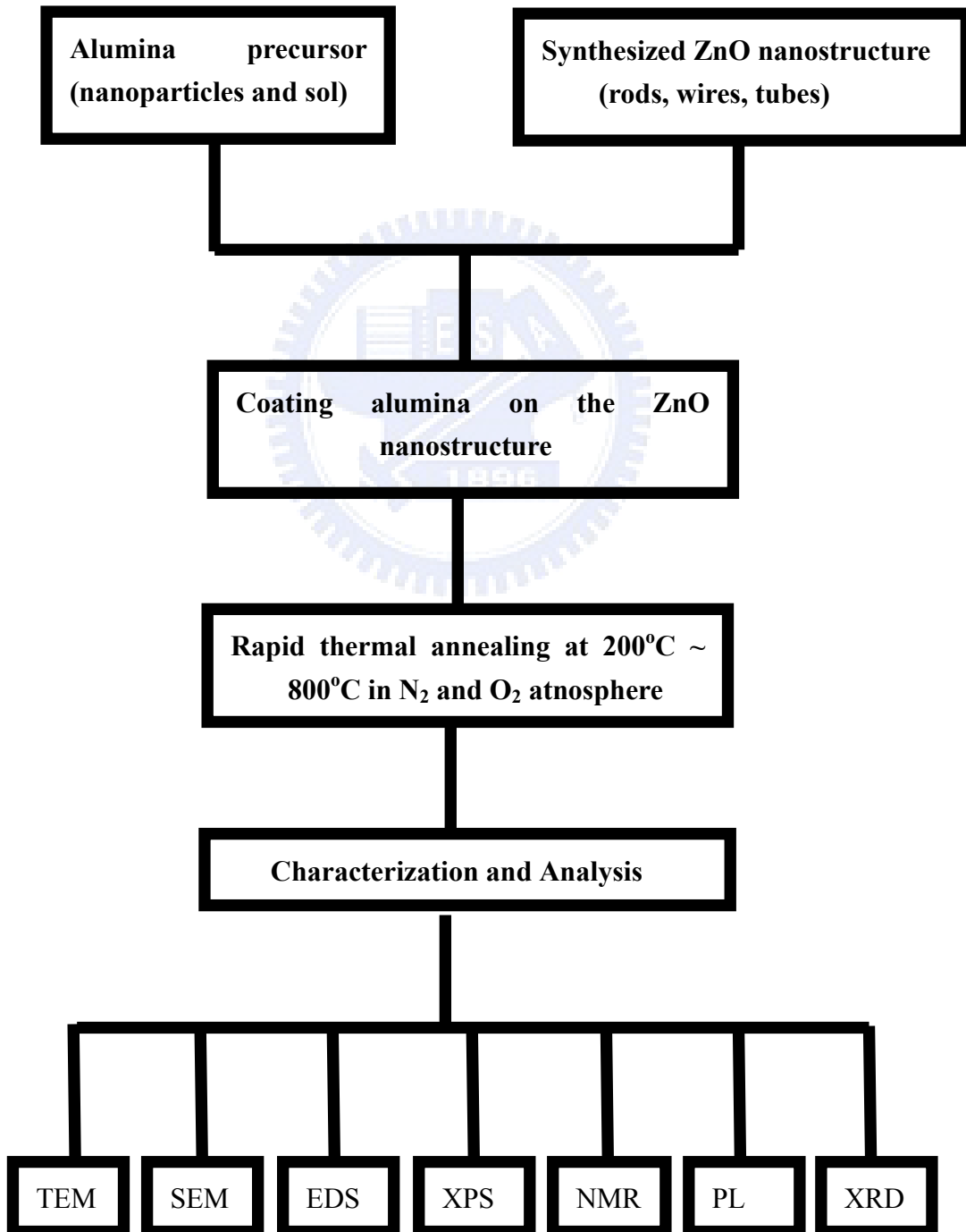


Figure 2.16 Photoluminescence spectra of SiO₂ and TiO₂ –coated ZnO [50]

Chapter 3

Experimental materials and methods

3.1 Flow chart of experimental procedure



3.2 ZnO thin films formation

The ZnO thin films (~100 nm) were deposited on 4 in. diam Si substrates by radio frequency (rf) magnetron sputtering using 99.99% ZnO as the target. The growth chamber was evacuated by a turbo pump and a mechanical pump. The gas mole ratio of oxygen to argon (OMR) was varied in the range of 5%. The silicon substrates were cleaned by the usual semiconductor technology before loading into the chamber. The sputtering conditions were optimized at a substrate temperature of 50°C, an rf power of 50 W, a sputtering pressure of 10 mTorr, and a sputtering time of 40 min.

3.3 Wet-chemical growth of ZnO nanorods and nanotubes

Zinc nitrate hexahydrate ($\text{Zn}(\text{NO}_3)_2 \cdot 6\text{H}_2\text{O}$) was used as zinc precursors to synthesize ZnO nanorods (ZNs) and nanotubes (ZTs). Methenamine ($\text{C}_6\text{H}_{12}\text{N}_4$), also called hexamethylenetetramine (HMT), is a highly watersoluble, non-ionic tetradentate cyclic tertiary amine and used to comply simultaneously with the precipitation of the divalent post-transition metal Zn^{2+} ions, the nucleation growth of its stable oxide form, zincite ZnO. Two kinds of substrates, one Si and the other Si coated with ZnO film, were also used. An equimolar (0.02M) aqueous solution of $\text{Zn}(\text{NO}_3)_2 \cdot 6\text{H}_2\text{O}$ and HMT was prepared in a bottle. Subsequently, substrates were placed inside the aqueous solutions and heated in the temperature range of 55–95 °C for 0.1–48 h. Usually, ZnO nanorods were grown at 75°C and ZnO nanotubes were grown at 95°C. After that, the substrates were removed from the aqueous solutions, rinsed with distilled water, and dried at roomtemperature overnight.

3.4 Wet-chemical synthesis of alumina nanoparticles and nanofilms

Following the sol-gel porous alumina templating method proposed by Martin et al. 5 M ammonia was added to an aqueous alumina nitrate solution (0.4 M) at room temperature. Then, the solution was controlled to the pH = ~10 to form hydrated precipitate. After the hydrated precipitate was formed, it was centrifugally separated and washed several times with distilled water. The precipitate was dry in the oven for 12 hours. Then, the alumina nanoparticles can be obtained. On the other hand, the precipitates were put into 100 ml D. I. water. Then, the solution was peptized with nitric acid and control the pH = 6.5 ~ 7.5. A translucent, homogeneous and stable sol was obtained.

3.5 Synthesis and thermal treatment of alumina/ZnO core/shell structure

The ZnO nanorods were subsequently immersed in the precursor sol of Al³⁺ to grow an alumina shell on the ZnO nanorods at 80°C for 1 hr. The thickness of alumina shell on the ZnO nanorods can be modulated by controlling reaction parameters, such as reaction time and temperature. The alumina-coated ZnO nanocables were obtained.

The alumina nanoparticles was dispersed in the water solution by ultra-sonication and adjusted to pH 8.0 with ammonia. The nanoparticles with pseudoboehmite phase (γ -AlO(OH)) will absorb OH⁻ ions to form -OO- Al - OH₂⁺ on the surface. Then, the ZnO nanotubes will react with -OO- Al - OH₂⁺ precursor to deposit alumina nanoparticles on the ZnO nanotubes after immersed into the solution at 120°C for 1 hr.

After washing the alumina-coated ZTs with distilled water, rapid thermal annealing (RTA) was performed for 20 minutes under oxygen and nitrogen atmospheres. The annealing parameter: raising temperature , 10 °C/min to 200°C, 400°C, 600°C and 800°C and holding the temperature. The samples were inserted into the tube at fix temperature and hold during 20 minutes. Finally, the samples were drawn out after 20 minutes.

3.6 Characterization of ZnO and alumina materials

An X-ray diffractometer (M18XHF, MAC Science, Tokyo, Japan) was used to examine the crystalline phase of the synthesized compounds with a scanning rate of 4° (2θ) per min over a 2θ range of $10\sim 70^\circ$. Cu K α radiation was used and the operating voltage was 50 kV. The growth morphology of the ZnO nanorods was examined by field emission scanning electron microscopy (FE-SEM, JOEL-6700). The samples were analyzed with a field emission transmission electron microscope (TEM, JEOL 2100F) with energy dispersive x-ray spectroscopy (EDS) operated at 200 keV. Room-temperature PL measurements were performed with a 325 nm He–Cd laser with an excitation power of 25 mW. The emitted luminescence was detected with a 0.32 m spectrometer with a charge-coupled device detector. The focused spot size of the He–Cd laser was estimated to be about $200\ \mu\text{m}$ in diameter. The Fourier Transform Infrared spectrometry (FTIR, PerkinElmer spectrum 100) was used to examine the alumina bonding during the thermal treatment process. A scanning number was 4 times: the resolution was $4\ \text{cm}^{-1}$: the scanning range was $450\sim 4000\ \text{cm}^{-1}$. The ^{27}Al MAS NMR was used to examine the chemical shift of alumina-coated ZnO nanorods scraped from the Si substrate using a Bruker Dsx400wc NMR Spectrometer. X-ray photoelectron spectroscopy (XPS) was used to evaluate Al-O chemical binding states. The XPS analyses were performed on a Kratos AXIS Ultra with a monochromatic Mg X-ray source at 150W.

Chapter 4

Tunable growth of ZnO nanorods synthesized in aqueous solutions at low temperatures

4.1 Introduction

One-dimensional ZnO nanocrystals have been extensively studied because of their promising chemical and physical properties,[52] and show potential applications in manufacturing electronic and optoelectronic devices.[53.54] In the past, a variety of methods have been employed, including vapor phase transport, metal-organic chemical vapor deposition to grow arrayed nanorods and nanowires of ZnO from aqueous solutions. Recently, many wet-chemical approaches have been developed to prepare oriented arrays of ZnO nanorods on polycrystalline (or single crystalline) substrates from aqueous solutions. Choy et al. reported that the buffer layer of dip-coated ZnO nanoparticles can effectively reduce the mismatch between the Si substrate and the ZnO nanorods.[55] Our previous report also suggested that on a Si wafer coated with a ZnO film, well-aligned ZNs with different aspect ratio can be grown along the [0002] direction on the Si substrate coated with ZnO film (ZnO_f/Si substrate).[56] All the observations reveal that the undercoating ZnO film plays a very important role in the development of ZNs. However, no systematical studies have been performed up to now. Therefore, the growth condition of the ZnO nanorods was first studied. Then, we investigate the effect of annealing treatment of the undercoating ZnO film on the growth behavior of ZNs. Furthermore, it was found that the ZNs can be selectively grown on

a patterned ZnO film which can serve as seeds to modify the morphology of ZNs by controlling the annealing condition of the coated ZnO film on any substrates.

4.2 ZnO nanorods with different growth parameters

Figure 4.1 shows the morphology of the ZNs with different concentrations (0.0025M 、 0.01M 、 0.004M and 0.08M) at 75°C for 10 hours. When the concentration was 0.0025M, it could be observed few and small ZNs. With increasing the concentration, the density of the ZNs would be increased. When the concentration was over high (0.08M), the morphology of ZNs would look like nanorod film, indicating too high density, as shown in the figure 4.1(d). The diameter of the ZNs would be reduced with the decrease of the solution concentrations. Because low Zn⁺ concentration would reduce the growth rate of the ZNs, small ZNs were obtained. The X-ray diffraction patterns (XRD) in Fig. 4.2 presents the growth orientation and crystalline of the ZNs. It can be obtained three main peaks (31.7, 34.4 and 36.2) which fit the wurzite structure by JCPDs card. When the solution concentration was 0.0025M and 0.01M, the (002) peak intensity was weak, indicating that the crystalline of the ZNs was not strong.

Figure 4.3 shows the morphology of the ZNs with growth temperature (55 °C, 65 °C, 75 °C and 85 °C) in 0.04 M for 10 hours. When the growth temperature increased from 55 °C to 85 °C, it could be observed the average diameter of the ZNs increased from 30 nm to 120 nm. When the growth temperature was below 50°C, it can not be obtained any ZNs because chemical reaction do not overcome the active energy barrier. The (002) intensity of the ZNs was weak when the growth temperature was 55 °C and 65 °C, as shown in the Fig. 4.4 Moreover, the (100) peak was so obvious, indicating that some ZNs were not grown vertically on the substrate. When the growth temperature was increased to 75 and 85 °C, the ZNs owned high crystalline and single orientation.

Figure 4.5 shows the atomic force microscopy (AFM) images of the ZnO film sputtered on

Si substrate (ZnO_f/Si) at different annealing temperatures. It was found that that the grain size of the ZnO film on Si substrates becomes larger and the surface morphology becomes rough with the increase of annealing temperature. Furthermore, it can be observed in Fig. 4.5(b) that many abnormally large ZnO grains were grown on the ZnO_f/Si substrate annealed at 800°C . Furthermore, according to our previous study, it was found that the diameter of ZnO nanorods was affected by the concentrations of the aqueous solution. Therefore, the same concentration of the precursors (0.01M) was used in this work to avoid the effect of solution concentration.

4.3 Patterned growth of the ZnO nanorods

Figure 4.6 shows the SEM images of the ZNs grown on the patterned ZnO_f/Si annealed at different temperatures, where the patterned ZnO film on Si substrate was fabricated by the photolithography and etching process. As the patterned ZnO_f/Si substrate was placed into the aqueous solution to grow ZNs, well-aligned ZNs are grown on the designed substrate, as shown in Fig. 4.6(a), and this demonstrates the selected growth behavior of the ZNs. Figure 4.6(b) shows the surface images of large-scale arrayed ZnO nanorods grown on the patterned ZnO_f/Si at room temperature and the ZnO nanorods have a well-defined hexagonal plane with a homogeneous diameter. Although the ZnO_f/Si substrate was patterned, nucleation of the nanorods was not correlated with the substrate patterning and subsequent growth of the ZnO grains was also unaffected by patterning. However, as the patterned substrates were first annealed at 600°C and 800°C , prior to the growth of the ZNs in the solution at 75°C , we found that the morphology of the ZNs was markedly changed, as shown in Fig. 4.6(c) and (d), especially for the ZnO_f/Si annealed at 800°C . Furthermore, the dimension of ZNs increases with increasing annealing temperature. The average dimension of the ZNs is 20 nm and 300 nm in diameter for the ZnO_f/Si at room temperature and annealed at 800°C , respectively. When compared with the AFM images of ZnO film on Si substrate shown in Fig. 4.5, this

seems to imply that the growth behavior of the ZNs is correlated with the grain size of the ZnO film sputtered on Si substrate, as illustrated in Fig. 4.7. Furthermore, there exists a critical temperature around 400°C, and above that, the ZNs are rapidly grown and become larger in diameter.

4.4 The relation between ZnO film and ZnO nanorods

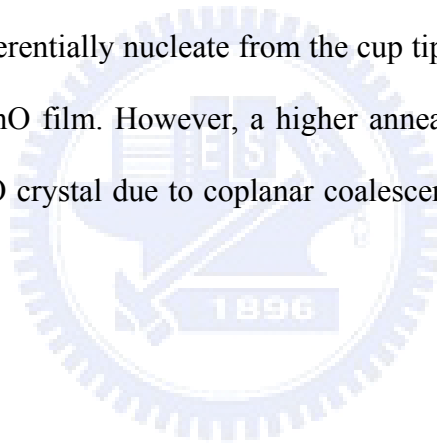
Figure 4.8(a) shows the TEM bright-field (BF) image of the aligned ZNs grown on the annealed ZnO_f/Si substrate at 600°C. It was observed that most of the ZNs were grown along the direction perpendicular to the ZnO_f/Si substrate. The TEM dark-field image marked with arrows in the Fig. 4.8(b) reveals that there exists a close relationship between ZNs and ZnO film. Both ZNs and ZnO_f on Si substrate were grown along the same direction of [0002] and are coherent, as demonstrated by the selected-area electron diffraction pattern (SAED) (inset of Fig. 4.8(b)). In addition, as one observes the interface between ZNs and ZnO_f/Si shown in Fig. 4.8(c), the HR-TEM image (magnified from the marked area in Fig. 4.8(a)) reveals that both the ZNs and ZnO film have identical parallel lattice fringes. This indicates that the ZNs seem to nucleate from the concave tip near the grain boundary (marked as lines) between two ZnO grains in ZnO films because it (near the concave tip) has a higher surface energy. A detailed discussion can be referred to Ref. 5.

As the ZnO_f/Si substrate was annealed at a higher temperature of 800°C, a low-magnification TEM image of the ZNs was shown in Fig. 4.9(a). The HR-TEM image of the ZNs marked with the box in Fig. 4.9(a) was further illustrated in Fig. 4.9(b) where some nanorods are merged together to form a larger ZN along similar growth direction [0002].[57] The selected area diffraction pattern (SADP) (shown in the inset of Fig. 4.9(b)) reveals that the diffraction spots were split with several different angles. This suggests that the larger ZNs are not perfectly single-crystalline and consist of three ZNs, as illustrated in Figs. 4.9(c), (d)

and (e), with a slight misalignment between the nanorods. Therefore, the growth behavior of the larger ZnO nanorods can be considered from the direct combination of a small number of individual nanorods having a similar orientation.[58]

4.5 Summary

We demonstrated that the growth of patterned ZnO nanorods can be controlled by changing the annealing conditions of the ZnO_f/Si substrates. When the ZnO_f/Si substrate was annealed above a critical temperature to promote the crystallization of ZnO phase, both ZNs and ZnO_f on Si substrate were found to become crystallographically matched. In this work, it reveals that the ZNs seem to preferentially nucleate from the cup tip near the grain boundary between two ZnO grains in the ZnO film. However, a higher annealing temperature may lead to the formation of a larger ZnO crystal due to coplanar coalescence behavior of several individual ZnO nanorods.



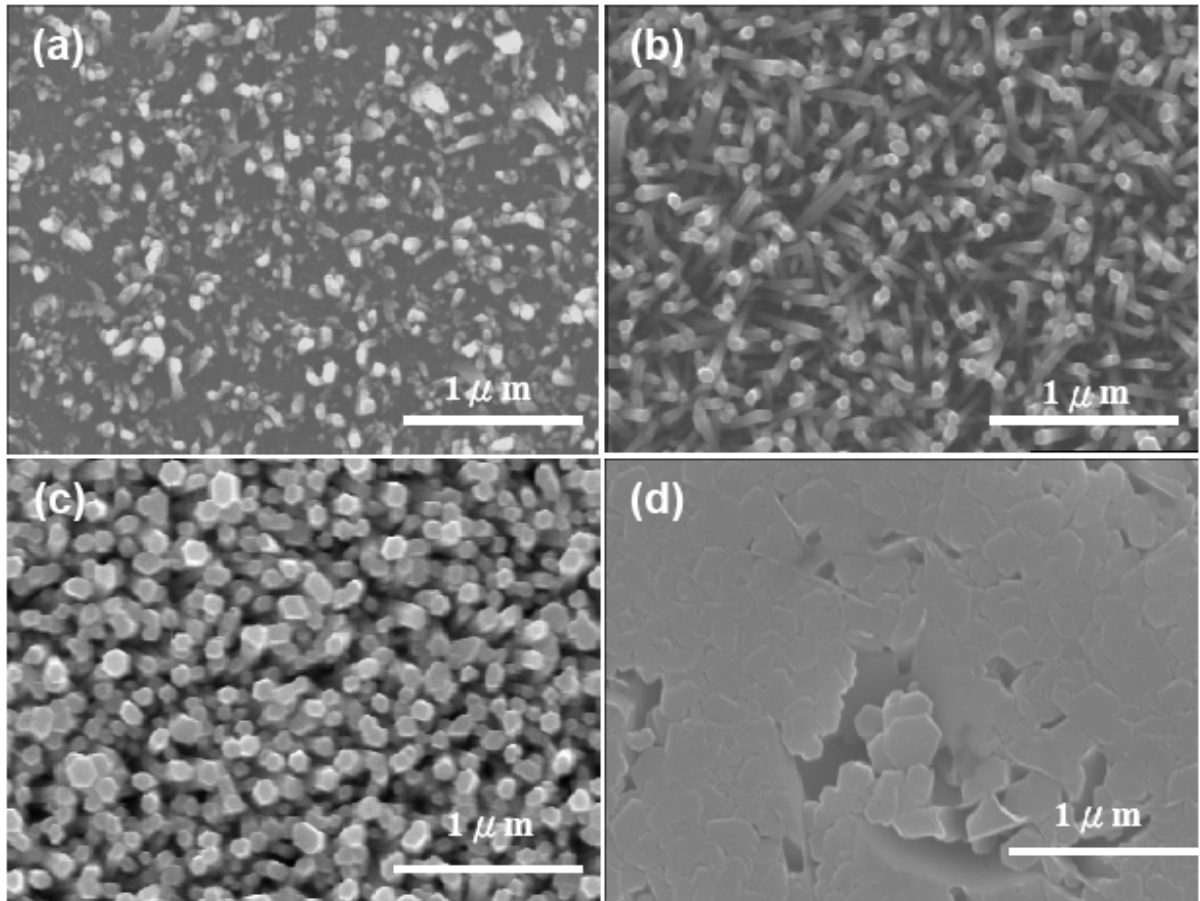


Fig. 4.1 SEM image of the ZNs synthesized in (a) 0.0025 M (b) 0.01 M (c) 0.04 M (d) 0.08 M

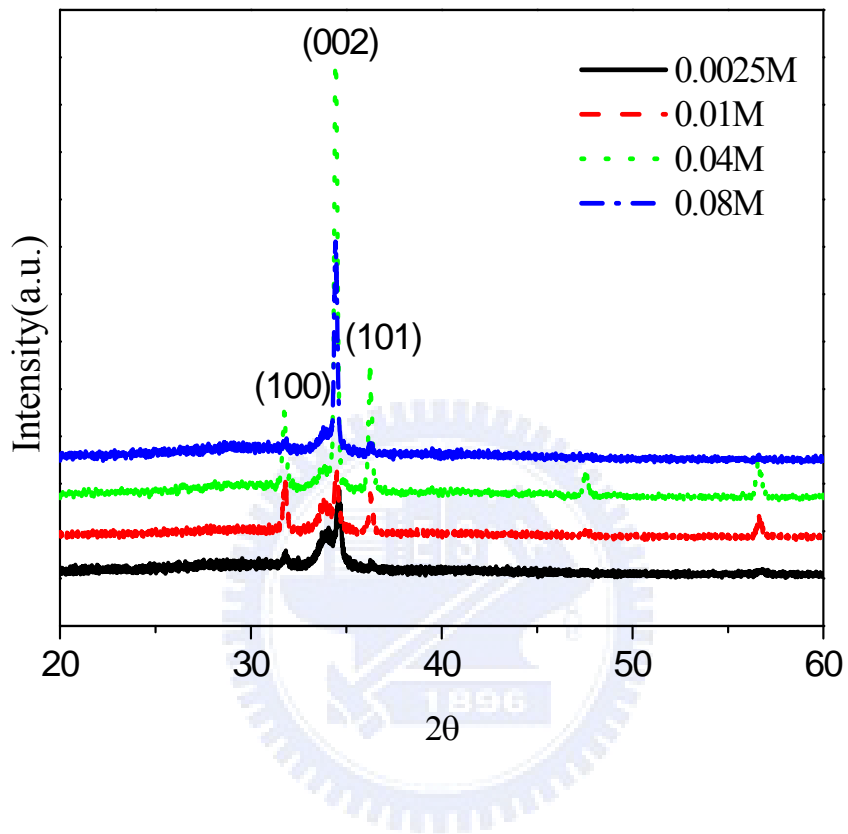


Fig. 4.2 XRD analysis of the ZNs synthesized in different concentrations.

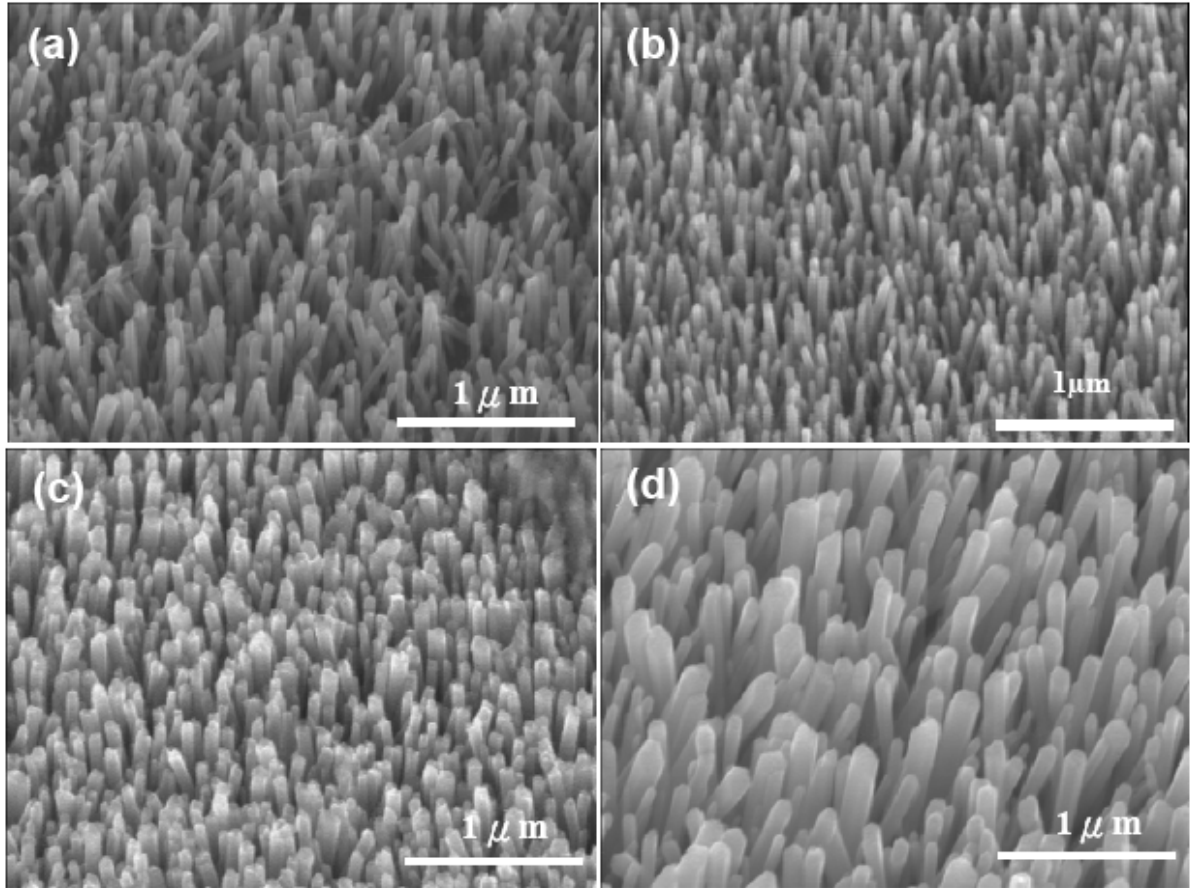


Fig. 4.3 SEM image of the ZNs synthesized at (a) 55 °C (b) 65 °C (c) 75 °C (d) 85 °C.

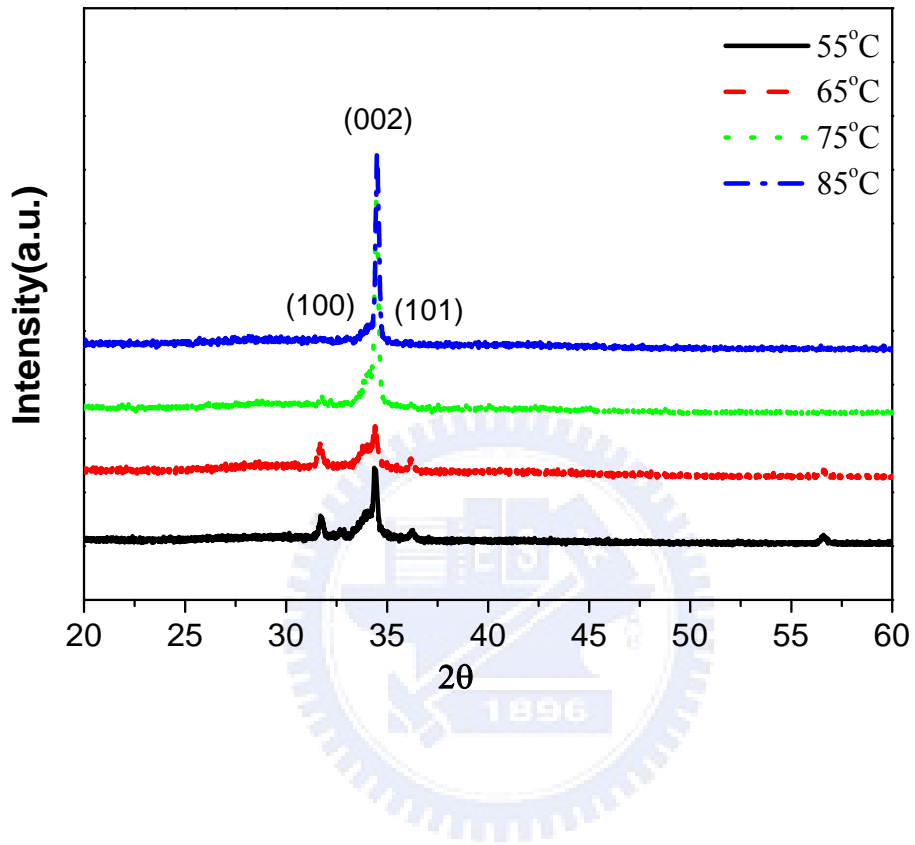


Fig. 4.4 XRD analysis of the ZnO synthesized in different growth temperature.

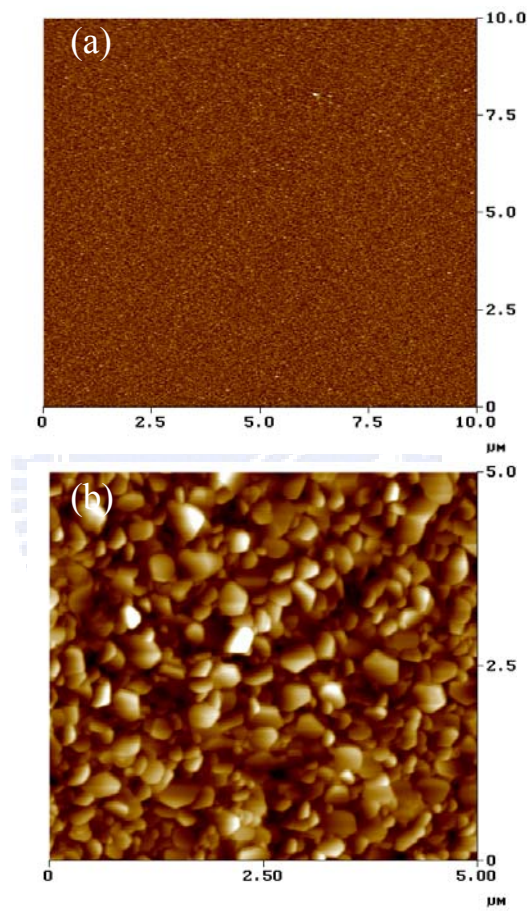


Fig. 4.5 AFM images of (a) as-grown ZnO films and (b) annealed ZnO film at 800°C.

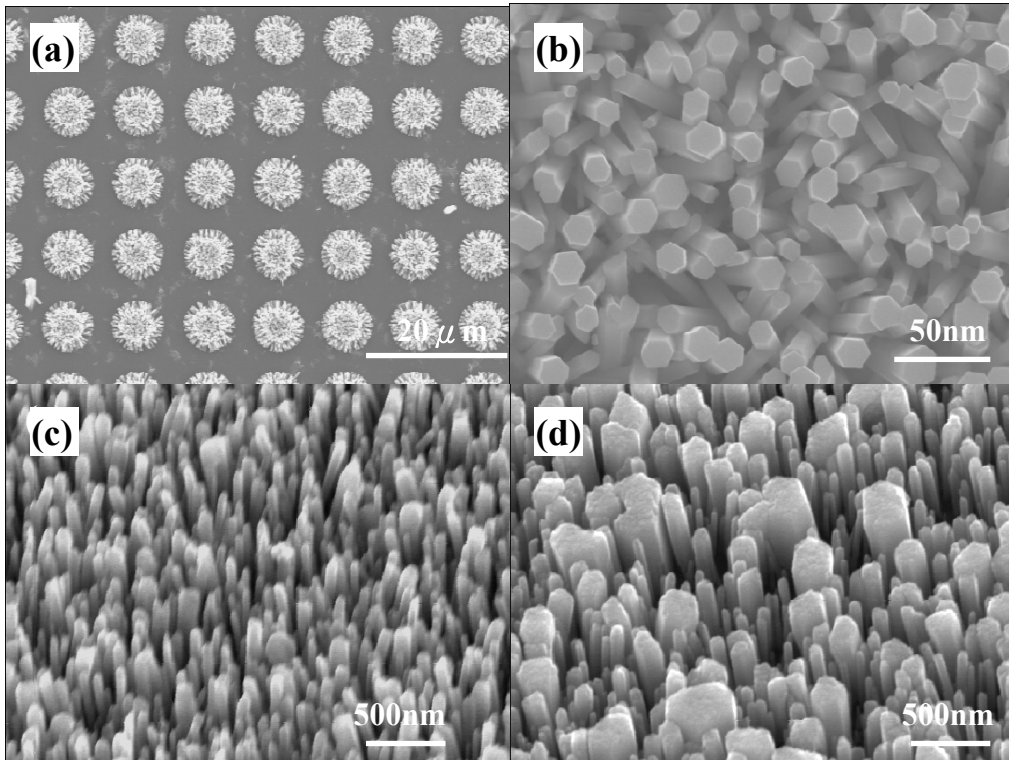


Fig. 4.6 SEM images of the ZnO nanorods (a) grown on the patterned ZnO_f/Si, (b) grown at

room temperature, and grown on the annealed ZnO_f/Si at (c) 600°C and (d) 800°C.

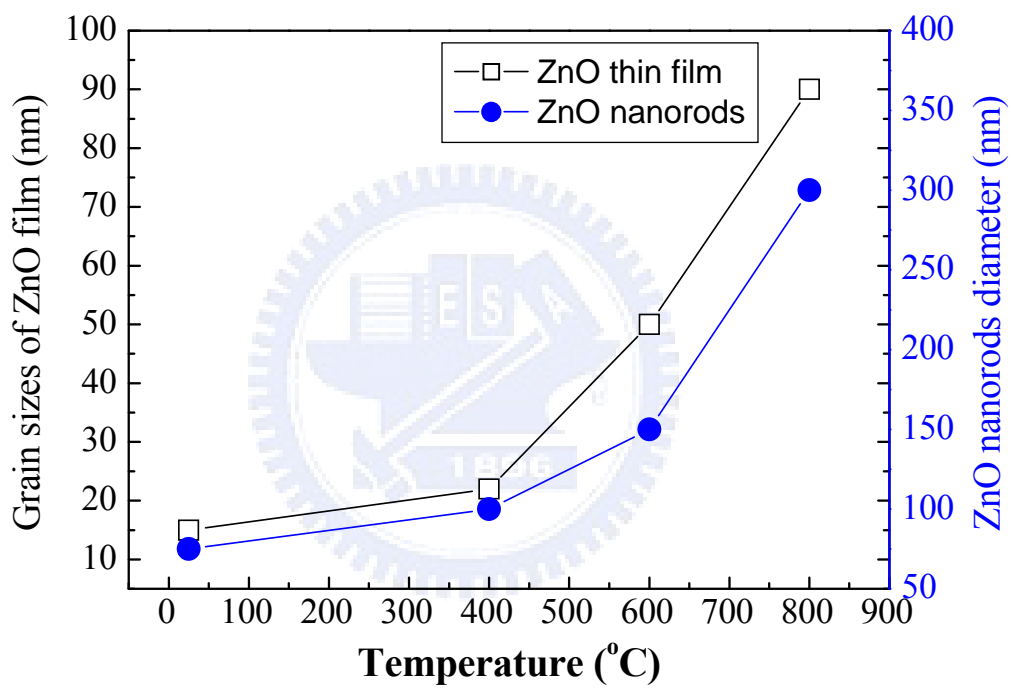


Fig. 4.7 Both ZNs diameter and ZnO_f grain size as a function of annealing temperature.

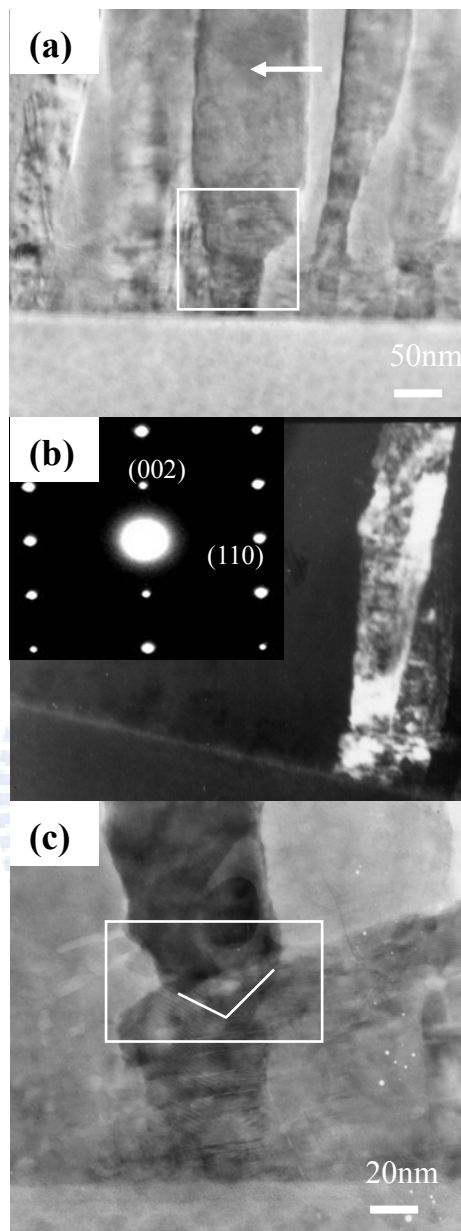


Fig 4.8 (a) TEM bright-field and (b) dark field images of the aligned ZNs grown on ZnO_f/Si substrate annealed at 600°C . A corresponding diffraction pattern is shown in the inset of Fig. (b) for the selected single nanorod. (c) A high-resolution TEM image of (a) showing the interface between ZNs and ZnO_f .

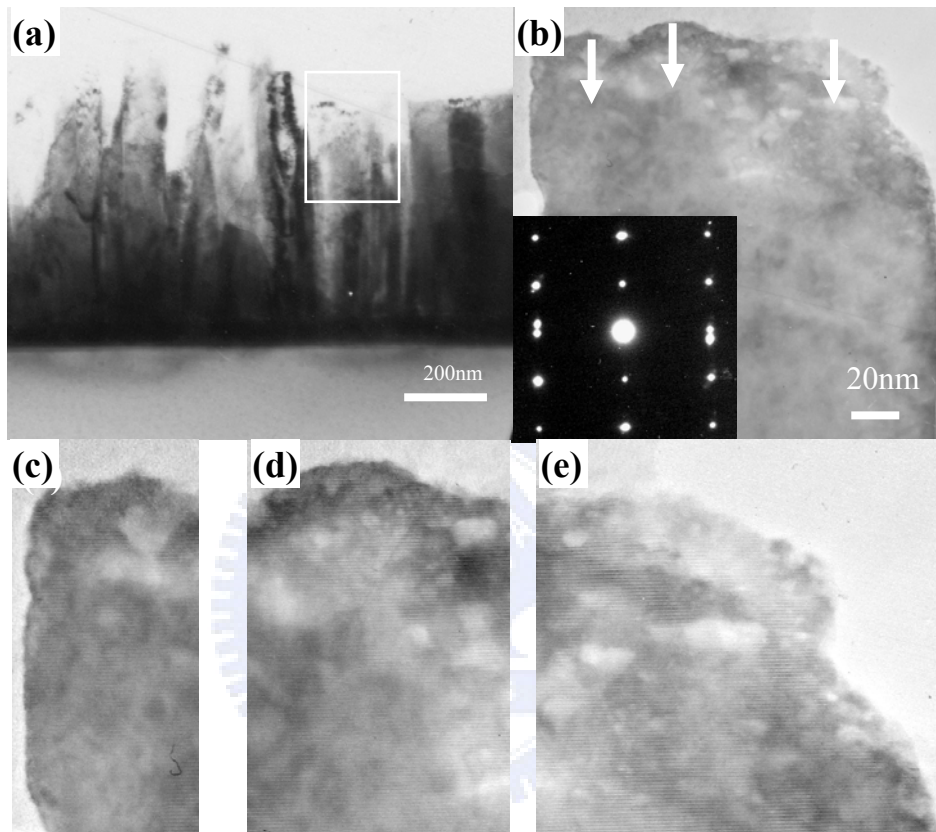


Fig. 4.9 (a) Showing the low-magnification TEM images of ZnO nanorods grown on the annealed ZnO_r/Si at 800°C. (b) HRTEM images of the ZnO nanorods marked in the frame of (a) along with split diffraction pattern in the inset. HRTEM image of (c) left, (d) middle and (e) right side of the larger nanorod, showing the larger ZnO nanorod seems to be composed of three ZNs.

Chapter 5

Growth behavior and microstructure evolution of ZnO nanorods grown on Si in aqueous solution

5.1 Introduction

One-dimensional (1D) semiconductor nanostructures have been extensively studied for their potential applications in manufacturing electronic and optoelectronic devices [59]. Zinc oxide (ZnO) is an important electronic and photonic material because of its wide and direct band gap (ΔE_g 3.37 eV) material [60]. The strong exciton binding energy of ZnO (60 meV) is much larger than that of GaN (25 meV), which can ensure an efficient exciton emission at room temperature. Recently, highly oriented nanorod arrays of ZnO nanostructures have demonstrated their potential applications in manufacturing electronic and optoelectronic devices [61,62]. Various methods, including chemical, electrochemical, and physical deposition techniques have been employed to synthesize 1D ZnO nanostructures such as catalytic growth via the vapor–liquid–solid (VLS) epitaxial method [63] and metalorganic-chemical vapor deposition (MOCVD) [64]. However, those methods are expensive and energy consuming processes since they are operated under extreme conditions. On the other hand, many wet-chemical approaches have been used for large oriented arrays of ZnO nanorods on polycrystalline (or single-crystalline) substrates from aqueous solutions [65]. It is well conceived that the preparation of ZnO via solution chemical routes provides a promising option for large-scale production of these materials. Recently, Vayssieres et al. has proposed a novel theoretical concept, called “purpose-built materials”, to grow arrayed

nanorods and nanowires of ZnO from aqueous solutions [66]. Such an approach does not require any template, membrane or applied external field to create anisotropic nanoparticles. However, it is worth noting that without suitable treatment on the substrate, highly oriented ZnO nanorods grown on a Si wafer have been rarely achieved due to the larger mismatch (~40%) between the substrate and the ZnO nanorods. Yamabi et al. reported that without undercoats on the surface, clusters of spindle-shaped hexagonal crystallite with diameters of 0.5–1.0 μm were scattered over the surface of a silicon wafer, but highly aligned arrays of ZnO nanorods with diameters of 20–100 nm can be developed on Si substrate undercoated with $\text{Zn}(\text{Ac})_2$ and annealed at 500 $^\circ\text{C}$ [67]. Recently, Choy et al. also found that high-quality ZnO nanorods were successfully grown on a Si wafer by a wet-chemical process at 95 $^\circ\text{C}$ for 6 h, where the Si wafer was dip-coated with 4 nm sized ZnO nanoparticles as a buffer and seed layer prior to crystal growth [68]. These observations reveal the importance of surface characteristics or treatment on the growth of well-oriented ZnO nanorods in aqueous solution. However, little investigation has paid attention to the growth behavior of such ZnO nanorods, in particular to tailor their orientation onto the substrates that can be used to control the structure morphology and optoelectronic properties. Therefore, in this work, a simple wet-chemical method was used to study the growth behavior of both scattered and aligned ZnO nanorods on Si by monitoring the average aspect ratio of ZnO nanorods as a function of growth time in aqueous solution. By controlling the experimental conditions, scattered or well-aligned ZnO nanorods with different aspect ratios can be obtained. Moreover, high-resolution transmission electron microscopy (HRTEM) was performed to investigate the microstructure evolution of both ZnO nanorods.

5.2 Phase and morphology of ZnO nanorods grown on different substrates

Two substrates, i.e., Si and ZnO-coated Si, were used in this work to study the growth

behavior of ZNs in the precursor solution at different temperatures of 55–95 °C for several hours. No ZNs were observed below 50 °C, indicating that a thermal barrier for the growth of ZNs cannot be overcome. Above 95 °C, ZNs cannot be synthesized because the reaction temperature is near the melting point of the aqueous solution. Fig. 5.1 shows the SEM images of the as-synthesized ZNs grown on these two kinds of substrates at 75 °C for 10 h in the 0.02M solution. As shown in Fig. 5.1(a), ZNs with dimensions of 7~10 mm in length and 0.5~1 mm in diameter were scattered on the Si substrate. On the other hand, high densities of well-aligned ZNs with dimensions of 20–200nm in diameter and up to several mm in length were obtained when ZNs were grown on ZnO_f/Si as shown in Fig. 5.1(b). It seems to imply that the formation of well-aligned ZNs on a pure Si substrate is difficult because a large mismatch (~40%) exists between ZnO and Si. Hence, this would retard the nucleation of ZnO nanorods on Si substrate. This observation strongly reveals the importance of the substrate characterization on the growth behavior of ZNs in the aqueous solution.

The X-ray diffraction patterns (XRD) in Fig. 5.2 show that the ZnO crystal phase starts to appear at 50 °C and is well crystallized above 65 °C. A strongly oriented peak can be indexed as the wurtzite ZnO at 75 °C in 0.02M aqueous solutions for the ZNs grown on Si and ZnO_f/Si substrate. However, it should be pointed out that a remarkable difference in XRD patterns exists between these two substrates. As shown in Fig. 5.2(a), the diffraction peaks were indexed as (1 0 0), (0 1 0) and (1 0 1) planes of ZnO for the ZNs grown on Si substrate. On the other hand, Fig. 5.2(b) illustrates that the strongest diffraction peak corresponding to the (0 0 2) plane of ZnO was detected when the ZNs were grown on ZnO_f/Si substrate. These observations obviously reveal that there exists different growth behavior between (1 0 0)-oriented (called scattered) ZNs on Si and (0 0 2)-oriented (called aligned) ZNs on ZnO_f/Si.

5.3 Microstructural analysis of ZnO nanorods

ZnO has a hexagonal lattice with a c/a axial ratio of 1.602 [69]. The most commonly observed morphologies of ZnO are either rod-like or needlelike crystals, especially the prepared ZnO in aqueous solution because of anisotropic crystal growth. The TEM bright-field (BF) image and corresponding selected-area diffraction pattern (SADP) of the scattered ZNs are shown in Figs. 5.3(a) and (b), respectively. The SADP in Fig. 5.3(b) clearly indicates that the scattered ZNs were grown along the $[01\bar{1}0]$ direction. This result is also consistent with the XRD analysis that the ZNs are preferentially oriented along the $[01\bar{1}0]$ direction. A close examination of the SADP shows the split of diffraction spots and extra diffraction spots, located halfway between the central (0 0 0) spot, the 0002 spots and $\{01\bar{1}0\}$ spots. However, no Morie' fringes were observed in the corresponding HRTEM in Fig. 5.3(c) so that double diffraction can be neglected in this study. Since the crystallographic phase of these ZNs belongs to wurtzite structure with a space group of $P6_3mc$, it easily appears as a characteristic "zigzag" structure [70,71], so-called "superlattice diffraction", corresponding to the observed extra spots in the SADP. It seems to imply that the crystal structure of the scattered ZNs was constituted from many tiny areas such as domains or mosaic texture according to the disoriented few degrees in SADP. It is well known that a crystal with mosaic structure does not have its atoms arranged on a perfectly regular lattice extending from one side of the crystal to the other; instead, the lattice is broken up into a number of tiny blocks, each slightly disoriented one from another. Within these tiny blocks, there exists a structural mismatch at the interface between these domains [72], as in this case with 1–21 difference in the SADP. Furthermore, the HRTEM image in Fig. 5.3(c) recorded from the scattered ZNs reveals that there seem to be two types of lattice fringes in this HRTEM image: one with wave-like fringes (as arrowed in Fig. 5.3(c)) and the other with straight fringes. This variation of lattice fringes as marked with arrows seems to be caused by these two types of crystal arrangements. Fig. 5.4(a) shows the TEM BF image of the aligned ZNs grown on ZnO/Si substrate. In contrast

to the scattered ZNs, most of the ZNs were grown along the direction perpendicular to the ZnO_f/Si substrate. A higher magnification in Fig. 5.4(b) indicates that the lattice fringes are perpendicular to the longitude direction of the ZNs, and the singular fringe spacing is about 0.51 nm, which is nearly consistent with the c-axis parameter in hexagonal ZnO structure (c=0.521nm in ZnO structure). This demonstrates that the [0 0 0 2] direction is the preferred growth direction for the well-aligned ZNs. In addition, as one pays attention to the interface between ZNs and ZnO_f/Si shown in Fig. 5.4(c), it was observed that the well-aligned ZNs seem to be nucleated from the cup tip near the grain boundary between two ZnO grains in ZnO film. The lattice image at the joint of the interface, shown in the inset of Fig. 5.4(c), clearly indicates that the lattice fringes near the interface of ZnO grains in ZnO film are continuous without any cracks. The formation of the cup shape around grain boundaries between two ZnO grains is supposed to be correlated with the solution reaction during the nucleation and growth of ZNs. This implies that the cup tip probably becomes a preferential nucleation position for the well-aligned ZNs grown on ZnO_f/Si. However, in addition to (0 0 0 2) fringes, some ZNs with white lines dissecting the ZNs can be identified as marked with arrows in Fig. 5.5 that is probably due to faster stacking and the instability of the polar (0 0 2) plane in ZnO. These kinds of planar defects are easily developed at a higher growth temperature, i.e. 90 °C, and can be considered as extrinsic stacking faults with insertion of an extra Zn-O layer parallel to the basal plane. It was worth noting that the presence of (0 0 0 1) stacking faults provides a possible diffusion path to modify its optoelectronic properties according to our study [73]. However, wellaligned ZnO nanorods without any planar defects can also be obtained in aqueous solution by controlling the experimental conditions.

5.4 Growth behavior of ZnO nanorods

It is well known that the growth behavior of ZNs was strongly influenced by growth

conditions such as ion concentration in the solutions, reaction temperature and time, which can be elucidated by the change of the aspect ratio ($AR = \text{length}/\text{width}$) of ZNs. As illustrated in Fig. 5.6, when the pure Si substrate was placed in the Zn-containing aqueous solution at 75 °C, it was found that in an initial growth stage of ZNs, prior to 0.2 h, no obvious ZNs can be detected. However, above that (0.2–0.3 h), SEM images (not shown here) show a small amount of ZNs with ~20 nm in diameter and ~60 nm in length that were randomly scattered on Si substrate. Although the SiO₂ is probably formed on the Si substrate, a similar growth phenomenon is also observed for SiO₂/Si substrate. This implies the importance of ZnO film coating on the nucleation and growth of aligned ZnO nanorods. Above 0.5 h, the aligned ZNs can be clearly obtained but the scattered ZNs start to preferentially grow along the longitude (c-axis) direction. With an increase of growth time, it can be observed that the growth of scattered ZNs becomes slower compared to that of the aligned ZNs. Especially above 5 h, it was found that the AR of the scattered ZNs changes little (9–11). Furthermore, with increasing growth time up to 15 h, the AR slightly decreases. This implies that the scattered ZNs do not further grow as expected despite extending growth time. As evidenced from the TEM BF image and corresponding SADP of ZNs shown in Fig. 5.7, it seems to reveal that more than two ZNs are self-assembled together to form a bundle in a coplanar manner using their side planes to form a large ZN as shown in Fig. 5.7(c) of the TEM dark-field (DF) image. This bundle of ZNs can be further transformed into another ZN with a larger dimension in diameter. In other words, the side crystal planes of the ZNs are able to glue together to form a larger crystal. This behavior is also called “oriented attachment” [74]. This observation may be used to explain the slight decrease in AR in the later growth stage (5–15 h). Consequently, the growth behavior of the scattered ZNs can be considered as a two-step growth mechanism. In contrast, as the ZnO_f/Si substrate was used and immersed into the precursor solution for the growth of ZNs, it was found that in the initial growth stage (to 0.5 h), no aligned ZNs can be clearly observed from the ZnO_f/Si substrates, but at 1 h, a smaller AR was obtained for the

aligned ZNs compared to that of scattered ZNs. This phenomenon reveals that the aligned ZNs need incubation time to nucleate from ZnO film (in a nucleation stage) but the scattered ZNs are under both stages of nucleation and growth. It was believed that the ZnO nuclei will be preferentially grown on the ZnO_f/Si substrate in this stage due to the high affinity of the nuclei of ZnO nanorods to the surface of ZnO film, especially at the cup sites as shown in Fig. 5.4(c). In this condition, although an inherent asymmetry along the c-axis allows the anisotropic growth of the crystal along the [0 0 0 2] direction, the lateral growth along different directions is possible for the nucleus to reduce the surface energy effect. When the favorable nucleation positions of ZNs were formed on the ZnO film, ZnO growth unit (or coordination polyhedron) will stack in order and grow along the [0 0 0 2] direction. Subsequently, a fast growth along the longitudinal direction (c-axis) for the aligned ZNs was expected because the growth in width direction is suppressed due to the size of the cup shape on ZnO_f/Si substrate. Finally well aligned and highly oriented ZNs with an aspect ratio up to 25–30 can be obtained in 15 h. These results can be used to explain the observation that the well-aligned ZNs with a smaller AR were developed in an early stage, but later, the ZNs were rapidly grown along the longitudinal direction.

5.5 Summary

Single-crystal ZnO nanorods (ZNs) can be synthesized on both Si and ZnO_f/Si substrates in an aqueous solution at 75 °C, but they present different growth behavior and direction. On pure Si substrate, ZNs were scattered over the entire Si substrate with a preferred orientation in the (1 0 0) plane or grown along the $[01\bar{1}0]$ direction. HRTEM observation demonstrates that the scattered ZNs present a two-stage growth mechanism with a self-assembly process of ZNs in the later growth stage. In contrast, on Si wafer with ZnO film coated, aligned ZNs

were directly grown along the $[0\ 0\ 0\ 2]$ direction from the ZnO film on Si. In comparison with the AR of the scattered ZNs, a larger AR up to 25–30 was obtained. This simple approach should promise us a future large scale synthesis of the patterned growth of the highly well-aligned ZNs on various kinds of substrates buffered with a controlled morphology and roughness layer in an aqueous solution at low temperatures.



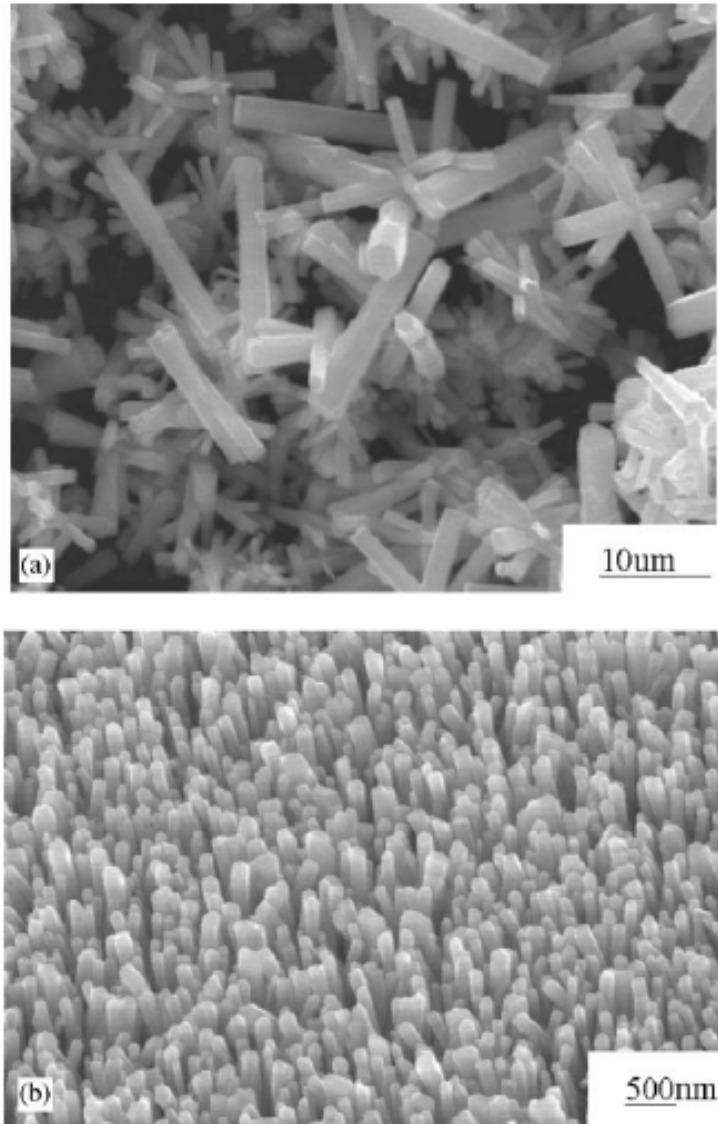


Fig. 5.1. SEM micrographs of ZnO nanorods grown on (a) Si and (b) ZnO_f/Si substrates.

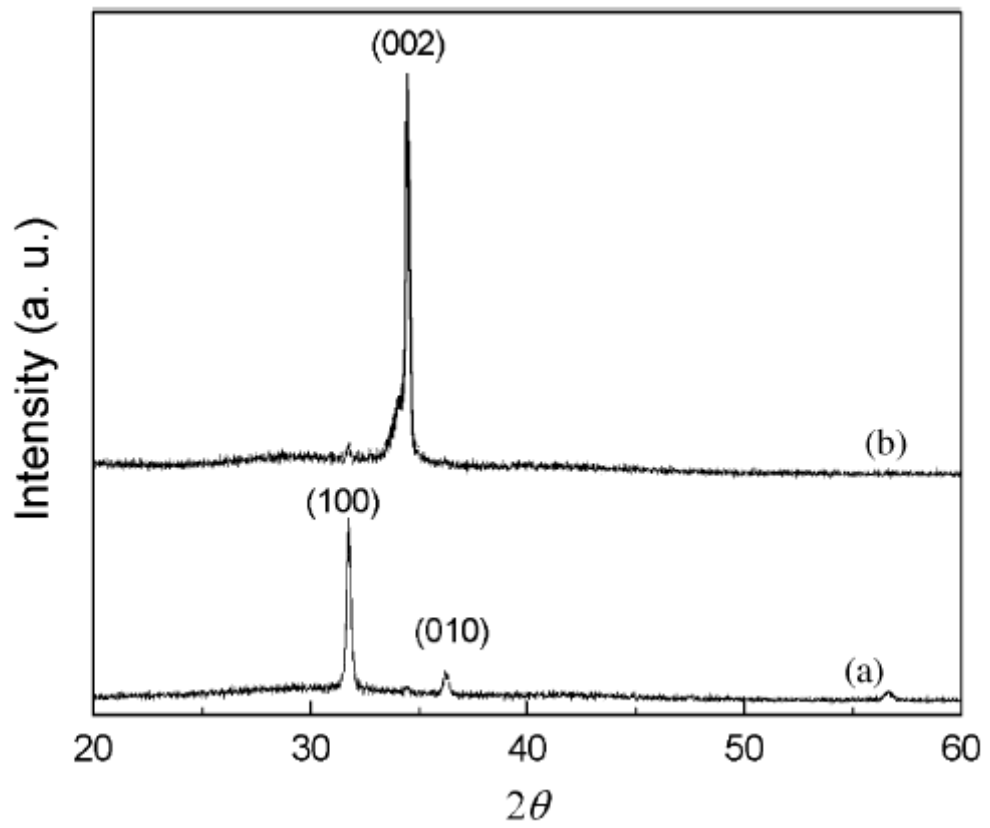


Fig. 5.2. X-ray diffraction patterns of ZnO nanorods grown on (a) Si and (b) ZnO_f/Si substrates.

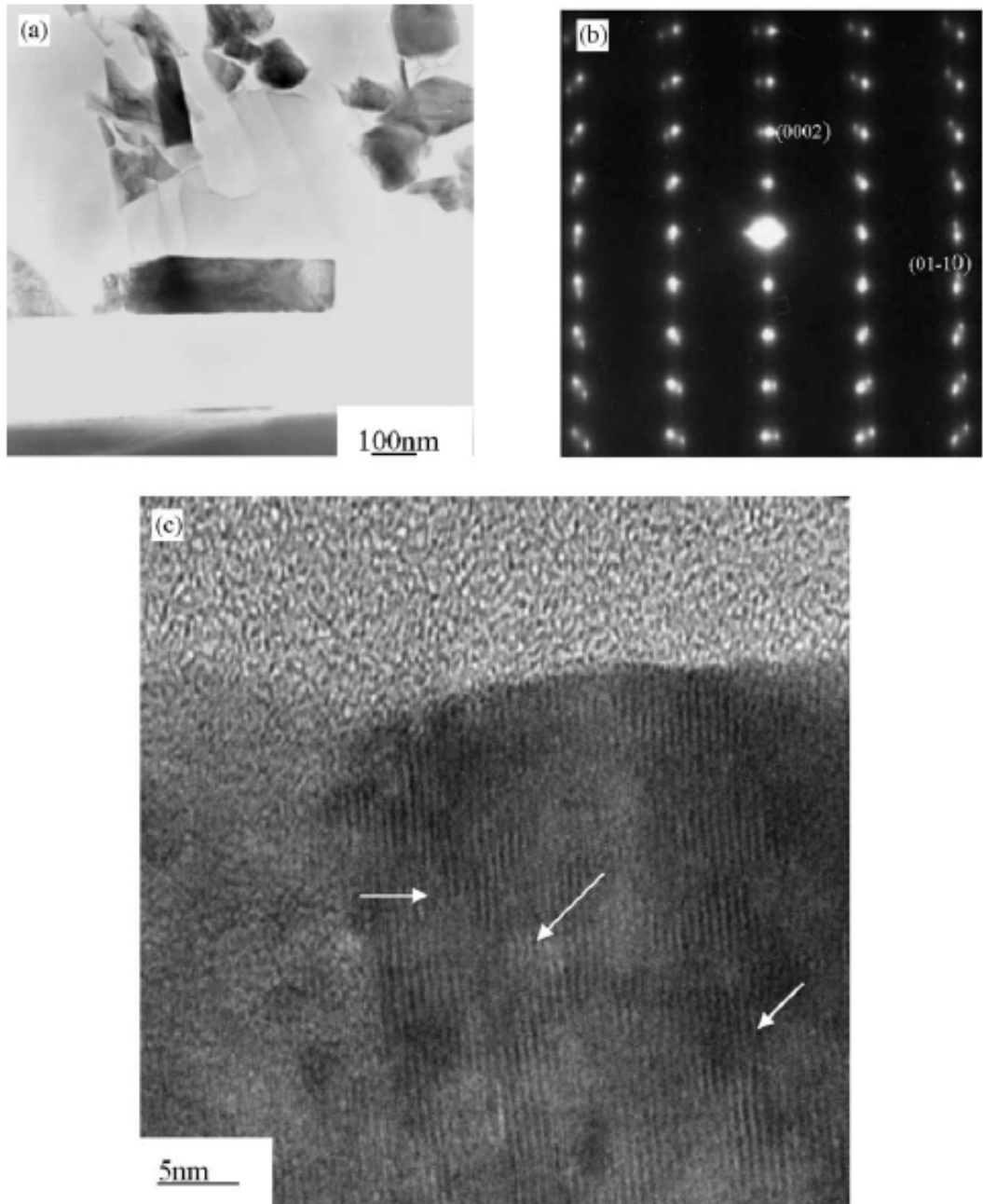


Fig. 5.3. (a) TEM bright-field (BF) image and (b) corresponding selected area diffraction pattern of ZnO nanorods grown on Si substrate. (c) Lattice fringes of ZnO nanorods in (a).

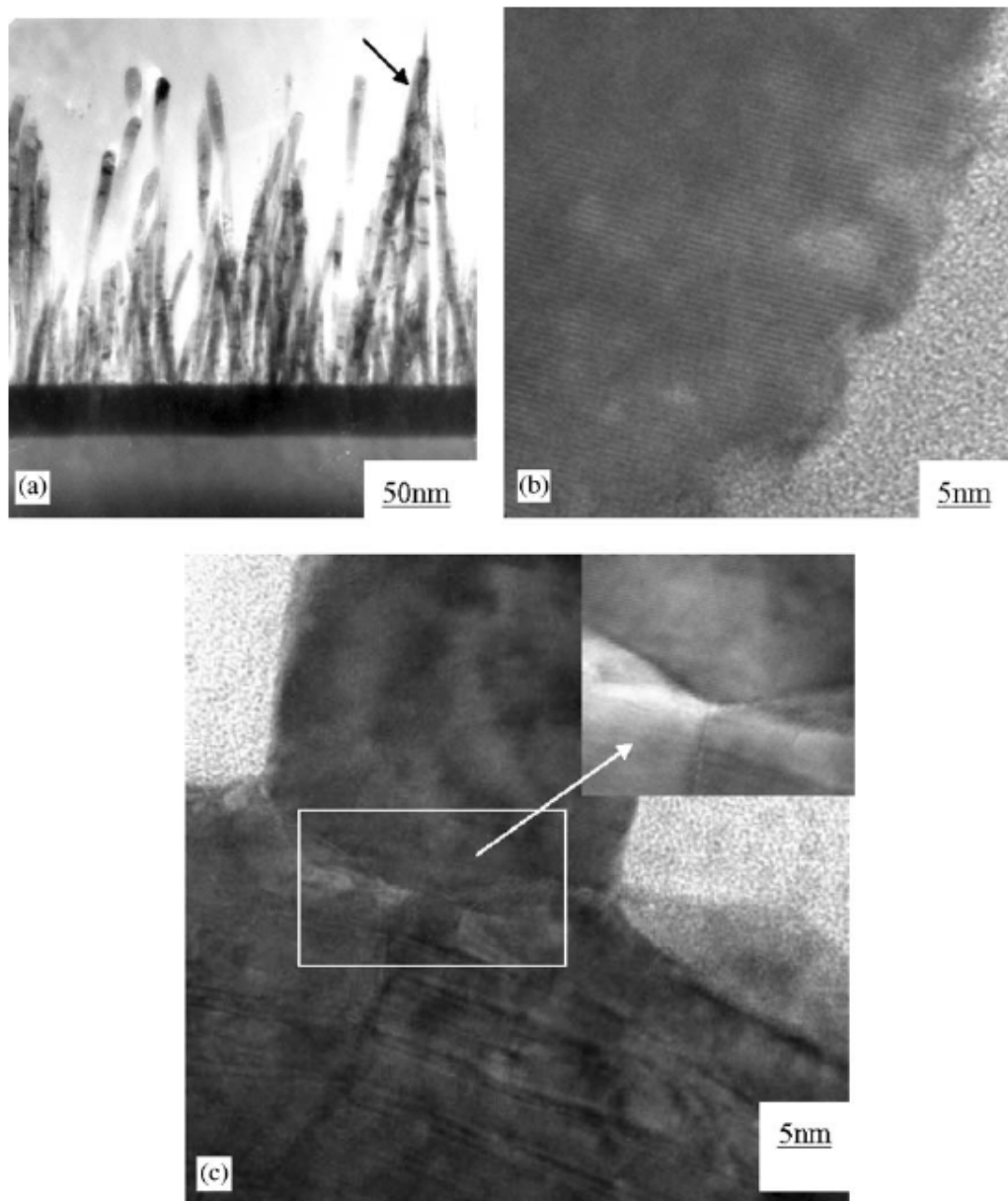


Fig. 5.4. (a)TEM BF image of aligned ZnO nanorods grown on ZnO_f/Si substrate. (b) High-resolution TEM images of the aligned ZNs and (c) interface region between ZNs and ZnO_f/Si.

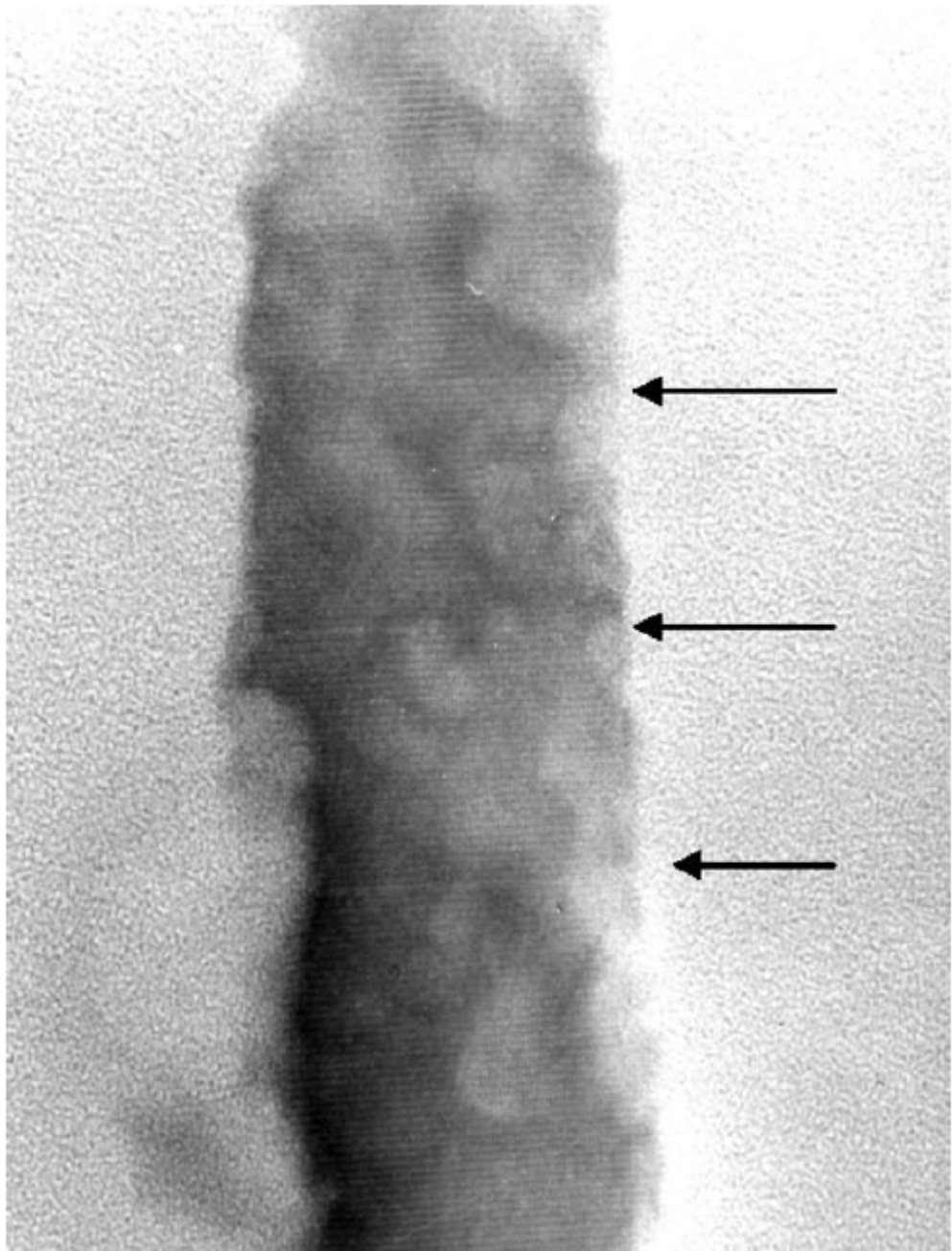


Fig. 5.5. High-resolution TEM (HRTEM) image of ZnO nanorods showing the presence of stacking faults (SFs) as marked with arrows.

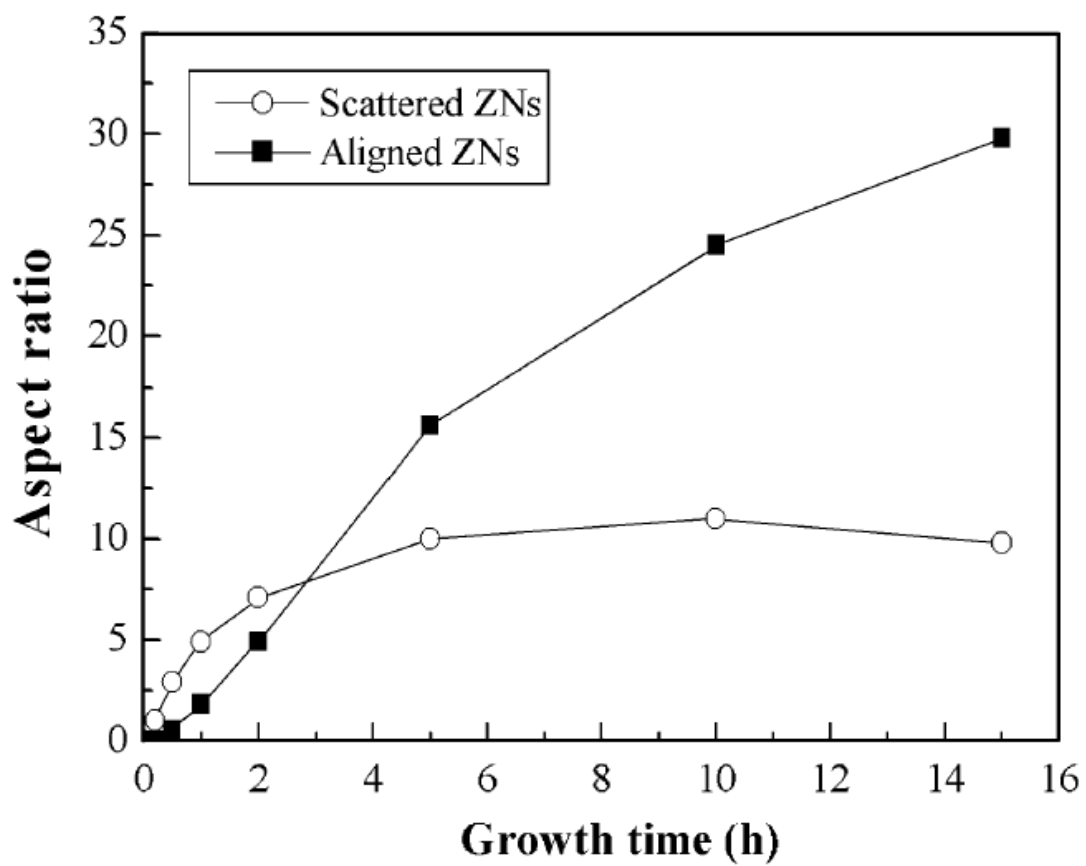


Fig. 5.6. Dependence of aspect ratio (AR) on growth time for scattered and aligned ZnO nanorods.

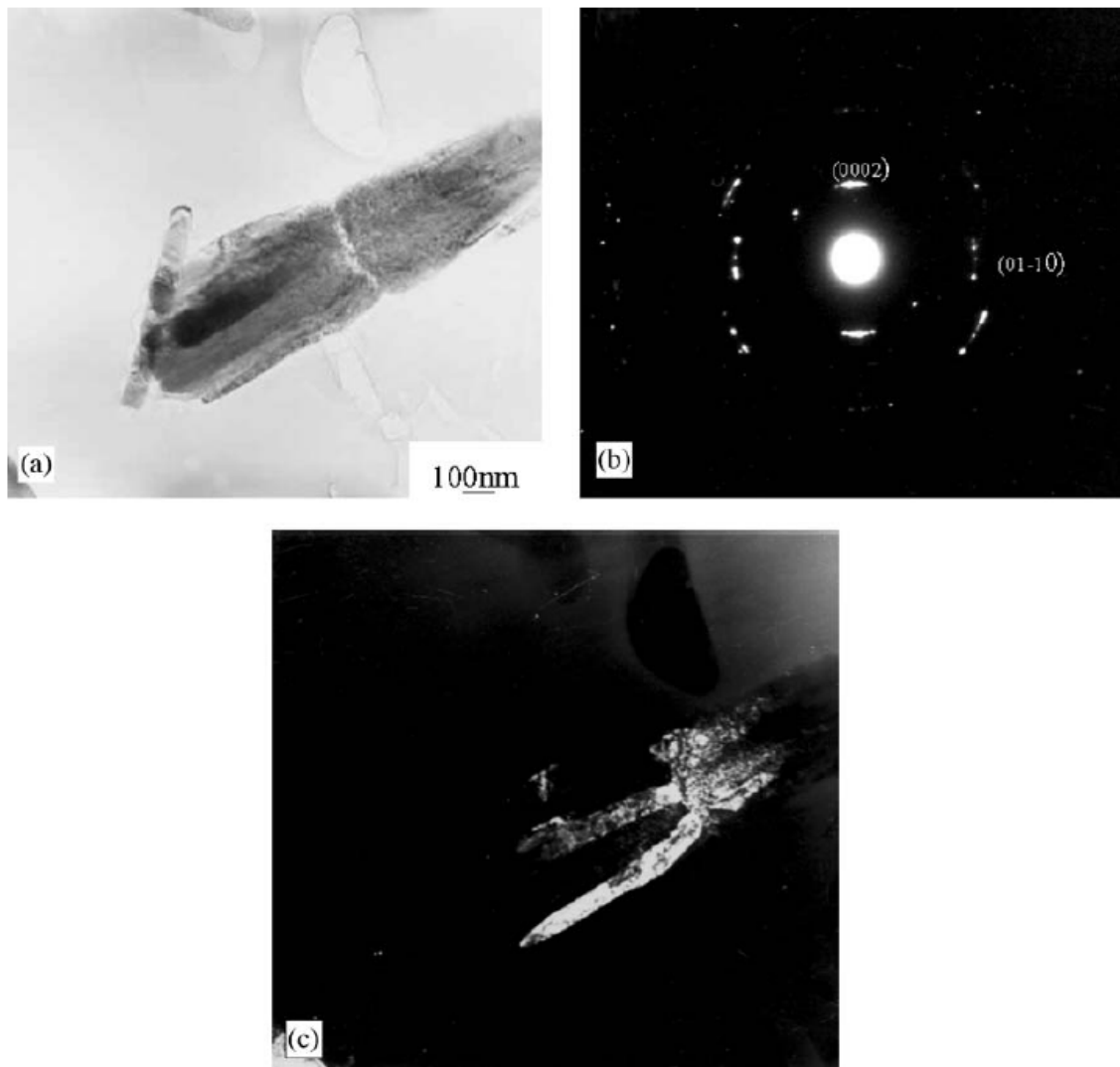


Fig. 5.7. (a) TEM bright-field image, (b) corresponding selected area diffraction pattern, and (c) dark-field image of self-assembled ZnO bundles.

Chapter 6

Synthesis and Luminescent Properties of Strong Blue Light-Emitting Al₂O₃/ZnO Nanocables

6.1 Introduction

Al₂O₃ has been used for capacitor dielectrics and gate oxides in memory devices due to its high dielectric constant, very low permeability and high thermal conductivity.[75] However, the photoluminescence property of alumina film or nanoparticles has not been studied in detail. Yoldas et al. studied alumina–silica powders and stated that the presence of pentahedrally coordinated aluminum appears to be strongly correlated to the occurrence of photoluminescence. [38] Suga et al. studied alumina gel from an inorganic salt and alkoxide and mentioned that the photoluminescence is closely related to oxygen defects and the development of Al^V site. [39] However, no data exists for determining the dependence of the properties of a defect centre on the structure of its coordinate sites and the presence of luminescence. Recently, Li et al. reported that a broad band located around 422 nm could be detected from nano-sized γ -Al₂O₃ powder. [40] It is suggested that the produced defect level could induce γ -Al₂O₃ nanopowder to emit blue photoluminescence (PL) bands. However, most of those studies have been focused on nanopowders or gel films. In past years, ZnO/Al₂O₃ core/shell nanofibers have been prepared from the Al₂O₃ deposition of ZnO nanowires with an atomic layer deposition technique, but no photoluminescence properties have been reported.[45] These findings indicate that so far, the photoluminescence property of nano-scale alumina film has been not investigated. In addition, our previous study found that

when an alumina film is deposited on a ZnO-coated silicon substrate by a wet chemical process, the alumina film not only emits blue, but the blue emission can also be much enhanced compared to that of coatings on pure silicon. This indicates that ZnO plays an important role on the photoluminescence properties of nano-sized alumina films.

Wet chemical approaches are widely used for the fabrication of large oriented arrays of ZnO nanorods on Si or polymer organic substrates. ZnO has been recognized as one of the promising nanomaterials in optoelectronic device applications. Therefore, it is possible to develop the Al₂O₃/ZnO nanostructure into white phosphor if blue emission from alumina can be incorporated into the ZnO nano-structure. So far, to the best of our knowledge, there have been no further systematic investigations on the light-emitting properties of alumina-coated ZnO nanorods grown in aqueous solutions at lower temperatures. Furthermore, it has been challenging to develop Al₂O₃/ZnO or ZnO-based nanostructures with strong light emission by simple wet chemical processing. Therefore, a simple method of combining the aqueous solution process with a thermal treatment is proposed to develop Al₂O₃/ZnO nanocables with strong blue emission. The structure and optical properties of the nanocables will be also discussed. In addition, the application of this advanced structure to modify luminescent properties demonstrates a new way to develop nanostructures for optoelectronic applications.

6.2 The structure of the Al₂O₃/ZnO nanocables

Figure 6.1(a) showed scanning electron microscopy (SEM) images of arrayed ZnO nanorods grown vertically on the substrate. As the ZnO nanorods were immersed in the Al⁺³ peptized solution with pH = 5-6, it was found that the ZnO nanorods were collapsed and transformed into nanoparticles as shown in Fig. 6.1(b). However, as the pH value of the solution was adjusted between 6.0 and 7.0, Fig. 6.1(c) shows that the nanorods remained unchanged and highly oriented. This result suggests that the microstructure of original ZnO

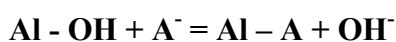
nanorods was strongly affected by the pH values of the Al^{+3} -peptized solution.

To understand how the microstructure of the as-grown ZnO nanorods was affected by the Al^{+3} peptized solution, X-ray diffractometry (XRD) and Fourier Transform Infrared Spectroscopy (FTIR) of the samples were analyzed. Figure 6.2 shows the XRD spectra of the ZnO nanorods grown in various pH solutions. It was observed that the ZnO phase disappeared at pH=4-6 Al^{+3} -peptized solution. This may be attributed to the fact that the ZnO nanorods were easily etched by nitric acid. However, as the ZnO nanorods were immersed in the Al^{+3} -peptized solution in the range of pH= 6.0-9.0, A single strong ZnO (002) peak at $2\theta = 34.4^\circ$ was detected, indicating that the crystalline phase of ZnO nanorods were remarkably influenced by the peptized solution.

As mentioned above, the pH value in the peptized solution plays a key role in the morphology and phase development of the ZnO nanorods. Fourier Transform Infrared Spectroscopy (FTIR) was further used to analyze the peptized solution. As shown in Fig. 6.3, the bands at 1390 cm^{-1} were attributed to the NO_3^- ions and the bands at 1042 cm^{-1} were assigned to the NH_3 wagging modes. The bands between 600 and 800 cm^{-1} may be contributed from the alumina complex. For a peptized solution in an acidic condition (pH value below 6.0), a strong NO_3^- band was observed, indicating the formation of NH_4NO_3 compound. Therefore, when the ZnO nanorods were immersed in the solution, it would be etched under this circumstance. In addition, a peak of alumina complex was observed in the FTIR curve ranging between 600 and 800 cm^{-1} . A ligand-exchange reaction between the surface site Al-OH and the dissociated form (A^-) of humic acid could take place. [76]



However, at a solution with pH = 6-9, the ligand-exchange reaction as shown below would become dominant.



Therefore, no any obvious peak in the range of $600\text{-}800\text{ cm}^{-1}$ was identified from the FTIR

curve. This may reveal that it is possible for the interaction between Al-peptized solution and ZnO nanorods in this condition.

6.3 Annealing effect on the Al₂O₃/ZnO nanocables

As evidenced from high-resolution TEM (HRTEM) in Fig. 6.4, heterostructured core(ZnO)-shell(Al compound) nanorod were observed. Figure 6.4 clearly reveals that the diameter of the core (ZnO nanorods) and the shell(AlOx) thin layer is about 20 nm and 7 nm, respectively. The {0002} lattice fringe of the ZnO nanorod core was parallel to the basal plane but no any lattice fringe can be identified in shell-AlOx thin layer, indicating that the shell layer was amorphous. The EDS analysis in mark-1 region presents a strong ZnO signal and no Al element. In contrast, in mark-2 region, the ZnO signal becomes weak but Al element becomes a little strong compared to those of mark-1. The TEM result suggests that the ZnO nanorods are not damaged and the AlOx layer on ZnO nanorods has been formed.

The High-Resolution (HR) TEM image in Figure 6.5(a) illustrates that alumina was conformably deposited on the ZnO nanorods to become a core/shell Al₂O₃/ZnO nanocable structure. From the selected area electron diffraction (SAED) in the inset of Fig. 6.5(a), two diffraction patterns (rings and spot patterns) are observed. The spot pattern is from the single-crystal ZnO structure, while the ring pattern can be attributed to an amorphous alumina structure that may be a pseudo-boehmite phase developed in aqueous solution according to the report of Ishizaka.[41] Upon annealing at 200°C, a short-range ordered structure seems to develop in the alumina shell as shown in the HRTEM image of Fig. 6.5(b). It is believed that rapid thermal treatment in O₂ atmosphere is favorable for the cleavage of the oxygen-hydrogen bond (OH), causing the departure of H ions from the pseudo-boehmite and initiating the occurrence of phase transformation of amorphous pseudo-boehmite into a γ -phase alumina structure. This structure can be thought of as a cubic spinel, with some

suggestion of a tetragonal (tetrahedrally coordinated aluminum) distortion in boehmite-derived γ - Al_2O_3 in the $I4_1/amd$ space group.[77] When annealed at 400°C in an O_2 atmosphere, a long-range ordered structure can be clearly observed from the HRTEM image in Fig. 6.5(c). According to the calculation of the lattice fringe (about 0.2 nm), it was indexed as (400) plane, indicating a γ -phase alumina structure ($d=0.198$ nm). This suggests that with increasing temperature to 400°C in an O_2 atmosphere, the γ -phase was developed in the alumina shell. As annealed at 600°C , two kinds of lattice fringes are clearly observed for annealed $\text{Al}_2\text{O}_3/\text{ZnO}$ nanocables as shown in Figure 6.5(d), indicating that in addition to single crystalline ZnO nanorods, a crystalline γ -alumina structure has been completely formed in the alumina shell at 600°C .

6.4 The investigation of photoluminescence centers in the $\text{Al}_2\text{O}_3/\text{ZnO}$ nanocables

Figure 6.6(a) shows the room-temperature photoluminescence (PL) property of $\text{Al}_2\text{O}_3/\text{ZnO}$ nanocables at different temperatures. Three important emission peaks can be observed from the PL spectrum of as-synthesized alumina-coated ZnO nanocables. Both UV emission (378 nm) and green-yellow (visible) emission (525-575 nm) bands are attributed to ZnO nanorods, and the other broad blue emission (425-475 nm) is possibly from the alumina shell. The near band edge (UV emission) is generally attributed to free exciton recombination, but the green-yellow emission is produced from the oxygen defect of the pure ZnO nanorods fabricated by chemical solution methods. In fact, it was found that the UV emission intensity of the as-grown nanocables increases with annealing temperature at 200 - 600°C in oxygen ambient, but the visible emission in post-annealed samples tends to disappear, suggesting that the native defects can be reduced by post-annealing treatment as shown in Fig. 6.6(a). It was noted that when the $\text{Al}_2\text{O}_3/\text{ZnO}$ nanocables are annealed at 200°C in O_2 atmosphere, an obvious blue emission at around 450 nm can be clearly identified that was primarily

contributed from the alumina shell. According to the report of Lipprns et al.[78], an increase of annealing temperature may cause the cleavage of the oxygen-hydrogen bond (OH) in pseudo-boehmite structure, and consequently, both Al-O-O^\bullet and Al-O^\bullet defects would probably be produced in the alumina shell and vary with annealing temperature and atmospheres. At a lower temperature, i.e., 200°C , Al-O-O^\bullet defects are much easily generated than Al-O^\bullet . However, According Ishizaka's report, the distance between the aluminum atom and the electron spin in Al-O-O^\bullet is long enough to neglect the hyperfine interaction with Al, indicating that Al-O-O^\bullet would not be a luminescent center.[79] With the increase of annealing temperature, the OH band in pseudo-boehmite structure tends to be broken and Al-O^\bullet would be formed during the phase transformation from pseudo-boehmite phase (octahedrally coordinated structure) to γ -phase aluminum oxide (tetrahedrally coordinated structure), favoring pentahedrally coordinated aluminum and the occurrence of singly ionized oxygen vacancies which are regarded to the F^+ center.[80]

With increasing temperature to 400°C , dehydration proceeds and the structure evolves through a series of disordered states during the phase transformation from pseudo-boehmite to γ -phase as demonstrated in Fig. 6.5(c). In this condition, pentahedrally coordinated aluminum is easily formed, indicating that more singly ionized oxygen vacancies (F^+ center) defects can be generated. Therefore, a strong blue emission can be observed. At a higher temperature, i.e., 600°C , although the positions of the blue emission remain unchanged, it is found that the peak intensity is weakened compared to the sample annealed at 400°C . This indicates that the defect density of the main defects (F^+ centers) responsible for blue emission is decreased with increasing annealing temperature up to 600°C . Consequently, the density of F^+ centers is reduced due to compensation in O_2 atmosphere.

As reported in the literature, ZnO material usually generates strong UV emission.[81] However, it can be seen in the figure that UV emission decreases while blue light emission increases. It can be inferred that UV emission from the ZnO band edge recombination can

excite the blue light of aluminum oxide. This may result in different intensity ratios of blue light to UV in the PL spectra. To further investigate the effect of heat-treatment on the F^+ centers and pentahedrally coordinated aluminum, the as-synthesized Al_2O_3/ZnO nanocables samples were subjected to annealing at different temperatures in N_2 and O_2 atmospheres. The relative PL ratios (I_B/I_{UV}) of blue emission to UV emission on annealing temperature as a function of O_2 and N_2 atmospheres is presented in Fig. 6.6(b). It is observed that the strongest blue emission of the nanocables appears at $600^\circ C$ in nitrogen ambient instead of $400^\circ C$ in oxygen atmosphere. Furthermore, it should be noted that the blue emission of post-annealed Al_2O_3/ZnO nanocables is dominated not only by the annealing temperature but also the annealing atmosphere because the PL emission is very sensitive to defect type.[82] As dehydration proceeds, the structure evolves through a series of disordered states, probably from octahedral to pentahedral and then tetrahedral. Ishizaka et al. reported that the luminescence is maximized for alumina treated at $600^\circ C$, at which temperature γ -alumina is formed.¹³ Yoldas et al. studied calcium aluminate glass and suggested that the pentahedrally coordinated aluminum (Al^V) may be strongly correlated with the occurrence of luminescence. Therefore, ^{27}Al NMR analysis was performed to characterize such complexes.[41] Figure 6.7 shows the ^{27}Al MAS NMR spectra of these samples as a function of annealing temperature. Besides the resonance lines attributable to tetrahedrally (Al^{IV}) and octahedrally (Al^{VI}) coordinated aluminum, a line corresponding to pentahedrally (Al^V) coordinated aluminum has also been observed. It was found that the concentration of pentahedrally coordinated (Al^V) aluminum are dependent on the thermochemical environment within the samples. Furthermore, the Al^V signal increases with firing temperature, reaches a maximum intensity at about $600^\circ C$, and then decreases at a higher temperature in both O_2 and N_2 annealing atmospheres. When comparing Fig. 6.6(b) with Fig. 6.7, it was noted that although the concentration of pentahedrally coordinated aluminum is higher at $600^\circ C$, the relative peak intensity (I_B/I_{UV}) of the O_2 -annealed nanocables is decreased. This may imply that with the

increase of annealing temperature, the OH band in pseudo-boehmite structure tends to be broken and produce more pentahedrally coordinated aluminum and singly ionized oxygen vacancies (F^+). However, the F^+ centers would be compensated in the case of annealing in oxygen at a higher annealing temperature, i.e., 600°C. Therefore, in this condition, F^+ centers decrease, but the pentahedrally coordinated aluminum still exists as indicated from the NMR result.

Because the equilibrium structure during the transformation of boehmite to γ -alumina phase is determined by the number of the OH groups,[83] the surface composition of Al_2O_3/ZnO nanocables was further examined by x-ray photoelectron spectroscopy (XPS) for samples annealed at 400°C in N_2 and O_2 atmospheres as shown in Figure 6.8. XPS spectra of Al 2p in annealed Al_2O_3/ZnO nanocables are shown in Fig. 6.8(a). The peak position for the samples with nearly stoichiometric composition annealed in N_2 atmosphere is located at a binding energy of 74.3 eV, indicating that the Al–O binding state is dominated by the boehmite/ γ -alumina phase. In contrast, the Al 2p position of the samples annealed in O_2 atmosphere is located at a binding energy of 74.6 eV, indicating that γ -alumina is easily formed for the sample treated in O_2 gas. The asymmetric spectrum of O 1s in Fig. 6.8(b) and 5(c) contains three peaks at 529.6 eV, 530.8eV and (broadly) 532.6 eV. The peaks around 529.6 eV and 530.8 eV can be assigned to O^{2-} ions in the Zn–O bonds and Al-O bonds, respectively. The peak related to the highest binding energy around 532.6eV is attributed to OH bonds. As a result, a strong OH-bond peak was observed in N_2 atmosphere compared to that in O_2 atmosphere. This again demonstrates that more F^+ centers are produced by the rapid thermal treatment of 400°C in O_2 atmosphere resulting in stronger blue emission.

However, with a further increase of annealing temperature up to 600°C, it was found that the I_B/I_{UV} decreases in O_2 atmosphere but increases in N_2 atmosphere. The F^+ centers would be diminished due to compensation in O_2 atmosphere. In contrast, I_B/I_{UV} continuously increases and reaches the maximum intensity at 600°C in N_2 atmosphere. Therefore, the

relative I_B/I_{UV} intensity of the Al_2O_3/ZnO nanocables annealed in N_2 atmosphere is stronger than that in O_2 atmosphere at $600^\circ C$, indicating the difficulty of compensating F^+ centers in a nitrogen ambient. Therefore, in this work, it can be concluded that the blue emission is primarily dominated by F^+ centers that are accompanied by the occurrence of pentahedrally coordinated aluminum during the phase evolution of the Al_2O_3 shell on the ZnO nanorods.

6.5 Summary

In summary, we have developed well-aligned arrays of Al_2O_3/ZnO nanocables on ZnO/Si substrate substrates buffered with a ZnO film by combining a simple chemical solution with a low-temperature treatment. The photoluminescence measurement indicates that a strong blue emission peak at ~ 450 nm appears at $400^\circ C$ and $600^\circ C$ in O_2 and N_2 atmospheres, respectively. The phenomenon is strongly related to OH bond cleavage and a phase transition from amorphous to γ -phase alumina, as evidenced by XPS and NMR analyses. To the best of our knowledge, the results provide an effective method for constructing nanostructures with strong blue light emission.

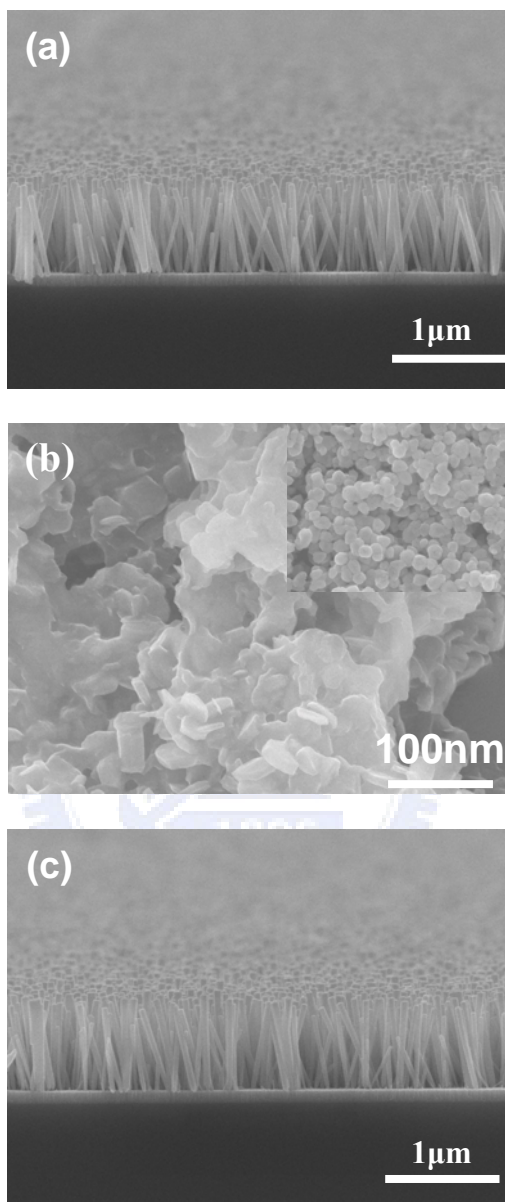


Fig. 6.1 SEM images of (a) the as-grown ZnO nanorods and those immersed in the peptized solution at pH = (b) 4.0~5.0 and (c) 6.0~7.0.

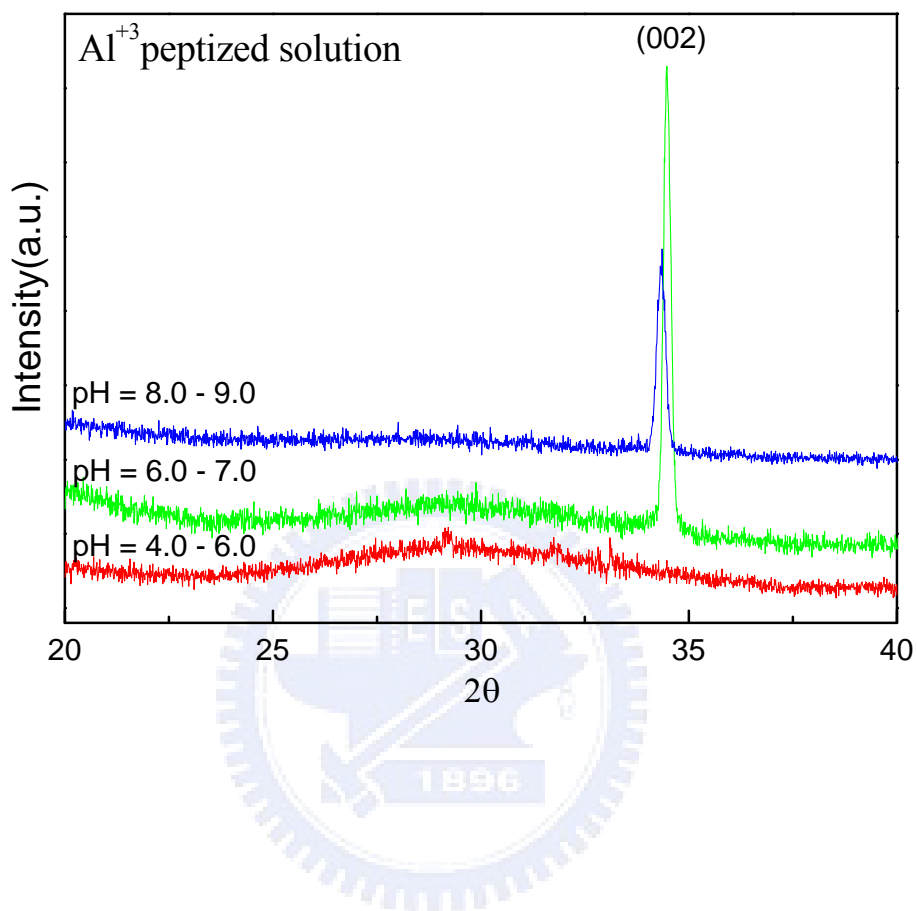


Fig. 6.2 X-ray diffraction patterns of ZnO nanorods immersed in the various pH-value solutions.

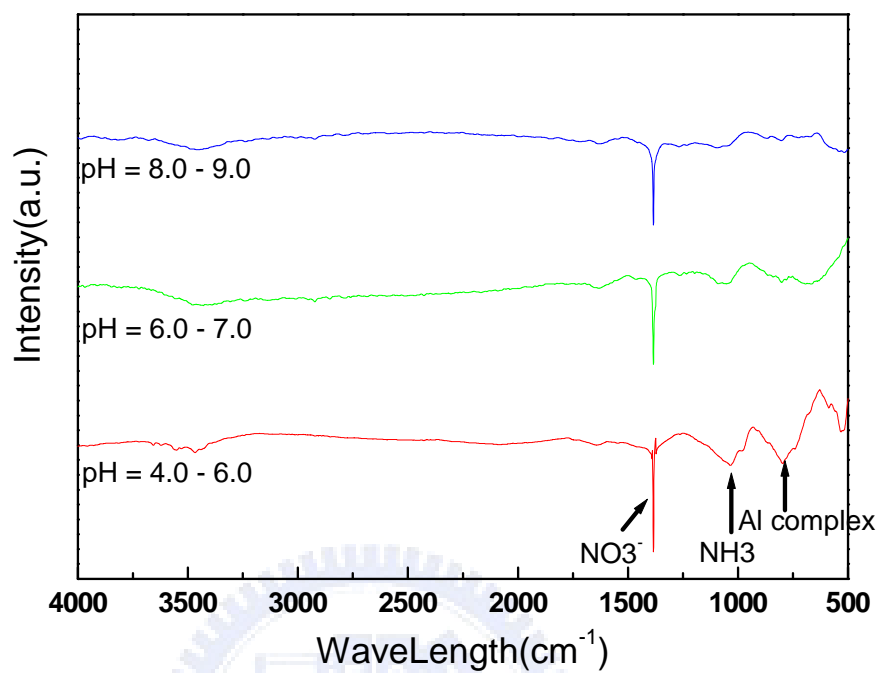


Fig. 6.3 Fourier Transform Infrared Spectroscopy (FTIR) of the Al^{3+} peptized solution as a function of pH.

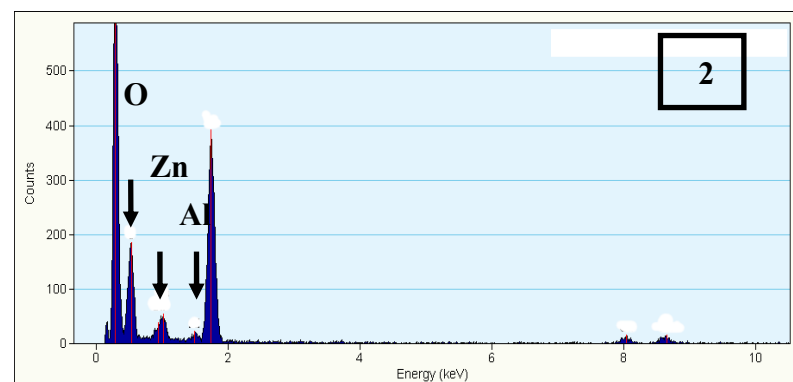
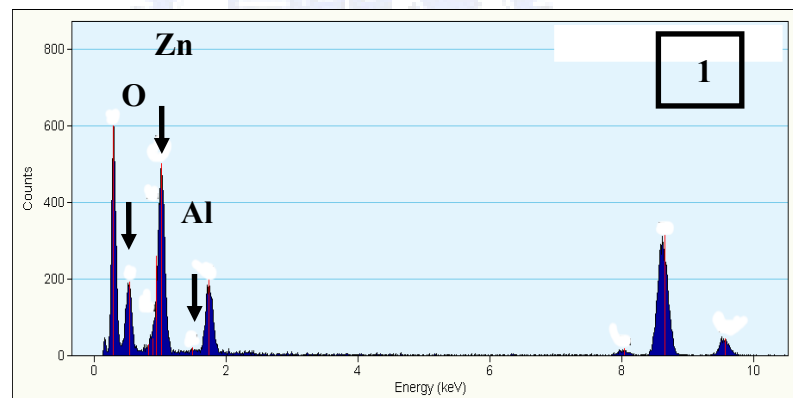
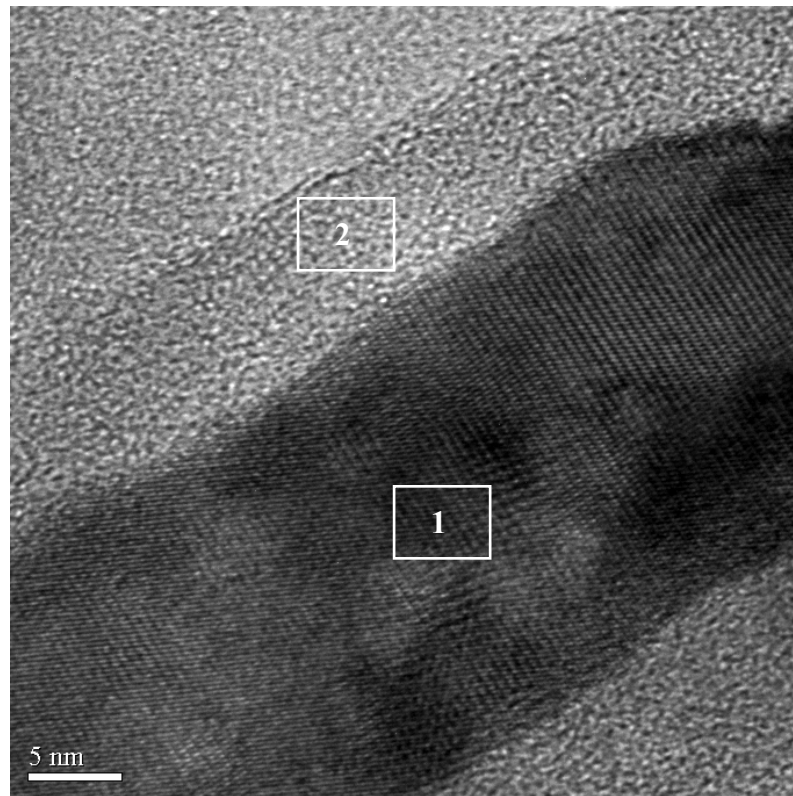


Fig. 6.4 High-resolution TEM (HRTEM) image of AlO_x-ZnO core-shell structure and its EDS analysis.

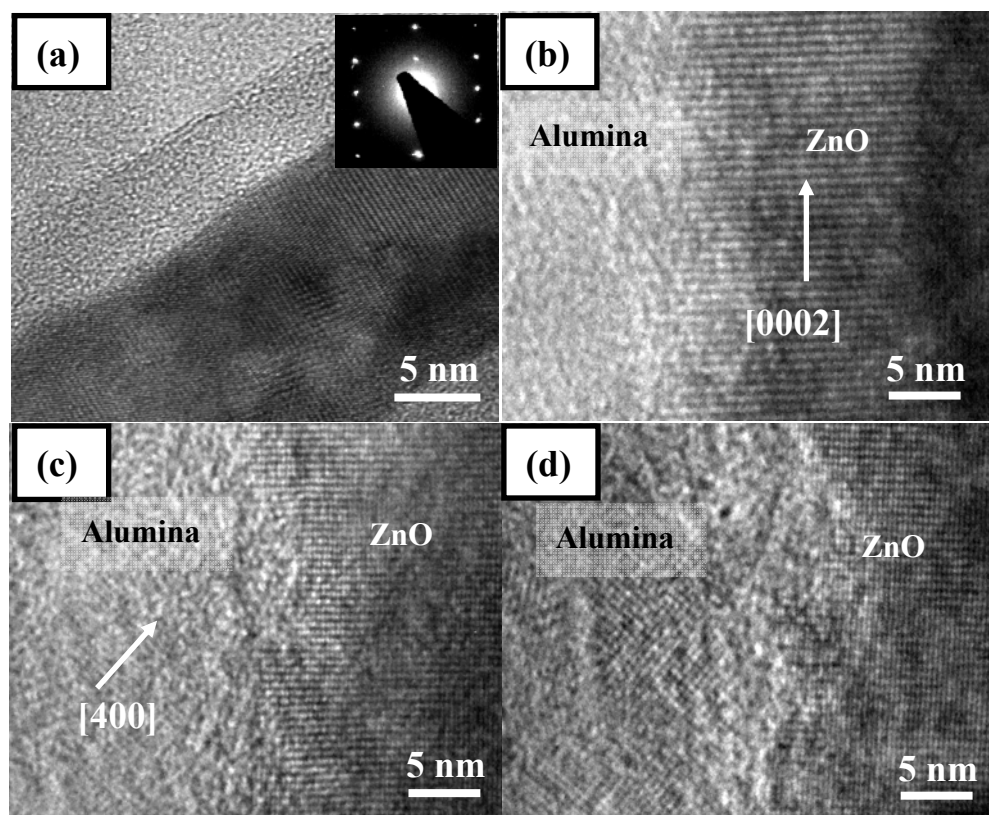


Fig. 6.5 High-resolution TEM of Al₂O₃/ZnO nanocables (a) as-synthesized; and annealed at (b) 200°C; (c) 400°C and (d) 600°C in oxygen ambient.

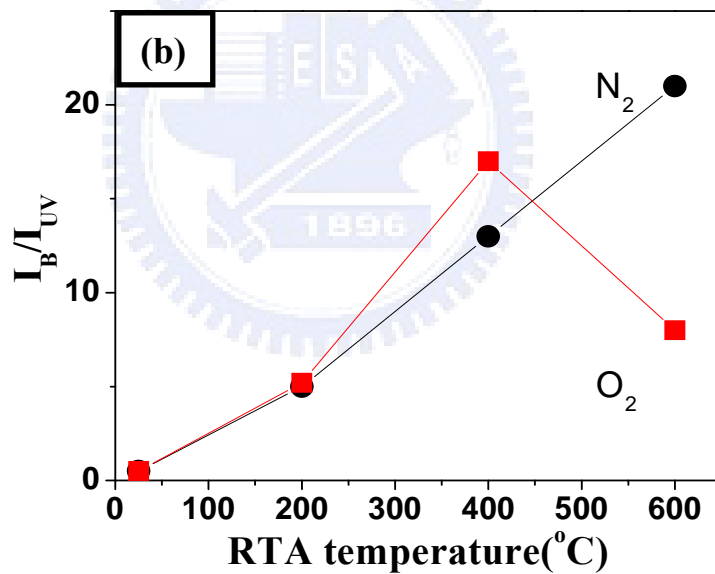
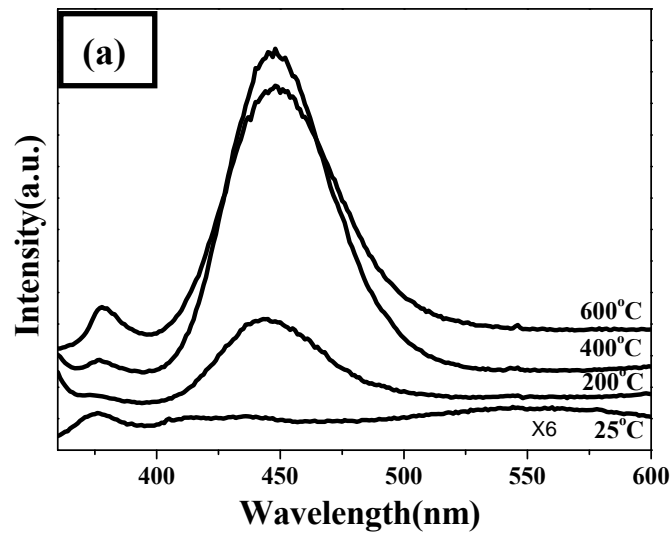


Fig. 6.6 (a) Room-temperature PL spectra of $\text{Al}_2\text{O}_3/\text{ZnO}$ nanocables after rapid thermal anneal at various temperatures in O_2 atmosphere. (b) The relative PL ratios (I_B/I_{UV}) of blue emission to UV emission on annealing temperature as a function of O_2 and N_2 atmospheres.

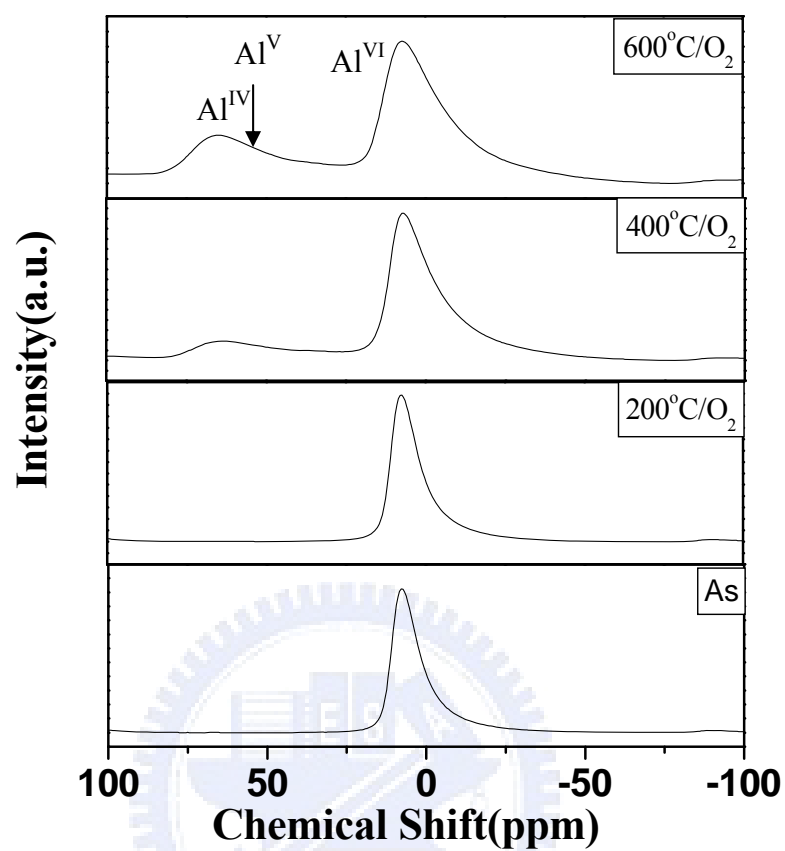


Fig. 6.7 ^{27}Al MAS NMR spectra for the alumina-coated ZnO nanorods annealed in O_2 .

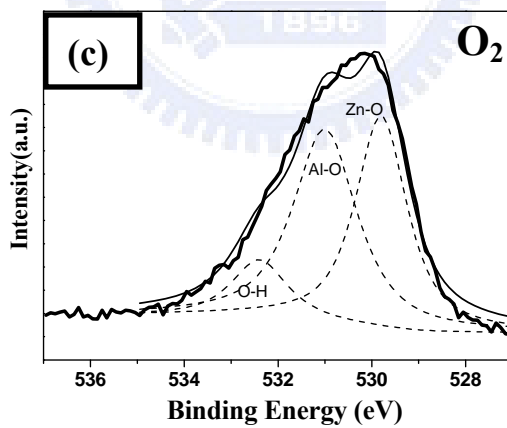
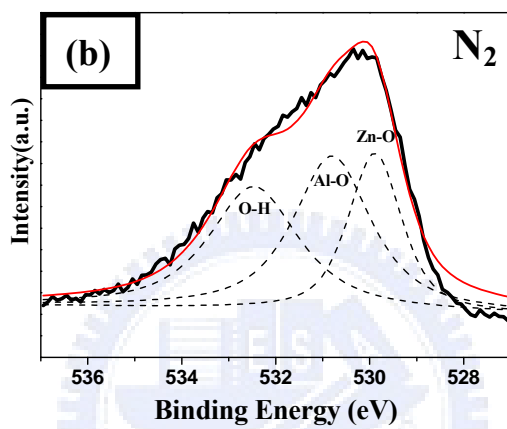
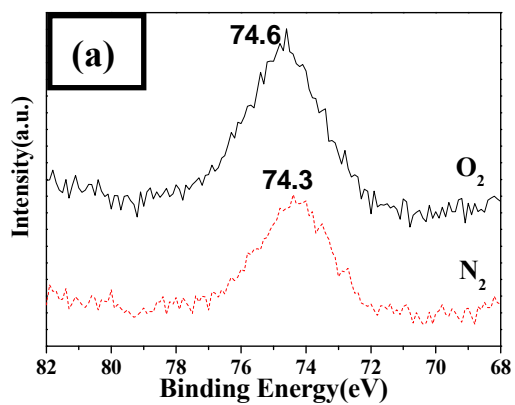


Fig. 6.8 XPS spectra for the Al_2O_3/ZnO nanocables of (a) Al 2p and O 1s annealed in (b) N_2 (c) O_2 at $400^\circ C$.

Chapter 7

Synthesis and Optical Properties of White-light Emitting Alumina/ZnO Nanotubes

7.1 Introduction

Zinc oxides (ZnO) have attracted extensive attention for nanoscale electronic and optoelectronic device applications because of their wide band gap and large excitation binding energy (60 meV). Numerous ZnO nanostructures have been demonstrated, including nanowires, nanotubes, and nanobelts. It is believed that tubular structures exhibit higher porosity and larger surface area than bulk materials, creating enhanced performance and activity.[84] Recently, ZnO nanotubes have been fabricated by many methods, such as a hydrothermal process, a template-assisted method and a thermal oxidation process. Almost all reports of ZnO nanotubes focus on morphologies, synthetic methods, and growth mechanisms. As mentioned above, however, the increased surface area is a key feature of tubular ZnO. Inevitably, high surface areas will significantly modify the chemical and physical properties of materials, which can be reflected in photoluminescence (PL) spectra.

Liu et al. studied the optical properties of faceted hexagonal ZnO nanotubes (ZTs) and reported that a strong yellow emission was detected after annealing at 400°C in ambient oxygen.[85] In contrast, Sun et al. reported that after annealing at 400 °C for 2h under vacuum, the PL spectrum of ZTs showed an increase in UV emission intensity and a concomitant decrease in green–yellow emission. Zhang et al. recently mentioned that a strong green emission was obtained from ZnO nanotubes annealed in H₂. Considering the large surface area-to-volume ratio in nanostructures, large numbers of defects and impurities at the

surface of ZnO nanotubes can produce new states that act as visible luminescence centers and broaden the visible emission band. This suggests that the ZnO nanostructure could, after low-temperature growth and high-temperature annealing treatments, be developed for application in photoluminescent devices. In our previous study, we found that when an alumina film was deposited on ZnO nanorods and then annealed at 600°C in the nitrogen ambient, the alumina-coated ZnO nanorods displayed a strong blue light emission. (The relative intensity (blue/UV) of the samples is up to 20. This indicated that ZnO strongly effected the photoluminescent properties of nano-sized alumina films, leading to different UV to blue light intensity ratios in the PL spectra. Furthermore, depending on the processing methods, a variety of defects can be easily generated in nano-structured ZnO. Therefore, it is possible to develop white light-emitting alumina coated ZnO nanotubes if relative intensities of various color emission can be properly controlled by incorporating alumina into the ZnO nano-structure to modify the defects in ZnO nanotubes. To the best of our knowledge, there have been no other systematic investigations of the light-emitting properties of alumina-coated ZnO nanotubes synthesized at low temperatures.

In this work, we propose a simple method of combining the chemical process with thermal treatment to develop alumina-coated ZTs. In addition, we discuss the structure and photoluminescent properties of the alumina-coated ZTs. It has been demonstrated that the color of emitted light can be varied with annealing processes at different temperatures and under different atmospheric conditions. White light-emitting alumina-coated ZTs may be useful in novel nanoscale electric and optoelectronic devices.

7.2 Synthesis and physical properties of ZnO nanotubes

Figure 7.1(a) shows the ZnO nanorods grown along c-axis on the ZnO_f/Si substrate in 0.01M at 95°C for 5 hours with diameter 100-300 nm. However, it was observed that when

the growth time increased to 4 days, ZnO nanotubes were formed with the diameter 100- 400 nm as shown in the Fig. 7.1(b). It can be inferred that the c-axis plane disappeared during a long-time growth. Similarly, Fig. 7.2(a) shows the SEM image of some small nanorods grown at 95°C for 12 hours in 0.001M. When the growth time increased to 24 hours, it was noted that, the ultra-thin ZnO nanotubes (ZTs) can be obtained with diameter 20-30 nm (Fig. 7.2(b)). Therefore, it was believed that the formation of the ZTs is strongly related to the increased growth time. To investigate growth mechanism of the ZTs, we measured the various pH value v.s. different growth time in three growth concentration, 0.1M, 0.01M and 0.001M (Fig. 7.3(a)). When the solution concentration is 0.1M, the pH value of solution is decreased with growth time increasing. And then, when the concentration is 0.01M, the pH value almost keeps 6 with time increasing. Finally, when the concentration is 0.001M, the pH value is increased with growth time increasing, especially after 12 hours. The better condition to synthesize the ZTs is 0.001M, 95°C, 24-36 hours. In this pH range an amine in the HMT will be rapidly protonated to form the $(\text{CH}_2)_6\text{N}_4\text{-H}^+$ complex. With prolonged heating, a closed aqueous HMT solution continues to consume protons, ultimately going to a liquid-vapor equilibrium in which the solution will contain partially decomposed HMT complexes and ammonia (NH_3) with the vapor containing a mixture of H_2O , NH_3 , and CH_2O . Therefore, the pH value of the solution is increased with ammonia concentration increasing.

On the other hand, the XRD analysis (Fig. 7.3(b)) shows the crystal structure of the ZTs. The intensity of the (002) plane can be seen strong in the 0.002M at 12 hours, which the ZnO structure would be nanorods at this condition. However, when the solution concentration is 0.001M and the growth time is increased, the intensity of the (002) plane can be obtained weaker, indicating that the (002) plane is getting disappeared.

High-resolution transmission electron microscopy (Fig. 7.4(a)) shows that the ZTs are open-headed tubular structures with wall thicknesses of about 5~7 nm and inner diameters of about 15~20 nm. Fig. 7.4(b) shows the highly preferential growth of ZnO nanotubes along the

c-axis orientation (0002) with a lattice constant of ~ 0.52 nm. Compared to ZnO nanowires, the disappearance of the *c*-axis plane of the ZnO nanotubes was clearly observed. In addition, rough inner surfaces were observed. Sun and co-workers reported that, during the formation of ZnO nanotubes in the solution, the concentration of all zinc-containing species falls and the concentration of OH⁻ increases with increasing *t*, leading to a progressive reduction in the overall Zinc/OH⁻ ratio. At first, the solution supersaturation falls below that required for growth. It may even fall to the point of triggering dissolution, as suggested by the appearance of volcano-like surface structures that serve as templates for the emerging NTs. With increasing time, the *c*-axis plane dissolves into Zn(OH)₂, forming the nanotube structure. Here, a rough inner surface was developed during the disappearance of the *c*-axis plane.

7.3 The structure of the ZnO nanotubes after thermal annealing

The ZTs were annealed in O₂ from 200°C to 600°C. At 200°C, no obvious changes were observed in the SEM and TEM images. Fig. 7.5(a) shows that ZTs annealed at 400°C in ambient oxygen had a diameter of 30 nm. After annealing at 400°C in oxygen ambient, surface roughness increased on the outside surface, probably due to the thermal etching seen in the TEM images in Fig. 7.5(a). Therefore, under these conditions, the diameter and wall thickness of the ZTs were possibly altered, and many surface defects were produced on the outside surface. The disappearance of the *c*-axis plane led to the formation of the nanotube structure, creating a rough inner wall at the initial stages. However, the inner surface morphology became flattened, as shown in Figure 7.5(b). When the ZTs were thermally annealed, the atoms may possibly have obtained enough energy to rearrange into their native morphology. To reduce the surface energy, the side plane wanted to flatten, but it was heavily thermally etched. It is believed that this is why the diameter of the ZTs decreased with increasing annealing temperature. When the annealing temperature increased to 600°C,

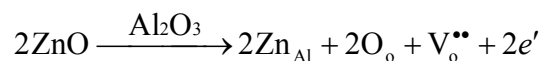
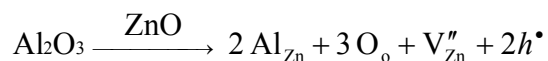
low-magnification TEM of the ZTs indicated that the inner wall became very rough (Fig. 7.5(c)). Further investigation by high-resolution TEM analysis (Fig. 7.5(d)) demonstrated that the inner wall became wave-like in shape. The lattice fringe of the ZT was different (marked with two arrows), indicating that the wave shape was probably related to structure relaxation during the high temperature treatment.

Figure 7.6 shows the room-temperature photoluminescence (PL) of ZTs annealed at different temperatures in oxygen ambient. Two obvious emission bands were observed: UV emission related to free exciton recombination at around 378 nm and broadband visible emission related to the oxygen defects. When the ZTs were annealed at 400°C in oxygen, the outside surface was gradually thermally etched and became very rough, indicating that more surface defects were created. Under these conditions, the oxygen gas was easily absorbed on the ZT surface, producing more oxygen interstitials (O_i). This was especially true for hollow ZTs, which have a much higher surface/volume ratio than ZnO nanowires. Wu et al. reported that oxygen interstitials may be the source of yellow emission.[86] Therefore, the yellow emission strengthened due to the increase of the oxygen defects and the UV emission intensified because increased annealing temperature decreased structural defects.

Increasing annealing temperatures to 600°C thermally etched both the outside and the inside surfaces of ZTs. The wave-like surface was confirmed by HRTEM analysis (Fig. 7.5(b)), indicating an increased surface-to-volume ratio with very high temperature treatments. Therefore, the crystallinity of ZTs decreased as the UV emission decreased in PL spectra. When the samples were annealed at high temperatures, antisite oxide O_{Zn} formed from interstitial oxygen O_i and zinc vacancies V_{Zn} in O-rich conditions.[87,88] Therefore, the broadband visible emission resulted from O_i , V_{Zn} and O_{Zn} defects. It has been reported that at 800°C antisite oxide forms, becoming the predominant source of point defects. In addition, the number of V_{Zn} defects increases. In our experiments, strong emission at 512 nm from O_{Zn} and V_{Zn} was observed.

7.4 The structure of the alumina/ZnO nanotubes

Figure 7.7(a) shows an SEM image of ZnO nanotubes coated with a nanoparticle alumina shell by the solution process. The low magnification TEM in Fig. 7.7(b) proves that the ZTs were covered with a number of alumina nanoparticles. The diameters of the ZTs were about 40 nm. The corresponding high-magnification TEM image in Fig. 7.7(c) clearly shows that the alumina nanoparticles were crystalline and distributed well on the ZTs. EDX line-scanning analysis further confirmed that alumina had successfully coated the surface of the ZTs (Fig. 7.7(d)). When the temperature was increased to 400°C, the alumina nanoparticles were clearly observed on the surface of the ZTs (Fig. 7.8(a)) but it was predicted that a phase transformation would occur in the alumina nanoparticles. The as-deposited alumina pseudo-boehmite phase would transform into γ -alumina according to literature report.[18] However, it was observed that some interaction occurred on the surface of ANZTs. It was noted in the HRTEM image in Fig. 7.8(b) that lattice disorder appeared at the interface of ZnO/Al₂O₃. The generated defects (V_{Zn} , V_O) strongly influenced the optical properties and will be discussed later. Upon raising the temperature to 600°C, as shown in Fig. 7.9(a), an interaction layer formed between the outside alumina layer and the surface of ZnO nanotubes. In addition, according to the Kirkendall effect, Zn atoms diffused into the alumina layer and several voids were formed in the core of the tubes, as shown with arrows in Fig. 7.9(b). The reaction would be expressed by the following equations.[89]



The corresponding diffraction pattern clearly revealed that the ANZT structure consisted of ZnO nanotubes grown with (002) planes and poly-crystalline γ -phase alumina. Fig. 7.9(a) also

shows lattice distortion and a local interaction at the ZnO/Al₂O₃ interface because of nanoscale effects. The lattice fringe changed from 5.2 Å inside the ZnO (002) to about 4.6 Å at the interface of ZnO/Al₂O₃. This may be related to the formation of a spinel structure reported in the literature. [46]

7.5 The optical properties of the alumina/ZnO nanotubes

To observe emission at 600-700 nm, a 400 nm optical pass was used, resulting in the appearance of 410 nm emission. Fig. 7.10 shows the PL spectra of the ANZTs under different annealing conditions. As annealed in oxygen ambient, it was found that the PL spectra of the ANZTs exhibit a very broad peak from 425 nm to 750 nm as shown in Fig. 7.10(a). Furthermore, it was also observed that the PL spectra are also changed with annealing atmosphere. As seen in Fig. 7.10(b), ANZTs annealed in nitrogen at different temperatures displayed one strong blue and one weak green-yellow peak. The broad green-yellow peak dominated at low annealing temperatures (below 600°C), and a strong blue emission peak at ~450 nm occurred at 600°C. The blue emission was primarily due to singly ionized oxygen vacancies in alumina. Large numbers of oxygen vacancies in the ANZT alumina nanoparticle shell were produced by annealing in nitrogen at high temperature. The above-mentioned results indicated that the PL spectra of the alumina-coated ZnO nanotubes (ANZTs) could emit different colors by varying the annealing conditions. Fig. 7.10(c) illustrates this with blue, green and white emissions.

The PL spectra of the ANZTs annealed in oxygen at different temperatures were further analyzed by Gaussian curve fitting as shown in Fig. 7.11. The curve fitting of the PL spectra revealed the competition between the UV, blue, blue-green, green and yellow band emissions associated with various defects. The fit using four peaks schema can be used to compare the relative intensity of the PL emission at the different spectral bands and only for this purpose.

Such fit cannot describe the spectrum as a whole. When the samples were annealed at 200°C in oxygen, the yellow emission dominated due to OH bond absorption on the surface of ANZTs. Increasing the annealing temperature to 400°C increased the blue emission and decreased the yellow emission. The blue emission was probably related to phase transformation from the boehmite phase (octahedrally coordinated) to the γ -phase (tetrahedrally coordinated), which starts to appear at this temperature. During phase transform, pentahedrally coordinated aluminum was produced, and singly ionized oxygen vacancies at the F^+ centers were responsible for the blue emission. For a detailed discussion, refer to our previous study. In general, the oxygen affinity in alumina is stronger than that in ZnO. Hence, the oxygen interstitials in the ZnO core diffused into the alumina shell, reducing the number of oxygen interstitials in ZnO. The number of oxygen vacancies in the ZT core nanotubes increased, leading to a strong green emission. In addition, as shown in Fig. 7.8, an interaction occurred at the interface between the ZnO nanotube and the alumina layer. As the Zn atoms compounded with Al, the concentration of Zn atoms in the nanotubes decreased, and the concentration of V_{Zn} increased. Since the emission of V_{Zn} is located at ~496 nm, this created blue-green light. As a result, the relative intensity ratio of the four color peaks (blue : blue-green : green : yellow) was estimated to be 1.3 : 1.7 : 1.2 : 1 for the ANZTs annealed at 400°C in oxygen.

Annealing ANZTs at a higher temperature (600°C) compensated for the F^+ centers and reduced the blue emission. According to the report by Yang et al., spinel structure might have been formed above 600°C.[90] The HRTEM image marked with an arrow in Fig. 7.9(d) shows that an intercompound structure, possibly a spinel structure, composed of Zn and Al appeared in the interface between the ZnO nanotubes and the alumina layer. This made the blue-green emission peak strong. In addition, annealing increased the number of ZT surface defects and thus strengthened the yellow emission. At the same time, the green emission was also enhanced because the interaction on the interface induced a large number of oxygen

vacancies in ZnO. Therefore, the relative intensity ratio of the four color peaks (blue: blue-green: green: yellow) changed to 0.86 : 1.23 : 1.11 :1, leading to white emission.

7.6 Summary

In summary, we have developed alumina nanoparticles-coated ZnO nanotubes (ANZTs) on ZnO/Si substrates buffered with a ZnO film by combining simple chemical solution growth and annealing. The ANZTs emitted different light emissions as the annealing temperatures and atmospheres were changed. A white-light emission, consisting of blue, blue-green, green and yellow band emissions, was obtained. Photoluminescence measurements indicated a blue emission peak at ~450 nm, a blue-green emission at ~496 nm, a green emission peak at ~525 nm and a yellow emission peak at ~600nm. This work not only demonstrates a novel method for preparing white-light emission alumina-coated ZnO nanotubes, but also suggests that the defect structure and transition mechanisms of samples could be modified by different defect species.

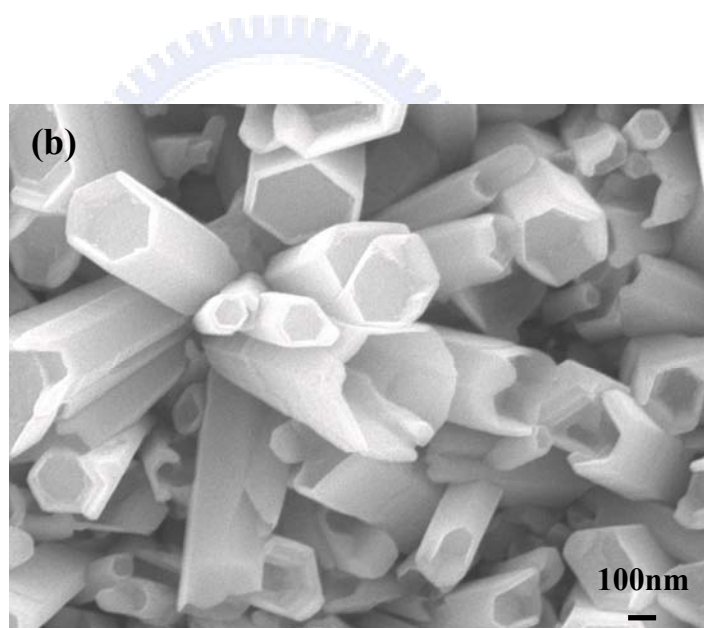
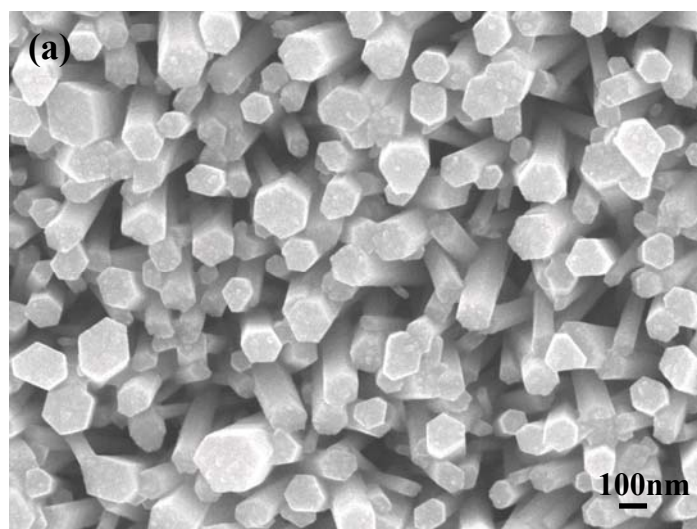


Fig. 7.1 SEM image of the (a) ZnO nanorods synthesized for 5 hours (b) ZnO nanotubes synthesized for 4 days.

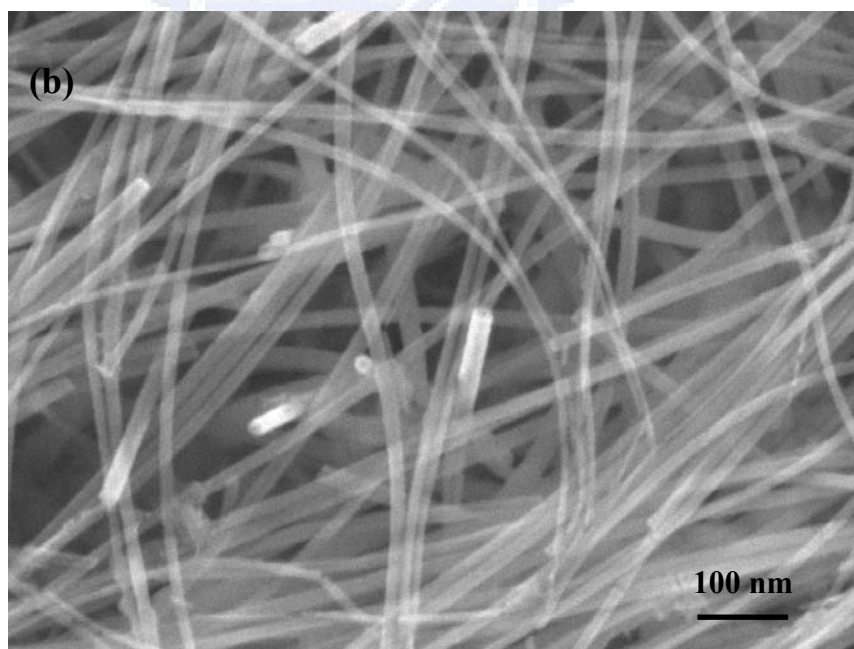
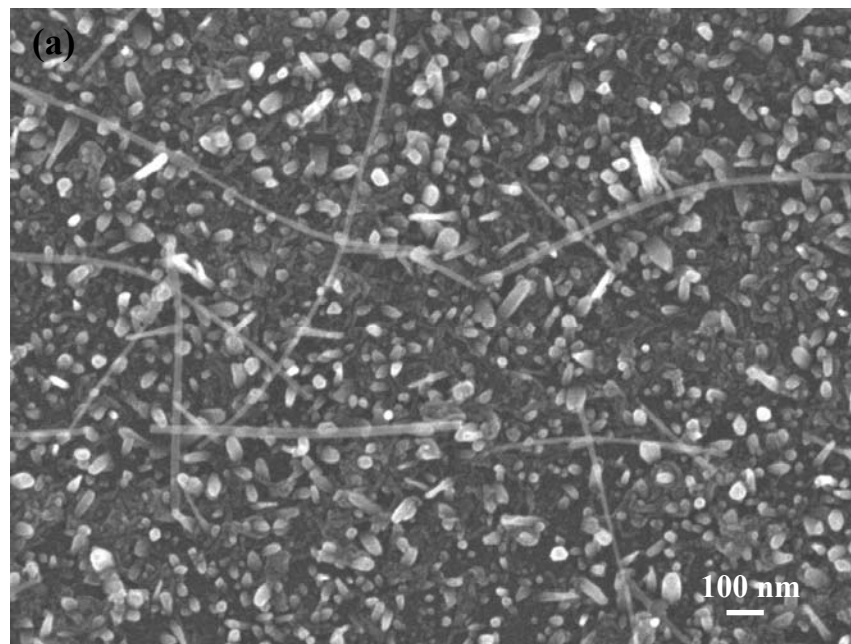


Fig. 7.2 SEM image of the (a) ZnO nanorods synthesized for 12 hours (b) ZnO nanotubes synthesized for 24 hours.

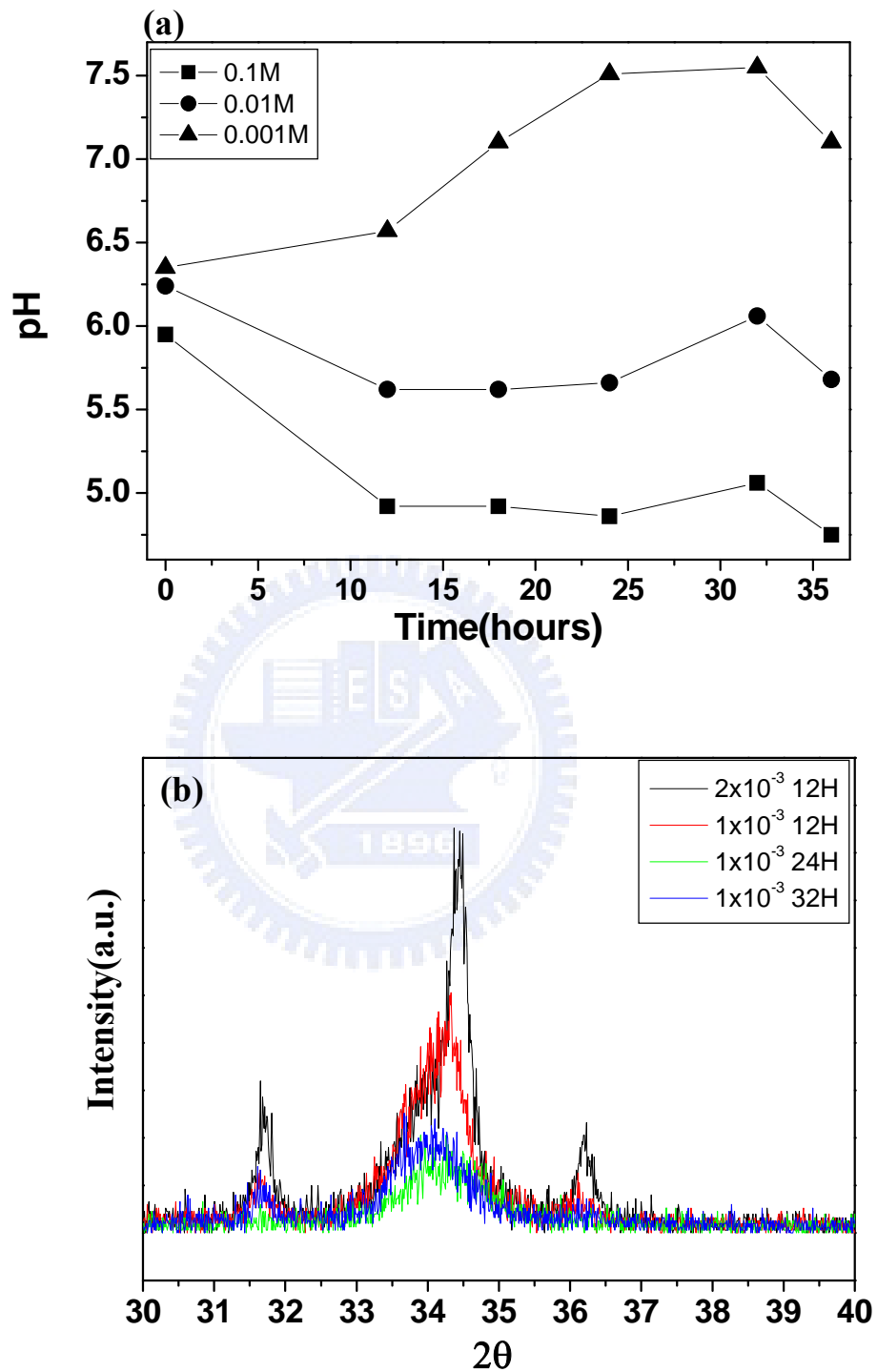


Fig. 7.3 (a) pH value varying with growth time as a function of solution concentrations. (b) XRD analysis of the ZnO nanotubes for different growth time.

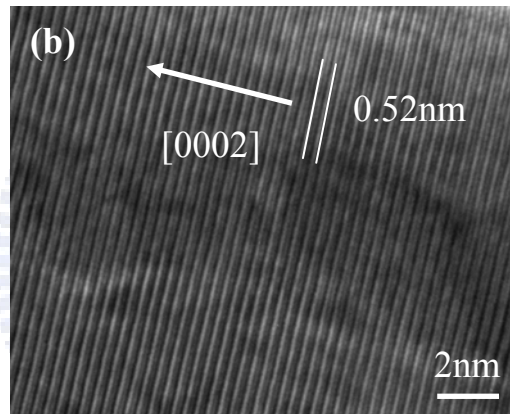
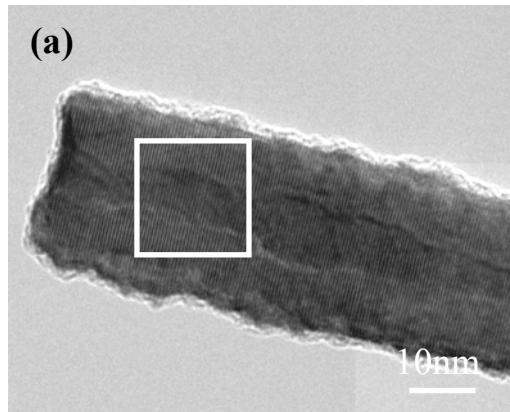


Fig. 7.4 (a) TEM images of a single ZnO nanotube. (b) High- resolution TEM image of a single ZnO nanotube.

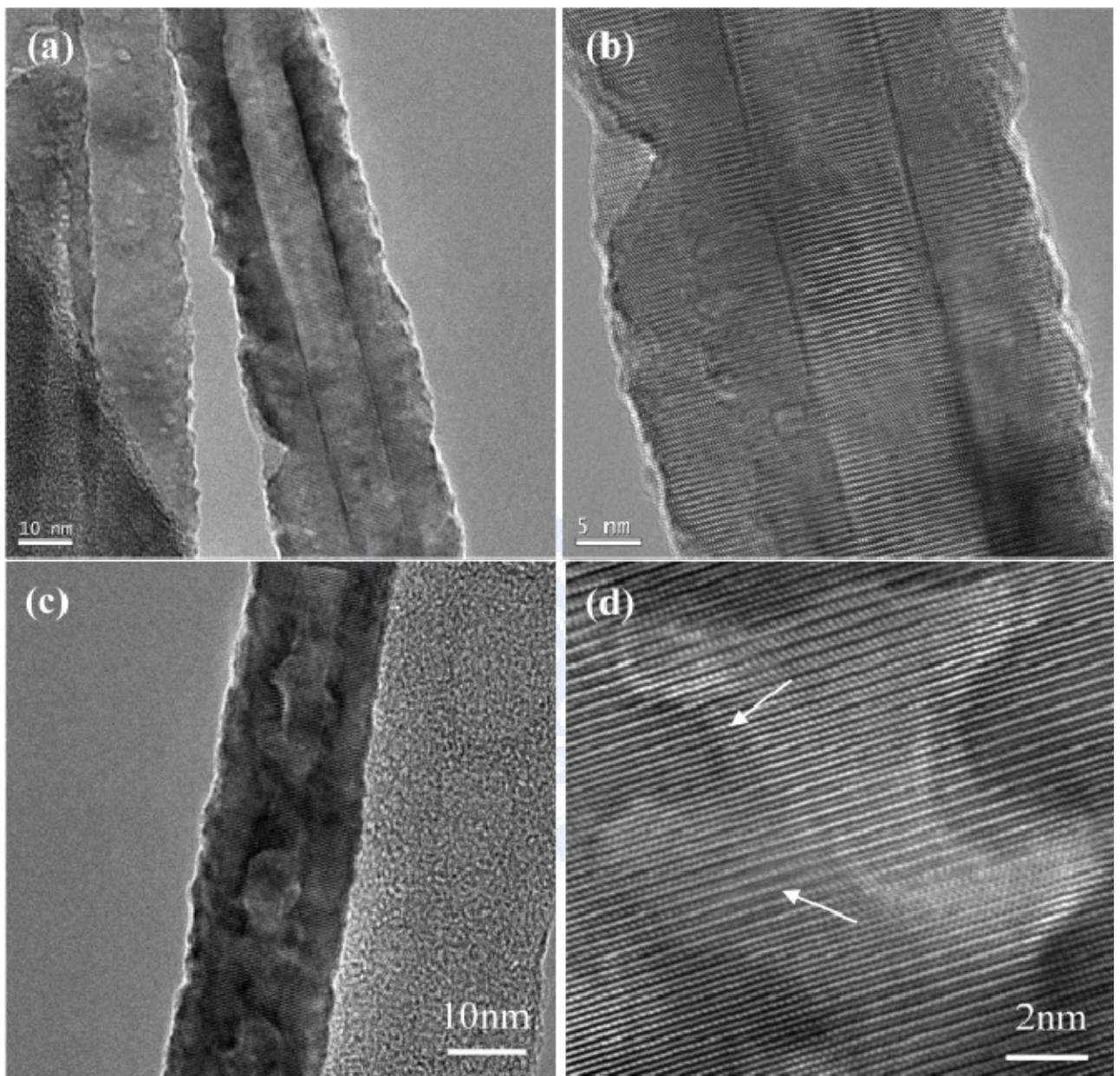


Fig. 7.5 TEM image of ZnO nanotubes annealed in oxygen at 400°C at (a) low magnification and (b) high magnification and at 600°C at (c) low magnification and (d) high magnification.

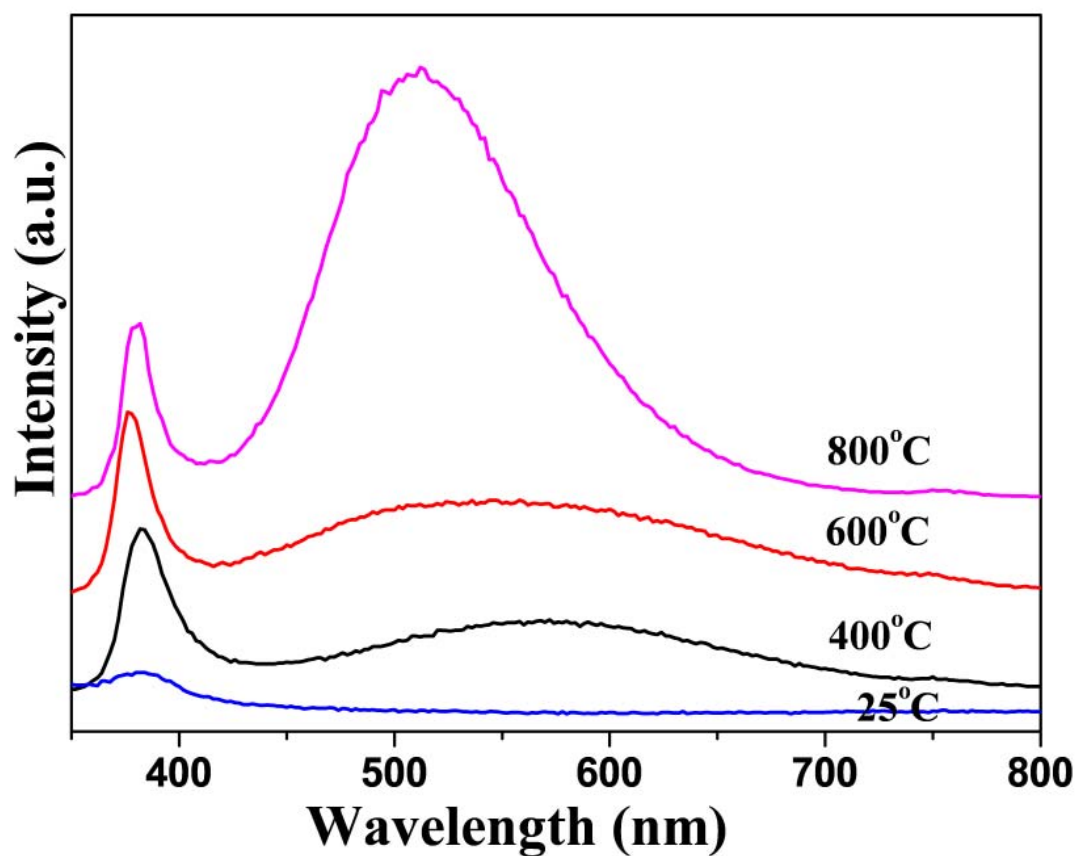


Fig. 7.6 (a) Room-temperature PL spectra of ZnO nanotubes after rapid thermal annealing at various temperatures in O₂ atmosphere.

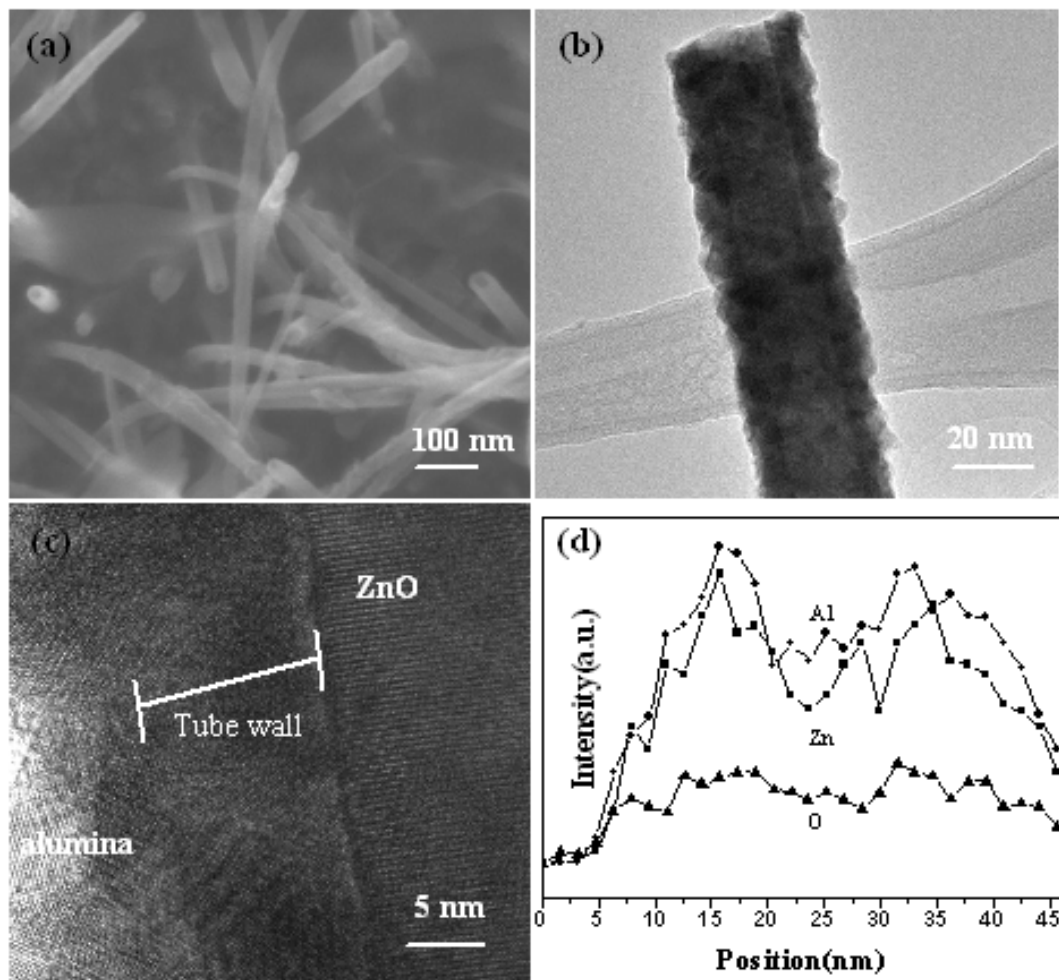


Fig. 7.7 (a) SEM and (b) TEM images of the alumina nanoparticles-coated ZnO nanotubes. (c) High magnification TEM images of the samples. (d) Intensity profile of Al, Zn, and O across and along one tube diameter.

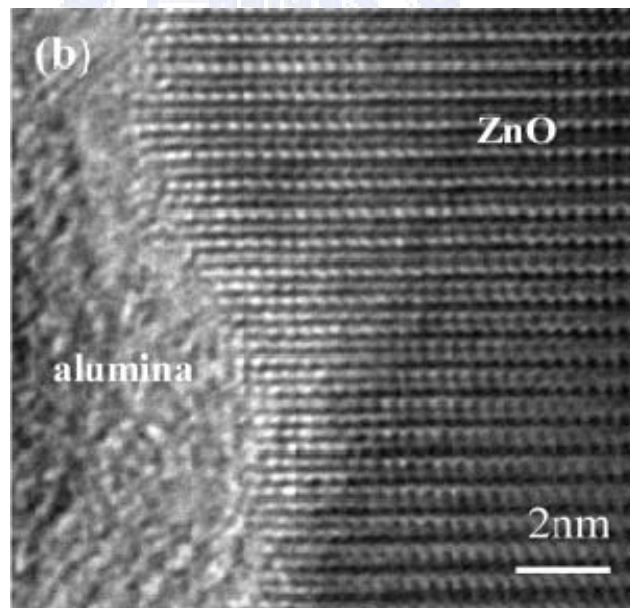
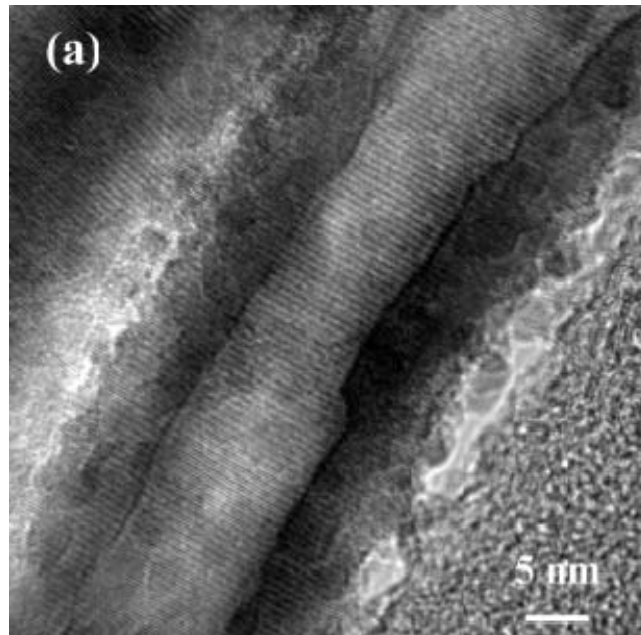


Fig. 7.8 (a) High magnification TEM images of the (a) interface and (b) core of a sample annealed at 400°C in ambient oxygen.

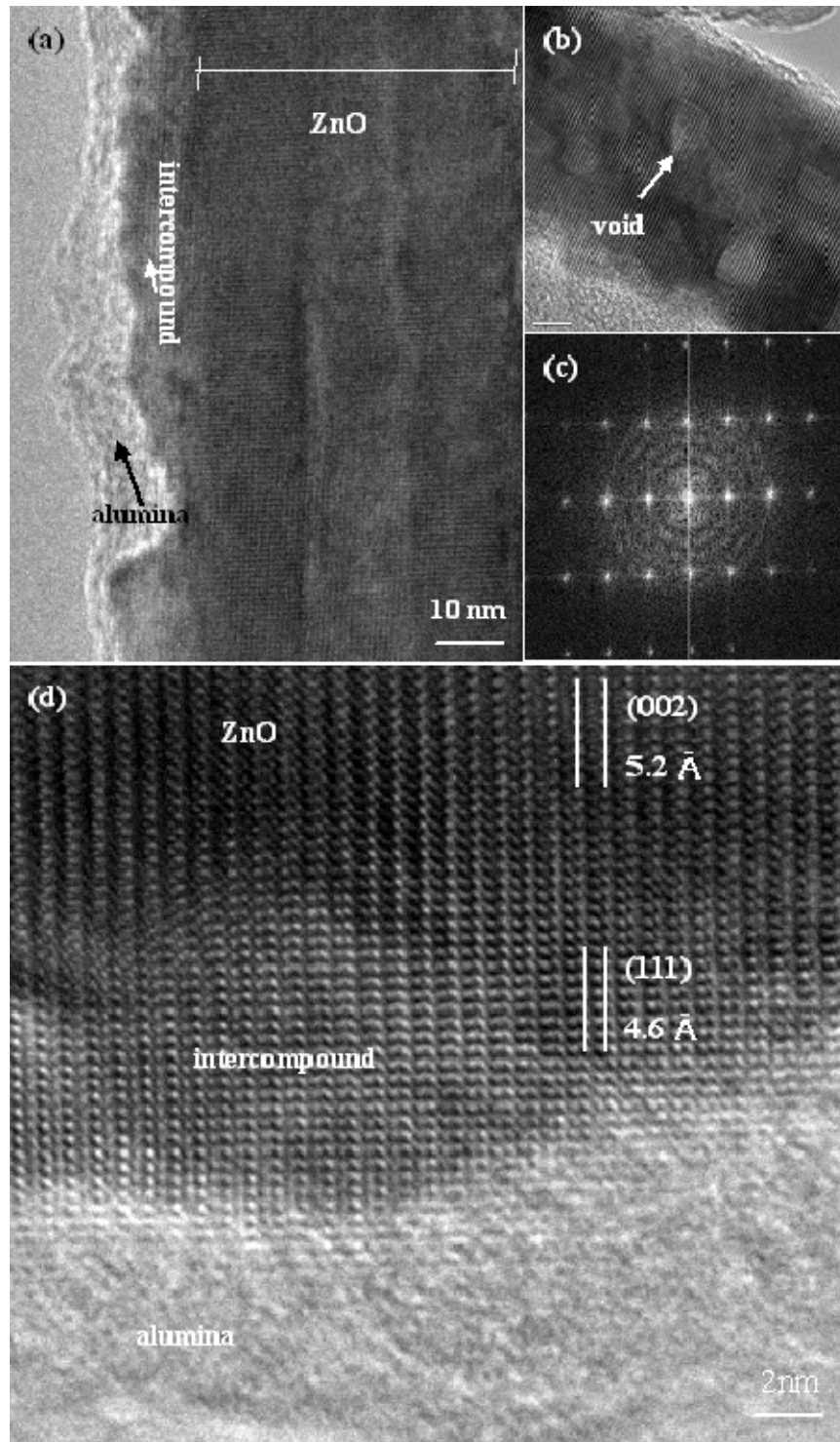


Fig. 7.9 (a) TEM overview of samples. (b) Magnified mid-section images from samples annealed at 600°C in oxygen. (c) Corresponding ED pattern. (d) High-resolution TEM images of interface of alumina and ZnO nanotubes.

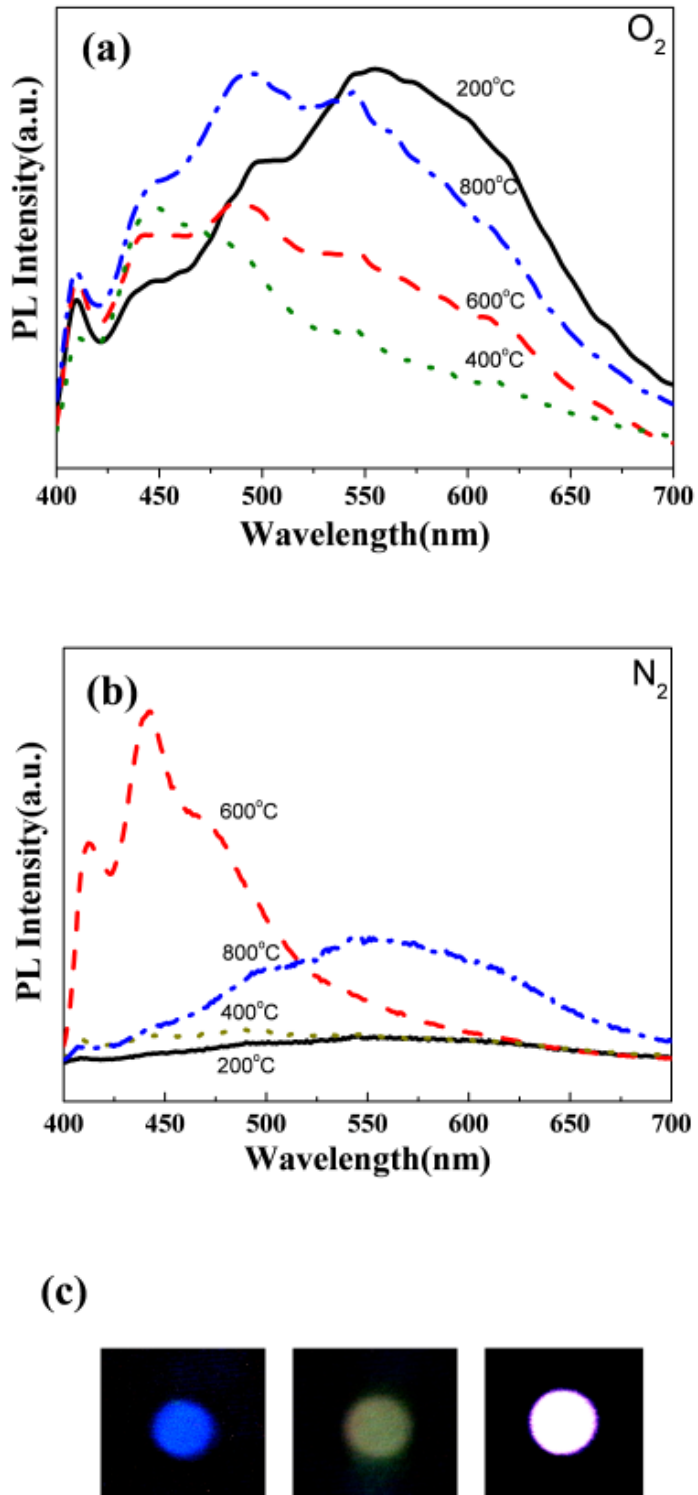


Fig. 7.10 Room-temperature PL spectra of ZnO nanotubes after rapid thermal annealing at various temperatures in (a) O_2 and (b) N_2 . (c) Blue, green and white photograph.

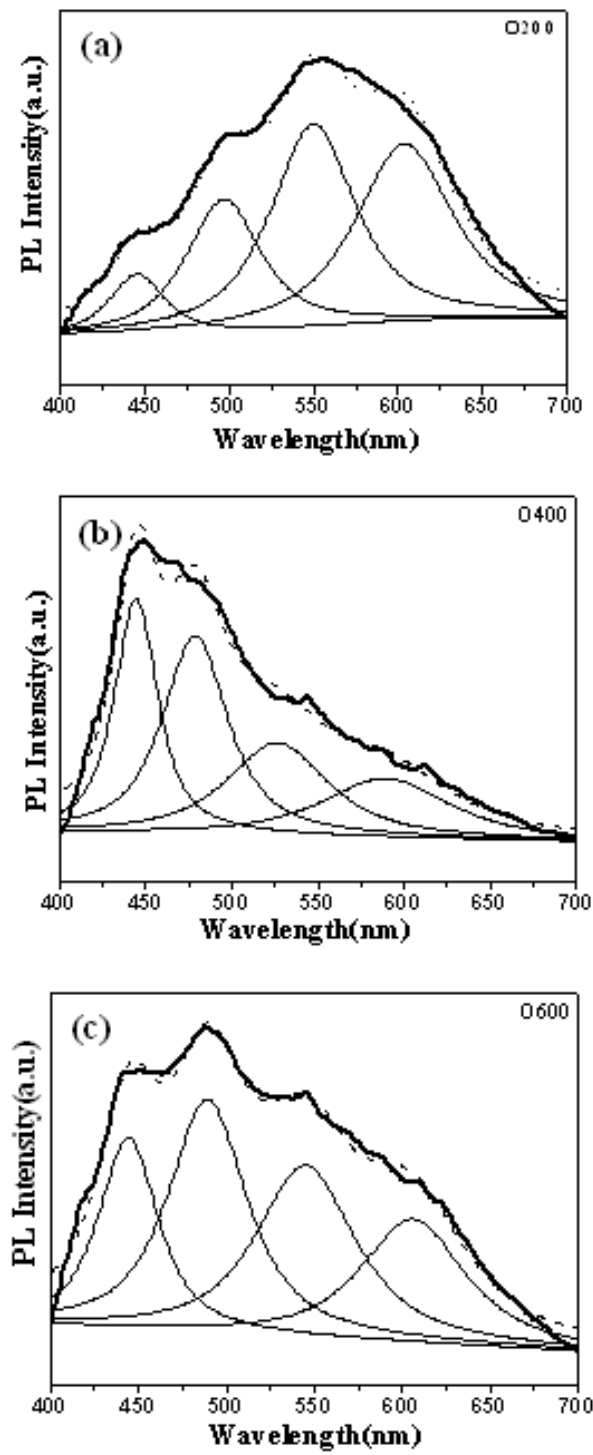


Fig. 7.11 The Gaussian curve fit of PL spectra for samples annealed in oxygen at (a) 200 °C, (b) 400 °C, and (c) 600 °C.

Chapter 8

Smart ZnO nanotube for Controlled Drug Release

8.1 Introduction

Precise drug delivery process has attracted considerable attention. This device requires low power consumption, biocompatible, bio-imaging and low-cost. Among many bio-compatible materials, Zinc oxide (ZnO) nanotubes are of considerable interest for a variety of biomedical applications. ZTs have large surface area-volume ratio and porous structure to be an exceptional nano-template. ZTs own high sensitive properties due to the large surface area-volume ratio in nanostructures. Wang and co-workers used in situ TEM to provide the mechanical resonance behavior of ZnO nanobelts induced by an alternative electric field. [91] Furthermore, they demonstrated a piezoelectric ZnO nanowire as a direct-current nanogenerator which could convert nanoscale mechanical energy into electric energy by ultrasonic waves. [30]

In general, ZnO are believed to be nontoxic, biosafe, and possibly biocompatible. Brayner et al. [47] reported preliminary studies of biocidal effects and cellular internalization of ZnO nanoparticles on Escherichia coli bacteria and showed that ZnO nanoparticles did not induce any damage, indicating ZnO is a nontoxic and biocompatible material. Similar observation was reported by Wang et. al.[49] These studies indicate that ZnO are benefit to be applied in bio-medicals.

Therefore, in this chapter, a study on the drug release of ZnO nanostructure will be investigated to demonstrate how ZnO can be used in biomedical applications. The ZnO nanotubes (ZTs) were used as a template since it can provide more surface area. The ZnO

nanotubes were grown on the ITO/PET substrate with ZnO film as a **catalyst** by chemical solution method. After grown, the surface of the ZTs was modified to become hydrophilic by using oxygen plasma and then put into the solution to absorb drugs. An electric field was applied to study the drug release from drug-loaded ZnO nanotubes. This device possesses low power consumption, biocompatible, bio-imaging and low-cost characteristic.

8.2 Morphology of the dye-ZnO nanotubes

As-grown ZnO nanotubes are synthesized in solution at 95°C for 24 h. A low-magnification SEM image in Fig. 8.1(a) shows that the nanotubes are several (2~5 μm) micrometers in length. The corresponding high-magnification SEM image in Fig. 8.1(b) shows that each nanotube has a uniform width over its entire length. The typical diameter is in the range of 20-30 nm. The ZTs are open-headed tubular structures with wall thicknesses of about 5~7 nm and inner diameters of about 15~20 nm, as shown in the Fig. 8.1(c). Furthermore, the highly preferential growth of ZnO nanotubes was observed along the *c*-axis orientation (0002) with a lattice constant of ~ 0.52 nm. Fig. 8.1(d) shows the dark field (DF) TEM images of the **002 reflection** and proved that the (002) plane of the ZTs disappeared.

Fig. 8.2(a) is the low magnification TEM image of the FITC-ZnO nanotubes with the diameter 30~40 nm. FITC was considered as a model drug to simulate the drug release behavior because it was a fluorescence dye. From the image, it can be clearly observed that the dye is absorbed on the ZTs to form core/shell structure. The high-resolution transmission electron microscopy (HRTEM) image in Figure 8.2(b) confirms FITC-ZnO nanotubes with a core tube structure and a thin amorphous shell. No observable crevices or cracks are visually detectable at the interface of these core/shell nanospheres, suggesting excellent physical integrity between the two dissimilar phases. The thickness of the shell is about 5~10 nm on average and the shell demonstrates a relatively dense nanoarchitecture. Fig. 8.2(c) further

reveals that the dye with the not only the surface but also the head of ZTs have been completely surrounded by dye. Due to capillarity, it could be supposed that the dye was encapsulated into the ZTs.

8.3 Release behavior of the dye-ZnO nanotubes

Figure 8.3 schematically illustrates the hypothesis of the release behavior of the dye-ZnO nanotubes. After the ZTs were synthesized on the substrate, the substrate was coated with Au electrode on the two ends. Then, the device was put into the neutral condition, such as 100 ml D.I water and actuated by applying a positive voltage. When the device was applied with an electric field, it was observed that the dye loaded on the ZTs would be released into the water. The mechanical resonance of a single ZnO nanobelt, induced by an alternative electric field, was proved by in situ transmission electron microscopy. Due to the rectangular cross section of the nanowires, two fundamental resonance modes have been observed corresponding to two orthogonal transverse vibration directions. Therefore, a single dye-loaded nanotube would release the dye when applying the electric field. In addition, tune the release rate could be tuned and controlled by using various frequencies in this study.

Figure 8.4(a) shows the current versus voltage (I-V) characteristics for a pure ZTs device. This result reveals that the ZTs present the characteristic similar to Ohmic contact between electrode and ZTs. The same condition was used to examine the dye-loaded ZTs. Before release process, the I-V curve is very rough. According to Yang's report [44], a better electron transport in these nanowire films is a product of their excellent crystallinity and a radial electric field within each nanowire that assists carrier collection by repelling photoinjected electrons from the surrounding electrolyte. When something were absorbed on the surface of the ZTs, a phenomenon of the band bending would reduce the surface recombination velocity of the majority-carrier electrons regardless of the speed at which the electrons move.

Recombination may remain diffusion limited, but the rate which electrons transport at the oxide surface is determined by the magnitude of the surface field rather than the diffusion constant for electrons in the wire cores. Therefore, the electron could not transport continuously on the surface of the ZTs because the dye was absorbed on the surface of the ZTs, indicating that it would make the I-V characteristic rough. After the dye was completely released, it was observed that the I-V characteristic was restored to approach pure ZTs state, as shown in Fig. 8.4(b).

A kinetic analysis was performed using photoluminescence (PL) spectroscopy to monitor the release of dye molecules from the core-shell nanotubes in different time periods under exposure to high-frequency electric field. Fig. 8.5(a) shows the chemical structure of the FITC. Fig. 8.5(c) and (d) show the resulting PL spectra of the released dye at different time periods under applied electric frequencies at 463 kHz and 100 kHz, respectively, where the peak intensity of the fluorescence spectra increases with time period independent of electric frequencies. The peak is corresponding to the green emission which is emitted by the FITC. It is noted that the peak intensity at 463 Hz is stronger compared to that at 100 kHz. This indicates that the cumulative released amount is much increased over 18 min-stimulus at 463 kHz compared to that at 100 kHz. The ZTs will be vibrated by the high frequency electric field. Moreover, the amplitude of vibration would increase with the frequency increasing. Therefore, when the ZTs were vibrated strongly, the dye would drop from the surface of the ZTs. It would be assigned that vibration could be reduced the interforce between dye and ZTs with time increasing.

Fig. 8.5(b) shows that the release profile of dye for dye-loaded ZnO nanotubes is recorded by applying different external high-frequency electric field at three specific times. After electric excitation, a significant increase in the released amount of drug was observed. The result implied that the drug molecules in the nanotubes exactly followed the signals switching from burst to slow release for each operation. While applying an electric field, the amounts of

drug release can increase instantly, and under suitable control, the drug concentration can reach the therapeutic window within a short time period. A control experiment was also carried out to display that the model drug did not exhibit any obvious release if no electric field was applied. This indicates that a repeat drug release can be controlled through the ZnO nanostructure and the released amounts of the drug can be also tuned through the operation time.

8.4 Cell incubation with zinc oxide nanotubes (ZTs)

HeLa (human cervical cancer) cells were maintained in DMEM (Dulbecco's modified Eagle's medium) containing 10% fetal bovine serum, 100 units/mL penicillin, and 100 µg/mL streptomycin. Cells were cultured with complete medium at 37 °C in a humidified atmosphere of 5% CO₂ in air. For all of the experiments, cells were harvested from subconfluent cultures by use of trypsin and were resuspended in fresh complete medium before plating.

Cellular uptake of the zinc oxide nanotubes (ZTs) was investigated by PL microscopy. After 24 hours of HeLa cell incubation, which is employed as a cancer cell model, cells treated with zinc oxide nanotubes (ZTs) were monitored. The ZTs under the PL microscopy can be observed like dark dots. As the Figure X shown, the cells exhibited the normal morphologies even under the high concentration of the ZTs (>100 roots/cm²). The cells surrounded by the ZTs can still highly attach on the plates, suggesting the ZTs showed low efficiency to affect the cell growth although the ZTs were not highly uptaken by the cells. Furthermore, the normal cells, MRC-5 cell lines, were incubated with the substrate covered the ZTs. After 12 hours, the cells can rapid attach on the substrate, indicating the good biocompatible of ZTs substrate. The cytoskeleton also can be seen clear on the substrate after the dyeing, and maintain well and strong structure. This finding indicates that the ZTs substrate showed little cytotoxicity to the cancerous and normal cells, suggesting excellent biocompatible character and should accordingly be highly compatible to healthy cells. As a critical requirement for drug delivery strategy, reduction of the cytotoxicity of drug carrier

itself can be satisfied and a further minimize the cytotoxicity of the drug can be accompanied.

8.5 Summary

We have developed smart dye-ZnO nanotubes devices. The dye is absorbed on the surface of the ZTs. Furthermore, the dye release behavior can be controlled by the high frequency electric field. Furthermore, by the cell survive experimental, the biocompatible properties of the ZTs would be proved excellently.



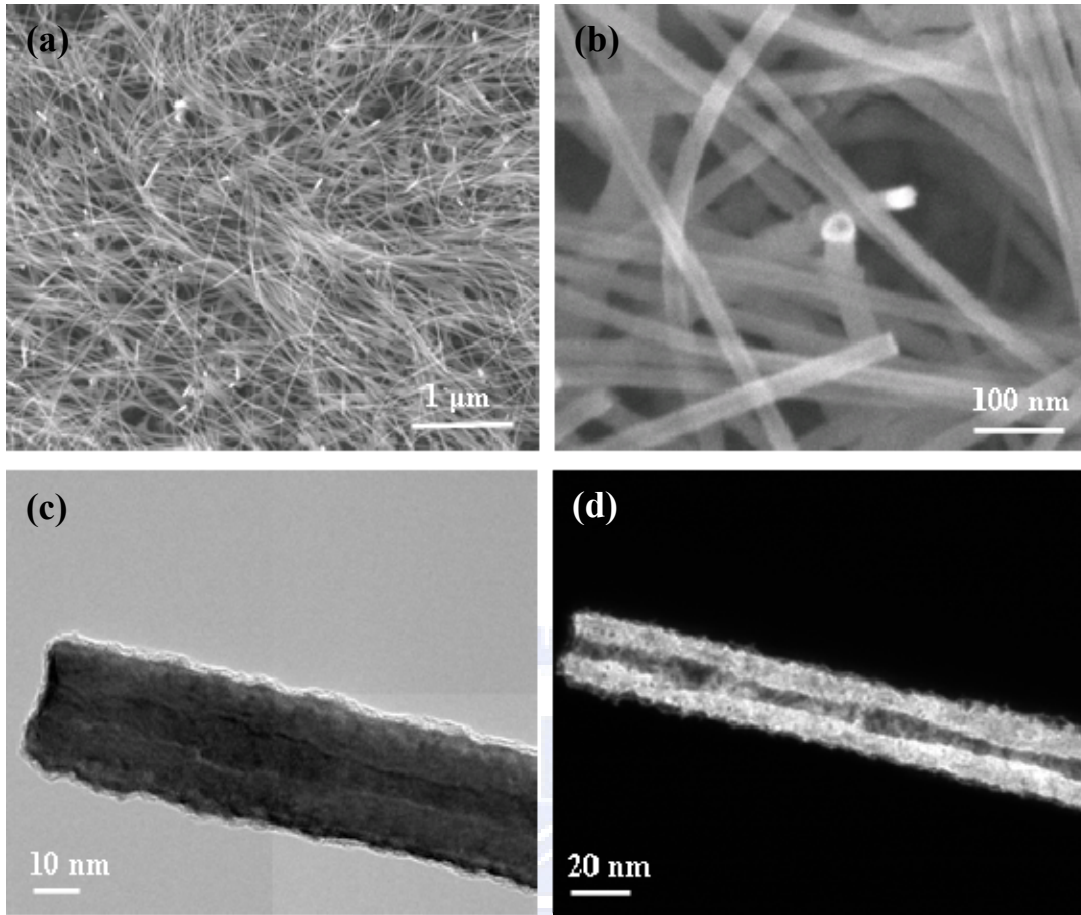


Fig 8.1 (a) SEM images of ZnO nanotubes. (b) High-magnification SEM image of ZnO nanotubes. (c) TEM image of a single ZnO nanotube. (d) Dark-field TEM image of a single ZnO nanotube.

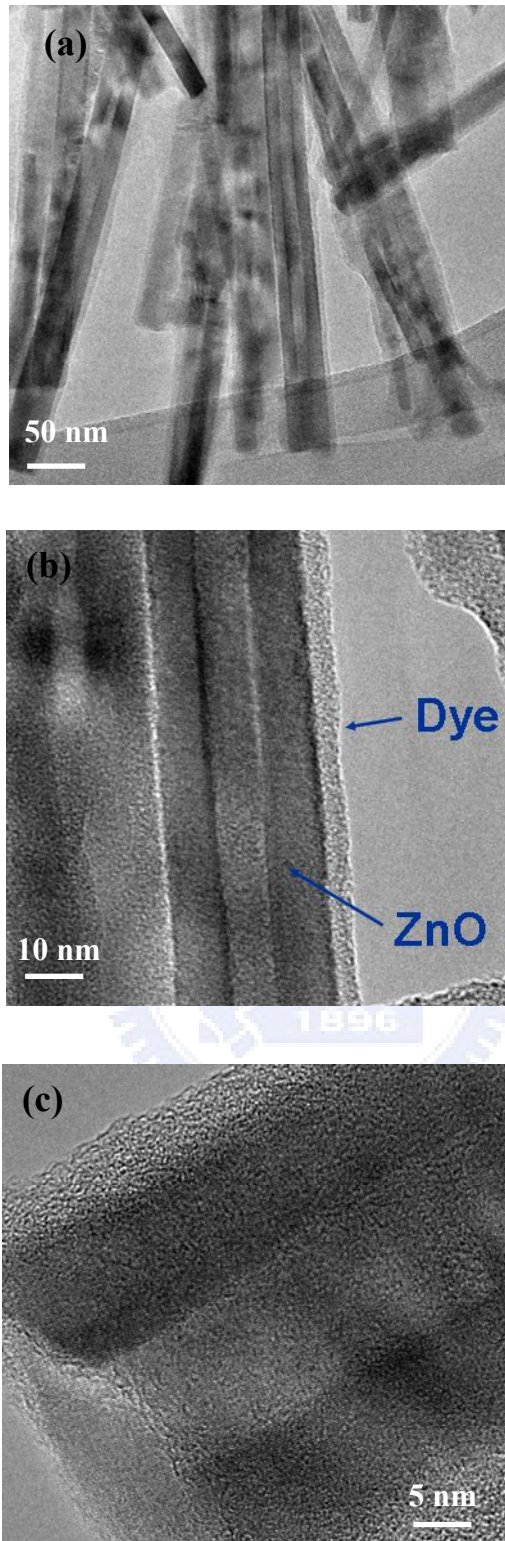


Fig 8.2 (a) TEM image of dye-ZnO nanotubes. (b) High- resolution TEM image of the dye-ZnO nanotubes (b) on the side part, (c) on the end part.

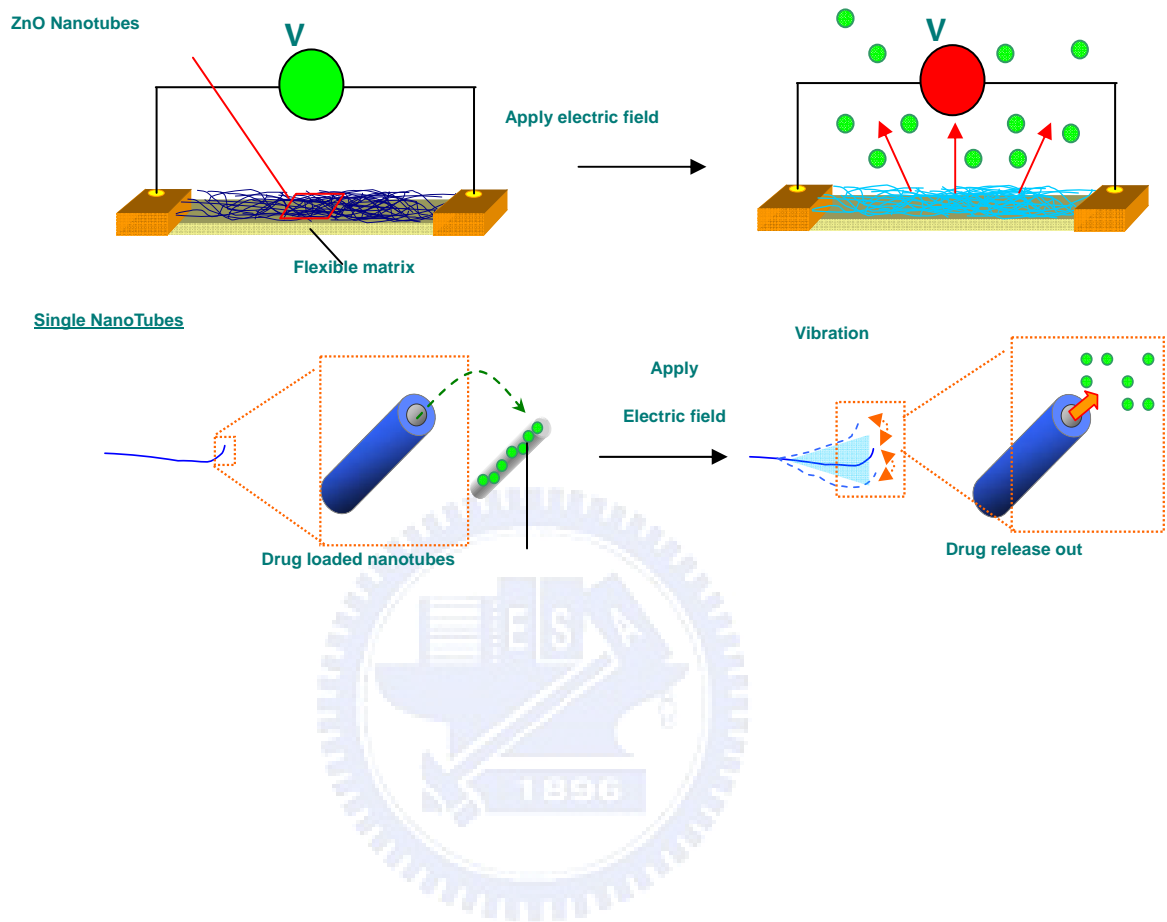


Fig. 8.3 Schematic illustration of the controlled release of dye-ZnO nanotubes.

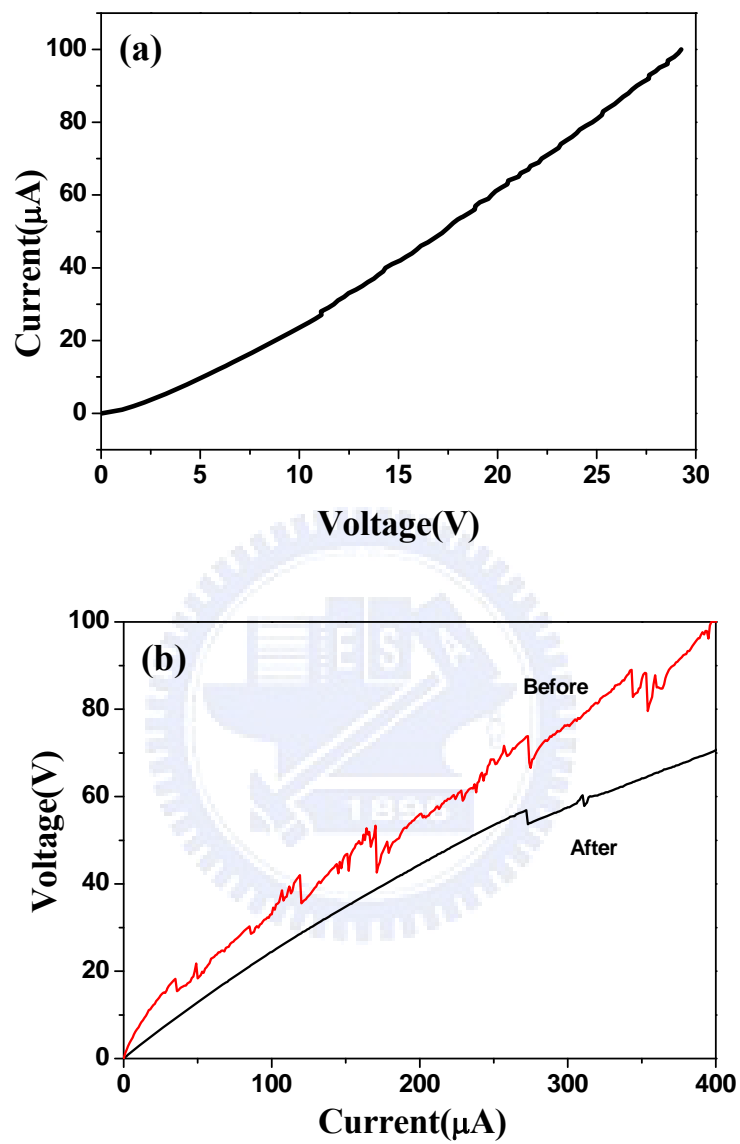


Fig 8.4 I-V characteristics of the (a) ZTs. (b) dye-ZTs with electric field applied.

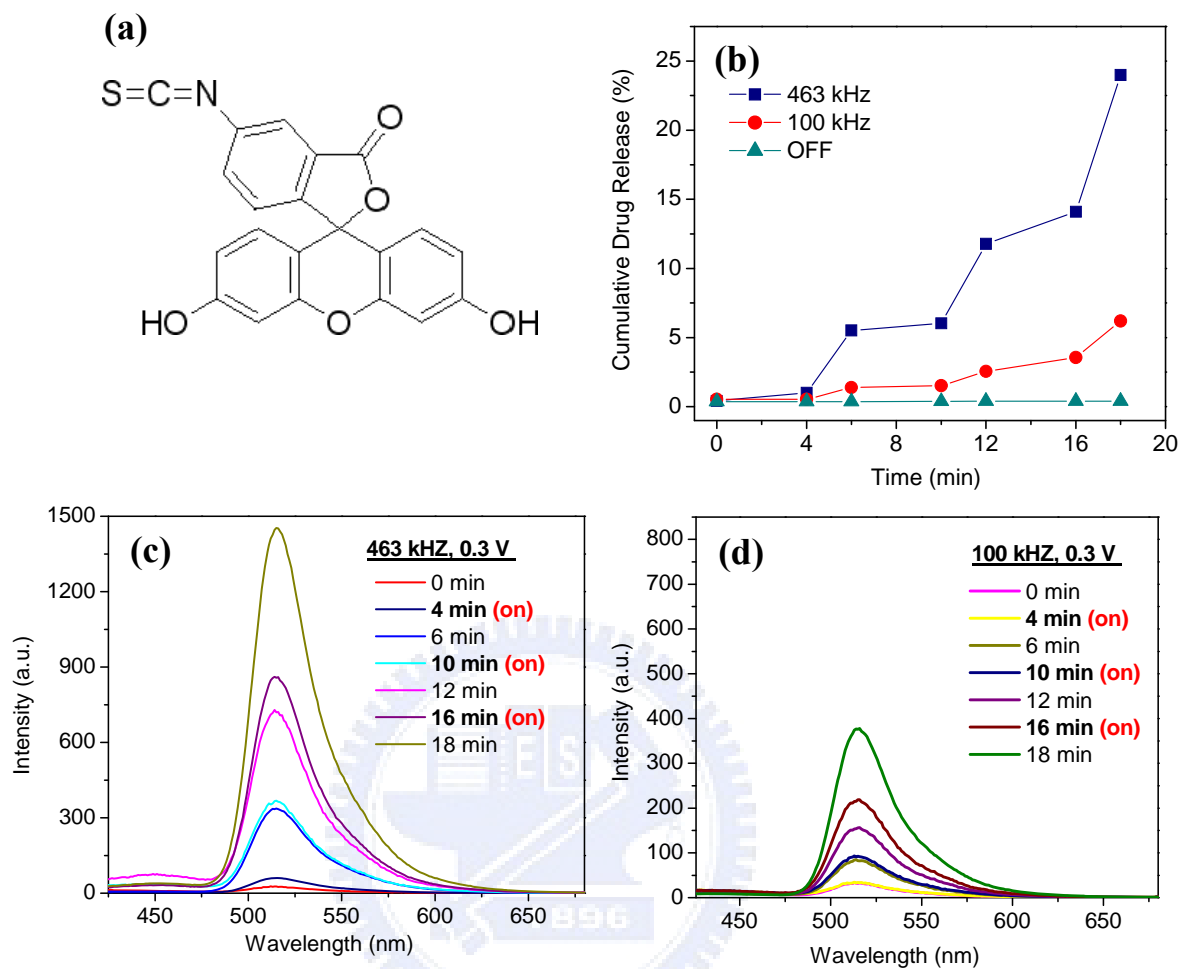


Fig 8.5 (a) FITC structure diagram (b) Cumulative dye release profiles of dye-ZnO nanotubes from different frequency in electric field. Emission spectra of the dye-ZnO nanotubes for applying (c) 463 kHz (d) 100 kHz electric field.

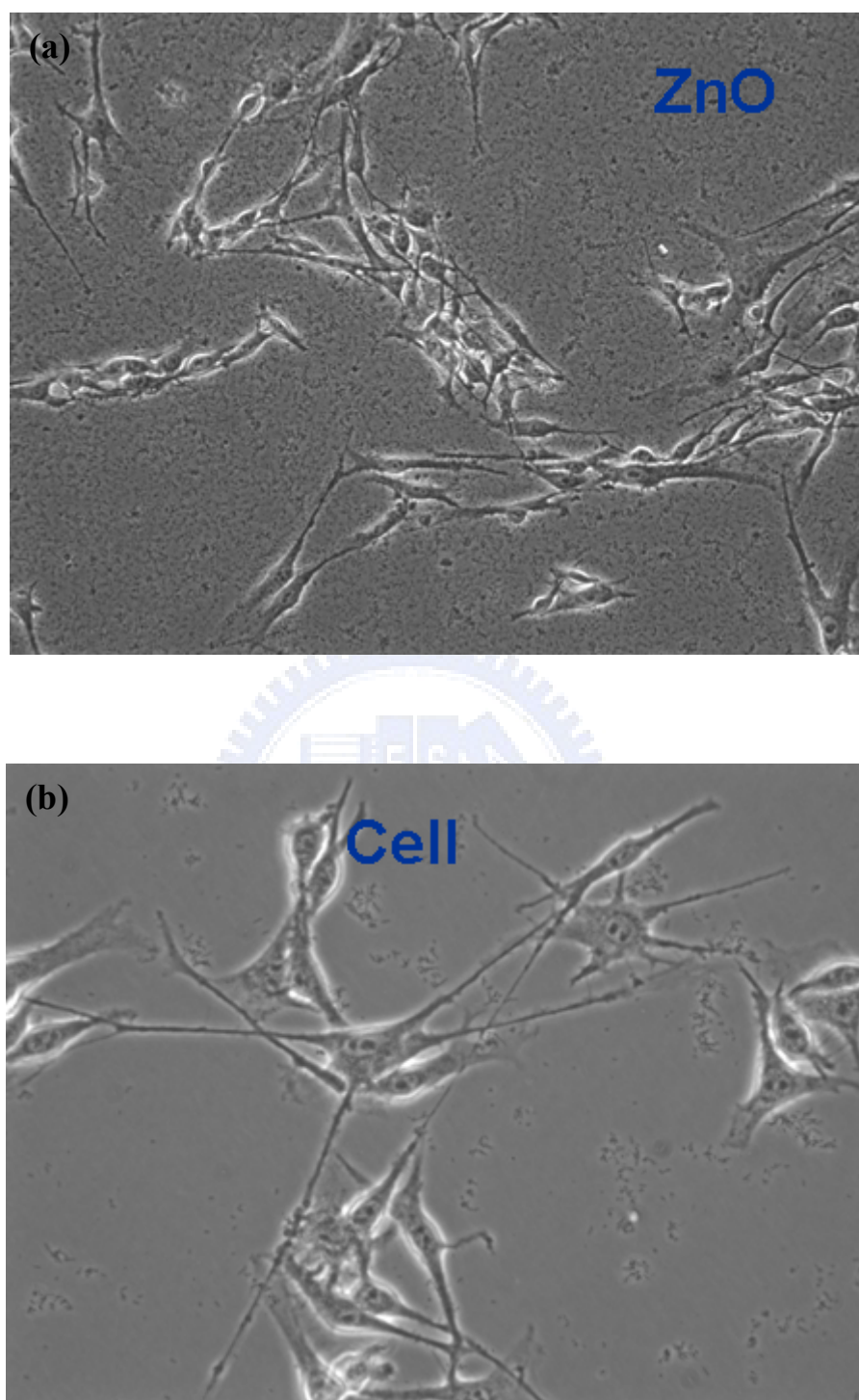


Fig. 8.6 (a) Fluorescence microscopy images of HeLa cells absorbed on the (a) large amounts (b) small amounts of the ZTs after 24h incubation.

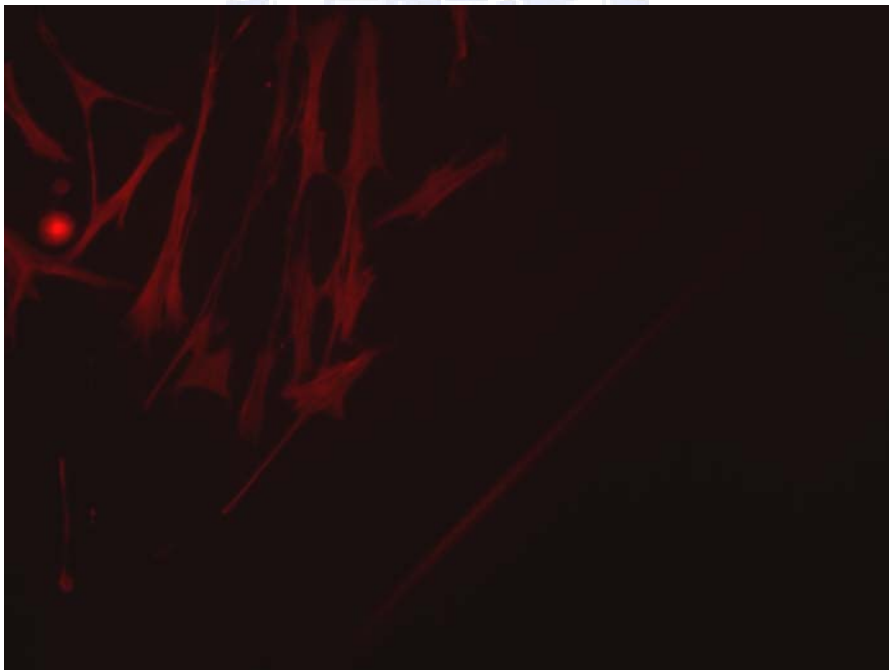
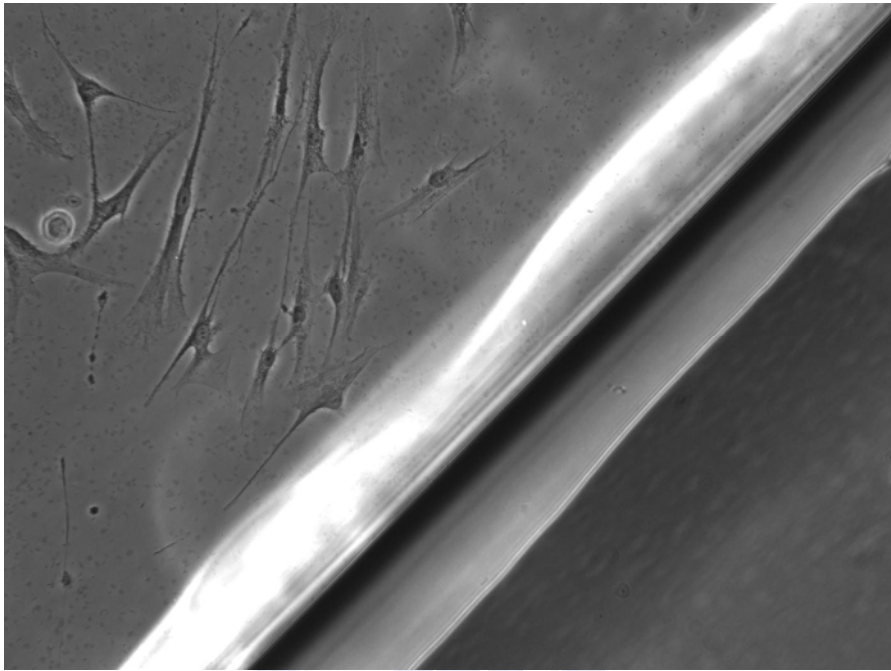


Fig. 8.7 Fluorescence microscopy images of MRC-5 cells absorbed on the ZTs after 36h incubation.

Chapter 9

Conclusions

9.1 Tunable growth and Growth behavior of ZnO nanorods synthesized in the aqueous solution

The growth of patterned ZnO nanorods can be controlled by changing the annealing conditions of the ZnO_f/Si substrates. When the ZnO_f/Si substrate was annealed above a critical temperature to promote the crystallization of ZnO phase, both ZNs and ZnO_f on Si substrate were found to become crystallographically matched. The ZNs seem to preferentially nucleate from the cup tip near the grain boundary between two ZnO grains in the ZnO film. A higher annealing temperature may lead to the formation of a larger ZnO crystal due to coplanar coalescence behavior of several individual ZnO nanorods. The scattered ZNs present a two-stage growth mechanism with a self-assembly process of ZNs in the later growth stage. Aligned ZNs were directly grown along the [0 0 0 2] direction from the ZnO film on Si.

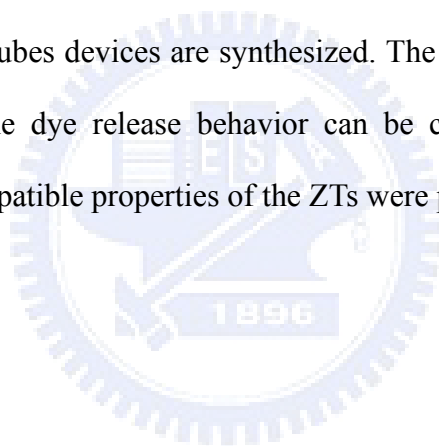
9.2 Synthesis and Optical Properties of the Alumina/ZnO nanostructure

It is demonstrated that well-aligned arrays of Al₂O₃/ZnO nanocables on ZnO_f/Si substrate substrates buffered with a ZnO film by combining a simple chemical solution with a low-temperature treatment. Al₂O₃/ZnO nanocables show a strong blue emission peak at ~450 nm appears at 400°C and 600°C in O₂ and N₂ atmospheres, respectively. With the increase of annealing temperature, the OH band in pseudo-boehmite structure tends to be broken and Al—O• would be formed during the phase transformation from pseudo-boehmite phase (octahedrally coordinated structure) to γ-phase aluminum oxide (tetrahedrally coordinated structure).

structure), favoring pentahedrally coordinated aluminum and the occurrence of singly ionized oxygen vacancies which are regarded to the F^+ center. The alumina nanoparticles-coated ZnO nanotubes emitted different light emissions as the annealing temperatures and atmospheres were changed. According to the Kirkendall effect, Zn atoms diffused into the alumina layer and several voids were formed in the core of the tubes. When ANZTs were annealing at a higher temperature (600°C), the samples demonstrated white-light emission. A white-light emission, consisting of blue, blue-green, green and yellow band emissions, was obtained from alumina nanoparticles-coated ZnO nanotubes.

9.3 Smart ZnO nanotube for Controlled Drug Release

Smart dye-ZnO nanotubes devices are synthesized. The dye is absorbed on the surface of the ZTs. Furthermore, the dye release behavior can be controlled by the high frequency electric field. The biocompatible properties of the ZTs were proved excellently.



References

- [1] M. H. Huang, S. Mao, H. Feick, H. Yan, Y. Wu, H. Kind, E. Weber, R. Russo, P. Yang, **Science** 2001, 292, 1897.
- [2] W. I. Park, G. C. Yi, M. Kim, S. J. Pennycook, **Adv, Mater.** 2003, 15, 526.
- [3] S. Nakamura, *Science* 1998, 281, 956.
- [4] X. Duan, Y. Huang, R. Agarwai, C. M. Lieber, *Nature* 2003, 421, 241.
- [5] Alex B. F. Martinson, Jeffrey W. Elam, Joseph T. Hupp, and Michael J. Pellin, *nano lett.* 2007, 7, 2183.
- [6] M. Roselli, A. Finamore, L. Garaguso, M. S. Britti, E. Mengheri, *Biochem. Molec. Actions Nutriments* **2003**, 4007.
- [7] P. Yang, H. Yan, S. Mao, R. Russo, J. Johnson, R. Saykally, N. Morris, J. Pham, R. He, H. J. Choi, *Adv. Funct. Mater.* **2002**, 12, 323.
- [8] W. I. Park, D. H. Wim, S. W. Jung, G. C. Yi, *Appl. Phys. Lett.* **2002**, 80, 4232.
- [9] C. K. Xu, G. D. Xu, Y. K. Liu, G. H. Wang, *Solid State Commun* **2002**, 122, 175.
- [10] B. D. Yao, Y. F. Chan, N. Wang, *Appl. Phys. Lett.* **2002**, 81, 757.
- [11] L. Vayssieres, *Adv. Mater.* **2003**, 15, 464.
- [12] X. Y. Kong and Z. L. Wang, *Nano lett.* **2003**, 3, 1625.
- [13] X. Y. Kong, et. Al. *Science* **2004**, 303, 1348.
- [14] Q. Li, V. Kumar, Y. Li, H. Zhang, Tobin J. Marks and Robert P. H. Chang, *Chem. Mater.* **2005**, 17, 1001.
- [15] Q. Yu, W. Fu, C. Yu, H. Yang, R. Wei, M. Li, S. Liu, Y. Sui, Z. Liu, M. Yuan, and G. Zou, *J. Phys. Chem. C* **2007**, 111, 17521.
- [16] D. P. Norton, Y. W. Heo, M. P. L'vill, K. Ip, S. J. Pearton, M. F. Chisholm and T. Steiner, *materialstoday* 2004, 34

- [17] J. Y. Lao, J. Y. Huang, D. Z. Wang and Z. F. Ren, *Nano Lett* **2003**, 3 235.
- [18] Z. W. Pan, Z. R. Dai and Z. L. Wang, *Science* **2001**, 291 1947.
- [19] P. O'Brien, T. Saeeda, J. Knowles, *J. Mater. Chem.* **1996**, 6, 1135.
- [20] R. B. Peterson, C. L. Fields, B. A. Gregg, *Langmuir* **2004**, 20, 5114.
- [21] L. Vayssieres, *Adv. Mat.* **2003**, 15, 464.
- [22] M. H. Huang, Y. Wu, H. Feick, N. Tran, E. Weber, P. Yang, *Adv. Mater.* **2001**, 13, 113.
- [23] R. A. Laudise, A. A. Ballman, *J. Phys. Chem.* **1960**, 64, 688.
- [24] R. A. Laudise, E. D. Kolb, A. J. Caporaso, *J. Amer. Ceram. Soc.*, 47 (1) 9.
- [25] J. Han et al., *J. Eur. Ceram. Soc.* **2002**, 22, 24
- [26] J. Anderson and Ghis G. Van de Walle, *Phy. Rev. B* **2007**, 76, 165202.
- [27] J. Wang, G. Du, Y. Zhang, B. Zhao, X. Yang and D. Liu, *J. Cryst. Growth* 2004, 263, 269.
- [28] M. Law, Lori E. Greene, Justin C. Johnson, R. Saykally and P. Yang, *nature materials* **2005**, 4, 455.
- [29] J. H. Choy, E. S. Jang, J. H. Won, J. H. Chung, D. J. Jang and Y. W. Kim, *Adv. Mat.* **2003**, 15, 1911.
- [30] X. Wang, J. Song, J. Liu, Z. L. Wang, *Science* **2007**, 316, 102
- [31] L. Vayssieres, K. Keis, A. Hagfeldt and S. E. Lindquist, *Chem. Mater.* **2001**, 13, 4395.
- [32] Y. Sun, N. George Ndifor-Angwafor, D. Janson, Riley, Michael N. R. Ashfold, *Chem. Phys. Lett.* **2006**, 431, 352.
- [33] G. Zhang, M Adachi, S. Ganjil, A. Nakamura, J. Temmyo and Y. Matsui, *J. J. Appl. Phys.* **2007**, 46, L730.
- [34] Alex B. F. Martinson, Jeffrey W. Elam, Joseph T. Hupp and Michael J. Pellin, *Nano Lett.* **2007**, 7, 2183.
- [35] P. Alphonse, M. Courty, *Thermoch. Acta* **2005**, 425, 75
- [36] J. J. Fitzgerald, G. Piedra, S. F. Dec, M. Seger and G. E. Maciel, *J. Am. Chem. Soc.* **1997**, 119, 7832.

- [37] A. Vijay, G. Mills and H. Metiu, *J. Chem. Phys.* **2002**, 11, 4509.
- [38] B. E. Yoldas, *J. Non-Cryst. Solids* **1992**, 147&148, 614.
- [39] Y. Kurokawa, T. Suga, S. Nakata and T. Ikoma, S. Tero-Kubota, *J. Mat. Sci. Lett.* **1998**, 17, 275.
- [40] Z. Q. Yu, D. Chang and C. Li, *J. Mater. Res.* **2001**, 16, 1890.
- [41] T. Ishizaka, S. Tero-Kubota, Y. Kurokawa and T. Ikoma, *J. Phys. Chem. Solids* **2003**, 64, 801.
- [42] S. K. Panda, A. Dev and S. Chaudhuri, *J. Phys. Chem. C* **2007**, 111, 5039.
- [43] M. Law, L. E. Greene, A. Radenovic, T. Kuykendall, J. Liphardt and P. Yang, *J. Phys. Chem. B* **2006** 110, 22652.
- [44] J. Goldberger, R. He, Y. Zhang, S. Lee, H. Yan, H. J. Choi and P. Yang, *Nature* **2003**, 422, 599.
- [45] J. Hwang, B. Min, J. S. Lee, K. Keem, K. Cho, M. Y. Sung, M. S. Lee and S. Kim, *Adv. Mat.* **2004**, 16, 422.
- [46] J. F. Hong, K. Mato, S. Roland, N. Kornelius, P. Eckhard, H. Dietrich, Z. Margit and G. Ulrich, *Nature mater.* **2006**, 5, 627.
- [47] R. Brayner, F. L. Roselyne, N. Brivois, S. Djediat, M. F. Benedetti and F. Fievet, *Nano Lett.* **2006**, 6, 866.
- [48] M. Roselli, A. Finamore, I. Garaguso, M. S. Britti and E. Mengheri, *Biochem. Molec. Actions Nutriments* **2003**, 4077.
- [49] J. Zhou, N. Xu and Z. L. Wang, *Adv. Mat.* **2006**, 18, 2432.
- [50] Y. L. Wu, C. S. Lim, S. Fu, A. I. Y. Tok, H. M. Lau, F. Y. C. Boey and X. T. Zeng, *nanotechnology* **2007**, 18, 215604.
- [51] F. Zhang, X. Wang, S. Ai, Z. Sun, Q. Wan, Z. Zhu, Y. Xian, L. Jin, K. Yamamoto, *Ana. Chim. ACTA* **2004**, 519, 155.
- [52] D. P. Norton, Y. W. Heo, M. P. Ivill, K. Ip, S. J. Pearton, M. F. Chisholm, and T. Steiner,

- Materials today **2004**, 34.
- [53] M. H. Huang, S. Mao, H. Feick, H. Yan, Y. Wu, H. Kind, E. Weber, R. Russo, and P. Yang, Science **2001**, 292, 1897.
- [54] W. I. Park, G-C. Yi, M. Kim, and S. J. Pennycook, Adv. Mater. **2003**, 15, 526.
- [55] J. H. Choy, E. S. Jang, J. H. Won, J. H. Chung, D. J. Jang, and Y. W. Kim, Adv. Mater. **2003**, 15, 1911.
- [56] S. C. Liou, C. S. Hsiao, and S. Y. Chen, J. Cryst. Growth **2005**, 274, 438.
- [57] B. Liu and H. C. Zeng, J. Am. Chem. Soc. **2003**, 125, 4430.
- [58] Sampanthar, and J. T. Zeng, J. Am. Chem. Soc. **2002**, 124, 6668.
- [59] C.M. Lieber, Y. Cui, Science **2001**, 291, 851.
- [60] M. Zamfirescu, A. Kavokin, B. Gil, G. Malpuech, M. Kaliteevski, Phys. Rev. B. **2002**, 65, 161205.
- [61] X. Duan, Y. Huang, Y. Cui, J. Wang, C.M. Lieber, Nature **2001**, 409, 66.
- [62] W.I. Park, G. Yi, M. Kim, S.J. Pennycook, Adv. Mater. **2003**, 15, 526.
- [63] Y. Wu, P. Yang, J. Am. Chem. Soc. **2001**, 123, 3156.
- [64] W.T. Chiou, W.Y. Wu, J.M. Ting, Diamond Relat. Mater. **2003**, 12, 1841
- [65] W. II. Park, G. Yi, M. Kim, S.J. Pennycook, Adv. Mater. **2002**, 14, 1841.
- [66] L. Vayssieres, K. Keis, J. Phys. Chem. B **2001**, 105, 3350.
- [67] S. Yamabi, H.J. Imai, Mater. Chem. **2002**, 12, 3773.
- [68] J.H. Choy, E.S. Jang, Adv. Mater. **2003**, 15, 1911.
- [69] J.C. Bailar, H.J. Emeleus, R. Nyholm, A.F. Trotman-Dickenson, Comprehensive Inorganic Chemistry, vol. 3, Pergamon Press, Oxford, **1975**.
- [70] L. Manna, E.C. Scher, A.P. Alivisatos, J. Am. Chem. Soc. **2000**, 122, 12700.
- [71] T.J. Trentler, K.M. Hickman, S.C. Goel, A.M. Viano, P.C. Gibbson, W.E. Buhro, Science **1995**, 270, 1791.
- [72] A.R. West, Basic Solid State Chemistry, Wiley, New York, **1999**, 244.

- [73] C.C. Lin, H.P. Chen, S.Y. Chen, Chem. Lett. **2004**, submitted.
- [74] B. Liu, H.C. Zeng, J. Am. Chem. Soc. **2003**, 125, 4430.
- [75] E. P. Gusev, M. Copel, E. Cartier, I. J. R. Baumvol, C. Krug, M. A. Gribelyuk, Appl. Phys. Lett. **2000**, 76, 17.
- [76] Tombacz, E., Dobos, A., Szeker, M., Narres, H.D., Colloid Polym. Sci. **2000**, 278, 337.
- [77] G. Paglia, S. Božin, and J. L. Billinge, Chem. Mater. **2006**, 18, 3242.
- [78] B. C. Lippens, and J. H. de Boer, Acta cryst. **1964**, 17, 1312.
- [79] T. Ishizaka and Y. Kurokawa, J. App. Phys. 2001, 90, 2257.
- [80] Y. Du, W. L. Cai, C. M. Mo, J. Chen, L. D. Zhang, and X. G. Zhu, Appl. Phys. Lett. **1999**, 74, 2951.
- [81] N. E. Hsu, W. K. Hung and Y. F. Chen, J. Appl. Phys. **2004**, 96, 4671.
- [82] X. L. Wu, G. G. Siu, C. L. Fu and H. C. Ong, Appl. Phys. Lett **2001**, 78, 2285.
- [83]. M. Nguéfac, A. F. Popa, S. Rossignol and C. Kappenstein, Phys. Chem. Chem. Phys. **2003**, 5, 4279.
- [84] C. W. Chen, K. H. C. Chen, H. Shen, A. Ganguly, L. C. Chen, J. J. Wu, H. I. Wen, W. F. Pong, Appl. Phys. Lett. **2006**, 88, 241905.
- [85] Y. Tong, Y. Liu, C. Shao, Y. Liu, C. Xu, J. Zhang, Y. Lu, D. Shen, X. J. Fan, J. Phys. Chem. B **2006**, 110, 14714.
- [86] X. L. Wu, G. G. Siu, C. L. Fu, H. C. Ong, Appl. Phys. Lett. **2001**, 78, 2285.
- [87] J. Wang, G. Du, Y. Zhang, B. Zhao, X. Yang, D. Liu, J. Cry. Growth **2004**, 263, 269.
- [88] L. H. Quang, S. J. Chua, K. P. Loh, E. Fitzgerald, J. Cry. Growth **2006**, 287, 157.
- [89] S. S. Lin, J. L. Huang, J. Mater. Res. **2003**, 18, 965.
- [90] Y. Yang, D. S. Kim, M. Knez, R. Scholz, A. Berger, E. Pippel, D. Hesse, U. Gosele, M. Zacharias, J. Phys. Chem. C **2008**, 112, 4068.
- [91] X. D. Bai, P. X. Gao, Z. L. Wang and E. G. Wang, Appl. Phys. Lett. **2003**, 82, 4806.

Curriculum Vitae

Name : Chi-Sheng Hsiao (蕭繼聖)

12.10.1978 Born in Taipei (Taiwan)

1997-2001 Undergraduate study in the department of Materials Science and Engineering at
National Cheng Kung University

2001-2003 Graduate study in the department of Materials Science and Engineering at
National Chiao Tung University

2003-2008 PhD study in the department of Materials Science and Engineering at National
Chiao Tung University (Taiwan)

PhD Thesis: Effect of synthesis and structure of nano Zinc Oxide on
Optoelectronic and characteristics and bio-medical application

Publication list

Journal

1. C. C. Lin, C. S. Hsiao, S. Y. Chen and S. Y. Cheng, “Ultraviolet Emission in ZnO Films Controlled by Point Defects”, J. Electrochem. Soc. **2004**, 151, G285.
2. S. C. Liou, C. S. Hsiao and S. Y. Chen, “Growth behavior and microstructure evolution of ZnO nanorods grown on Si in aqueous solution”, J. Crys. Growth **2005**, 274, 438.
3. C. S. Hsiao, C. H. Peng, S. Y. Chen and S. C. Liou, “Tunable growth of ZnO nanorods synthesized in aqueous solutions at low temperatures”, J. Vac. Sci. Technol. B **2006**, 24, 288.
4. C. H. Chiu, C. E. Lee, C. L. Chao, B. S. Cheng, H. W. Huang, H. C. Kuo, T. C. Lu, S. C. Wang, W. L. Kuo, C. S. Hsiao and S. Y. Chen, “Enhancement of light output intensity by integrating ZnO nanorod arrays on GaN-based LLO vertical LEDs“, Electrochemical and Solid State Lett. **2008**, 11, H84.
5. C. S. Hsiao, S. Y. Chen and S. Y. Cheng, “Synthesis and physical characteristics of AlO_x-Coated ZnO nanorod arrays grown in aqueous solution at low temperatures”, J. Phys. Chem. Solids **2008**, 69, 625.
6. C. S. Hsiao, W. L. Kuo, S. Y. Chen, J. L. Shen, C. C. Lin and S. Y. Cheng, “Synthesis and Luminescent Properties of Strong Blue Light-Emitting Al₂O₃/ZnO nanocables”, J. Electrochem. Soc. **2008**, 155, K96.
7. C. S. Hsiao, S. Y. Chen, W. L. Kuo, C. C. Lin and S. Y. Cheng, “Synthesis and optical properties of white-light-emitting alumina/ZnO nanotubes” nanotechnology **2008**, 19, 405608.
8. S. H. Hu, S. Y. Chen, D. M. Liu and C. S. Hsiao, “Core/single-crystal-shell nanospheres for controlled drug release via a magnetically triggered rupturing mechanism”, Adv. Mat. **2008**, 20, 2690.